Accounting for quantum effects in stopping site DFT calculations for muon spectroscopy

ALBERTO HERNANDEZ-MELIAN

Accounting for quantum effects in stopping site DFT calculations for muon spectroscopy

Alberto Hernández-Melián

A thesis presented for the degree of

Doctor of Philosophy

Department of Physics

Durham University

United Kingdom

May 2024

Accounting for quantum effects in stopping site DFT calculations for muon spectroscopy

Alberto Hernández-Melián

Abstract

The technique of μ^+SR is one of the most accurate methods of probing the local magnetism of materials, but to fully utilise its potential, knowledge of the location of the muon sites is required. A popular method is to use density functional theory (DFT) to determine the classical sites from first principles. In this thesis, we present the results of multiple μ^+SR experiments on crystalline materials, where in each case analysis was aided by knowledge of the sites, with a focus on accounting for the quantum behaviour of the muon.

The ground state of the molecular honeycomb lattice $Cu(pym)_{1.5}(H_2O)(BF_4)_2$ is determined using ZF μ^+SR with a transition at $T_N = 4.02 \pm 0.01$ K from a low-temperature phase with an incommensurate magnetic structure, an unusual feature for a coordination polymer. Above the transition interactions with fluorine atoms dominate the signal, consistent with the class of candidate muon sites found through DFT calculations.

We also present results on a pair of very different systems where a combination of ZF μ^+SR experiments and DFT calculations suggest that different muon sites are realised on the two sides of a structural transition. In the first case we look at magnetic switching in the molecular crystal 4-(2-benzimidazolyl)-1,2,3,5-dithiadiazolyl with temperature, finding hysteretic behaviour centred at 274 ± 11 K and caused by a structural phase transition. We also report the results of applying an external current to the Mott insulator material Sr_2IrO_4, finding that our experimental measurements can be explained by a change in the class of muon sites realised as calculated by DFT and an additional FM component to the magnetic structure with $m_z \leq 0.0214\,\mu_B$.

The results of an analysis of a pair of analogous chiral spin chain compounds $[Ni(pym)(H_2O)_4]SO_4$ ($S = 1$) and $[Cu(pym)(H_2O)_4]SiF_6 \cdot H_2O$ ($S = 1/2$) are also presented. Using ZF μ^+SR measurements on the nickel chain we confirm a phase transition at $T_N = 1.82 \pm 0.02$ K to an ordered magnetic ground state and use the magnetic dipole field at

each DFT site to determine the most likely pair of realised sites and confirm that our calculations are consistent with a proposed canted AFM magnetic structure, which we determine to have 1.27 μ_B and make an angle of 34° with the *c*-axis. Similarly, TF μ^+SR measurements are used to confirm that the application of an external field stabilises an ordered magnetic ground state with a phase transition at $B = 3$ T. By calculating the muon sites and using the information to directly simulate the measured polarisation spectra we also find that our results can be explained with an increasing field-dependent copper magnetic moment up to 0.4 μ_B.

Finally, the results of a series of quantum tunnelling calculations in a set of methylated benzene crystals at low temperatures are presented. A potential energy barrier is constructed for transitions between all possible pairs of sites using DFT calculations and the transition rate is estimated using the WKB approximation. We then simulate the avoided level crossing (ALC) μ^+SR spectra expected in each case for different degrees of tunnelling between sites, finding that more tunnelling narrows the resonances and decreases their number. We find the greatest agreement with experimental data for an intermediate amount of tunnelling over the case without tunnelling and with all possible transitions, which is an encouraging result for this novel method of simulating muon quantum behaviour.

Declaration

The work in this thesis is based on research carried out in the Department of Physics, Durham University, UK. No part of this thesis has been submitted elsewhere for any other degree or qualification and it is all my own work unless referenced to the contrary in the text.

Publications

- **A. Hernández-Melián**, B.M. Huddart, F.L. Pratt, S.J. Blundell, M. Mills, H.K.S. Young, K.E. Preuss, T. Lancaster, "Muon-spin relaxation investigation of magnetic bistability in a crystalline organic radical compound", Journal of Physics and Chemistry of Solids, Volume 181, 111493 (2023).

- B.M. Huddart, **A. Hernández-Melián**, T.J. Hicken, M. Gomilšek, Z. Hawkhead, S.J. Clark, F.L. Pratt, T. Lancaster, "MuFinder: A program to determine and analyse muon stopping sites", Computer Physics Communications, Volume 280, 108488 (2022).

- B. M. Huddart, **A. Hernández-Melián**, G. D. A. Wood, D. A. Mayoh, M. Gomilšek, Z. Guguchia, C. Wang, S. J. Blundell, G. Balakrishnan, T. Lancaster, "Field-orientation-dependent magnetic phases in GdRu2Si2 probed with muon-spin spectroscopy", arXiv:2403.09431 (2024).

- **A. Hernández-Melián**, T. Lancaster, S.J. Blundell, F.L. Pratt, B.M. Huddart, P.A. Goddard, R.D. Johnson, R. Scatena, "Determining low-temperature magnetic order in chiral spin chains" (in preparation).

- **A. Hernández-Melián**, F.L. Pratt, L. Liborio, S.J. Clark, T. Lancaster, "Quantum tunnelling between muon sites in methylated benzene crystals" (in preparation).

- C. Wang, **A. Hernández-Melián**, H. Zhao, C. Bernhard, T. Lancaster, H. Luetkens, G. Cao, "Current-mediated control of magnetism in Sr_2IrO_4" (in preparation).

Acknowledgements

Firstly, I would like to thank all three members of my supervisory team: Tom Lancaster, Stewart Clark and Francis Pratt. It has been a privilege to learn so much from each of them and the last four years wouldn't have been the same without their help and encouragement. I couldn't have asked for a better primary supervisor than Tom Lancaster, who has provided constant guidance and feedback in all aspects of the research. Many of the computational parts of the thesis, especially the DFT simulations, owe much to Stewart Clark, who spent a lot of time debugging my failing calculations and teaching me about the internals of CASTEP. I have also enjoyed working with Francis Pratt, who helped enormously with many of the simulations on molecular systems and made me feel very welcome during my time at the ISIS facility.

I have been fortunate to work alongside the excellent members (both past and present) of the Durham muon group: Benjamin Huddart, Thomas Hicken, Matjaž Gomilšek, Nathan Bentley and Theodore Breeze. They kept me sane during beamtimes and much of the progress that I have made during my PhD can be traced back to the discussions and collaboration that they encouraged. Also in Durham, I'd like to thank Nikitas Gidopoulos for sharing his interesting ideas about quantum muon simulations. Special thanks also to Stephen Blundell, who taught and inspired me as both an undergraduate tutor and master's supervisor, setting me on this path.

My thanks also to the instrument scientists at both the ISIS Neutron and Muon Source and the Paul Scherrer Institute. Nearly all of the experimental work presented in this thesis was performed at these facilities and would have not been possible without their constant effort and expert assistance. The ISIS muon group and wider RAL community also made me feel very welcome during the year that I spent based at the facility. The friends that I met there made that period feel incredibly short but productive (thanks in particular to Yue Yuan for making me feel less alone as the other muon scientist in my office).

I have enjoyed the friendly environment at Durham and thank Zachary Hawkhead, Alistair Brewin, Michael Hertaeg, Sam Walker, Harish Charan and all the members of the muon group mentioned previously. It has been a pleasure to share an office with you and

the days would have felt a lot longer without our many conversations. I'm thankful to my friends for providing a necessary distraction from physics but being willing to listen and nod along when required. I also owe a lot to my family who have kept my spirits up and always been willing to encourage me; my parents also nurtured my interest in physics from an early age and have always been willing to provide invaluable mathematical (and financial) support.

Finally, I am grateful to STFC and Durham University Faculty of Science for funding my studentship, and to Durham Hamilton HPC, ARCHER2, MMM Hub and SCARF for the computing resources which made this work possible.

Contents

Acronyms

AFM Antiferromagnetic

ALC μ^+SR Avoided level crossing μ^+SR

CHC $Cu(pym)_{1.5}(H_2O)(BF_4)_2$

CPM $[Cu(pym)(H_2O)_4]SiF_6 \cdot H_2O$

DFPT Density-functional perturbation theory

DFT Density functional theory

DM Density mixing

EDFT Ensemble density functional theory

ESR Electron spin resonance

FFT Fast Fourier transform

FGT Fast Gauss transform

FM Ferromagnetic

GGA Generalised gradient approximation XC functional

GUI Graphical user interface

HF Hartree-Fock

LDA Local-density approximation XC functional

LF μ^+SR Longitudinal field μ^+SR

LST Linear synchronous transit

MB Methylated benzene

NCP Norm-conserving pseudo-potential

NEB Nudged elastic bands

NMR Nuclear magnetic resonance

NPM $[Ni(pym)(H_2O)_4]SO_4$

PIMD Path integral molecular dynamics

QSL Quantum spin liquid

QST Quadratic synchronous transit

SCF Self-consistent field

SIO Sr_2IrO_4

SOE Sums-of-exponentials

SOI Spin-orbit interaction

TF μ^+SR Transverse field μ^+SR

TSS Transition state search

USP Ultrasoft pseudo-potential

WKB Wentzel–Kramers–Brillouin approximation

XC Exchange-correlation function

ZF μ^+SR Zero field μ^+SR

ZPE Zero-point energy

μ^+SR Muon spin resonance / relaxation / rotation

Chapter 1

Muon-spin spectroscopy and density functional theory

Muon-spin spectroscopy (μ^+SR) can provide a very sensitive probe of the local magnetic fields in a material. A series of spin-polarised positive muons are implanted into a sample and the precession and relaxation of the muon spin polarisation are studied to extract information about both the sample's static and dynamic magnetic behaviour (see **Section 1.1** and references). The μ^+SR technique is similar to others that follow the spin depolarisation of a species like nuclear magnetic resonance (NMR) or electron spin resonance (ESR), but has the advantage that experiments can be conducted without an external magnetic field. We also find that the muon's large gyromagnetic ratio makes it very sensitive to weak magnetic moments (such as in molecular magnets as discussed in this thesis) when compared to techniques like neutron scattering and NMR. Some examples of systems where muons have been used successfully to study magnetic properties are molecular magnets [1, 2], non-metallic metals [3], skyrmion lattices [4] and superconductors [5].

The fact that the muon probes locally has certain advantages when compared to bulk techniques used to investigate magnetism, such as susceptibility measurements, which average over the sample volume. Using μ^+SR does, however, create the additional complication that to fully analyse the results of an experiment knowledge of the interstitial sites where muons are implanted into the structure is required, especially when determining magnetic structures and moment magnitudes. Additionally, as a positively-charged defect in the unit cell, the muon will distort the charge density and atomic positions around it, and so ultimately the magnetism observed, raising the question of if the measured fields are intrinsic to the material or a result of implanting the muon. This must be resolved by understanding the interaction between the muon and its environment.

One of the most effective methods of calculating the muon stopping sites in a material is to use the framework of density functional theory (DFT) to perform a geometric

relaxation of the combined supercell and muon system [6,7]. The resulting calculation will make use of a quantum *ab inito* electronic structure calculation to obtain the forces between atoms and then move the positions until these forces vanish. All the calculations presented in this thesis were performed using the CASTEP DFT code [8]. An issue with this method of calculating muon sites is, however, that the muon is treated as a light proton with mass $m_\mu \simeq m_p/9$ and so effects like zero-point motion and quantum tunnelling, which already complicate calculations with proton defects [9] are even more pronounced. Existing approaches to account for such quantum effects in DFT like path integral molecular dynamics (PIMD) [10] have the disadvantage of being prohibitively expensive computationally, especially for large systems with many possible sites. This thesis aims to investigate ways of quantifying the degree to which the muon behaves like a quantum particle and develop methods to model this behaviour in the context of muon site calculations.

The rest of this chapter is separated into two sections. The first provides a brief introduction to μ^+SR (**Section 1.1**) and the most common asymmetry functions used when analysing experimental data. Similarly, the second outlines the basics of DFT (**Section 1.2**) as applied to the problem of calculating classical muon sites.

1.1 Muon-spin spectroscopy

1.1.1 Theory

A very useful probe of the magnetic environment inside a material is muon spin spectroscopy (μ^+SR) where, depending on the dominant effect, the last letter of the acronym can stand for resonance, rotation or relaxation. Measurements are made using muons, which are elementary particles belonging to the class of charged leptons with very similar properties to electrons but a much higher mass ($\simeq 207 m_e$) and a finite average lifetime of 2.2 μs [11]. The technique is less well known than alternatives like nuclear magnetic resonance (NMR) or neutron scattering, in part because intense beams of muons are difficult to create. They present some advantages, however, like being more sensitive to magnetic fields (due to their larger magnetic moment than any nucleus) and allowing for

the measurement of surface or interface effects by tuning the energy of the muon beam [12].

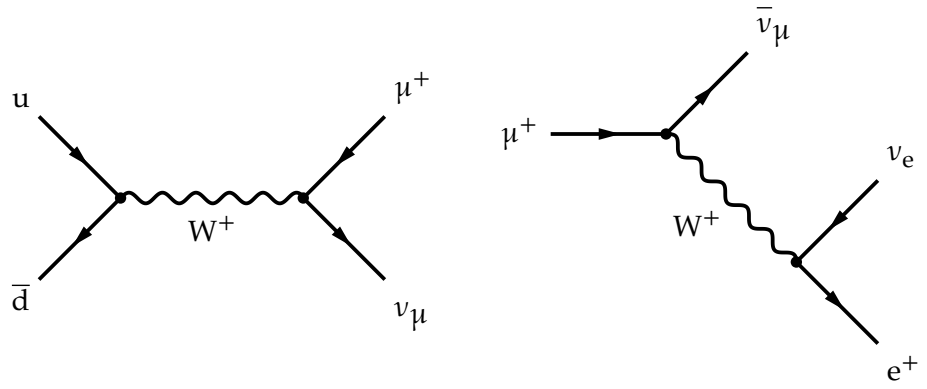

(a) Pion decay (b) Muon decay

Figure 1.1 Feynman diagrams for positive muon creation and decay.

A μ^+SR experiment starts with a source of polarised muons, usually a particle accelerator. For example, a proton beam fired at a graphite target will produce pions ($p + p \rightarrow \pi^+ + p + n$), which will then decay into muons ($\pi^+ \rightarrow \mu^+ + \nu_\mu$), as shown in **Figure 1.1a**. Since the pion has zero spin, the spins of the two products must have opposite values, and because the neutrino's momentum is anti-aligned with its spin (negative helicity), we have our polarised muons. These muons are then implanted into the sample of interest before quickly decaying into a positron and two neutrinos ($\mu^+ \rightarrow e^+ + \nu_e + \bar{\nu}_\mu$). Of the three products, we can only detect the positrons, which, because the decay is a weak process (see **Figure 1.1b**) violating parity conservation [13], will be preferentially emitted in the instantaneous direction of the muon spin (see **Figure 1.4**).

Between the implantation and the decay, however, the muon will stop at a muon site (they thermalise in about 0.1–1 ns and without depolarisation since the process is electrostatic) and the spin will precess in the local magnetic field (for up to $\sim 20\,\mu s$) so that the emission direction will give us information about the sample [14]. Usually, positive muons are used in μ^+SR experiments because they will settle into regions of high electron density where measurements can be made of local magnetic fields or charge densities (through the hyperfine coupling) without the result being dominated by the positively charged nuclei. The fundamental equation for μ^+SR experiments where rotation dominates is the Larmor precession frequency

$$\omega = \gamma_\mu \|\mathbf{B}\|\,, \tag{1.1}$$

where $\gamma_\mu = 2\pi \times 135.5\,\mathrm{MHz/T}$ is the gyromagnetic ratio for the muon and $\mathbf{B}$ is the local magnetic field that it experiences. The ratio determines the rate of precession of the muon spin around the field and so sets the limit of the muon's sensitivity to magnetic fields and its ability to resolve times.

1.1.2 Experimental setup

A schematic representation of the typical setup for a μ^+SR experiment is shown in **Figure 1.2a**, where the muons are implanted into the sample with their spin antiparallel to their momentum and, after interacting with the local magnetic fields, decay and the directions of the emitted positrons are measured. Although modern experiments usually contain many detectors, when analysing the results of an experiment we normally distinguish only between forward and backward detector banks relative to the direction of the muon polarisation[1]. This means that we obtain two histograms in time for the number of positron counts $N_\mathrm{F}(t)$ and $N_\mathrm{B}(t)$ which are then combined into an asymmetry

$$A(t) = \frac{N_\mathrm{F}(t) - \alpha N_\mathrm{B}(t)}{[N_\mathrm{F}(t) + \alpha N_\mathrm{B}(t)]}\,, \tag{1.2}$$

where the parameter α is a calibration constant which accounts for the difference in detector efficiency and geometry. The asymmetry function is of particular interest because it is proportional to the time-dependent polarisation of the muon spins $P_\alpha = \langle S_\alpha(t) \rangle$, which is the expectation of the muon spin operator S_α in a direction $\alpha = x, y, z$, and so is ultimately the quantity that is modelled when analysing the results of an experiment.

Three main geometries can be used in a μ^+SR experiment: the transverse-field (TF), the zero (ZF) and the longitudinal (LF) field geometries. In the first, the external field is arranged perpendicular to the initial muon spin (z-axis) and the polarisation is measured along the x-axis. In contrast, in the second two arrangements, both the initial muon spin and the external field are oriented in the same direction, so that the polarisation of interest is also along the z-axis.

[1] This is true only in a zero or longitudinal field experiment; in a transverse field experiment more directions (e.g. up, down, left, right) are normally used for a more complete analysis of the results.

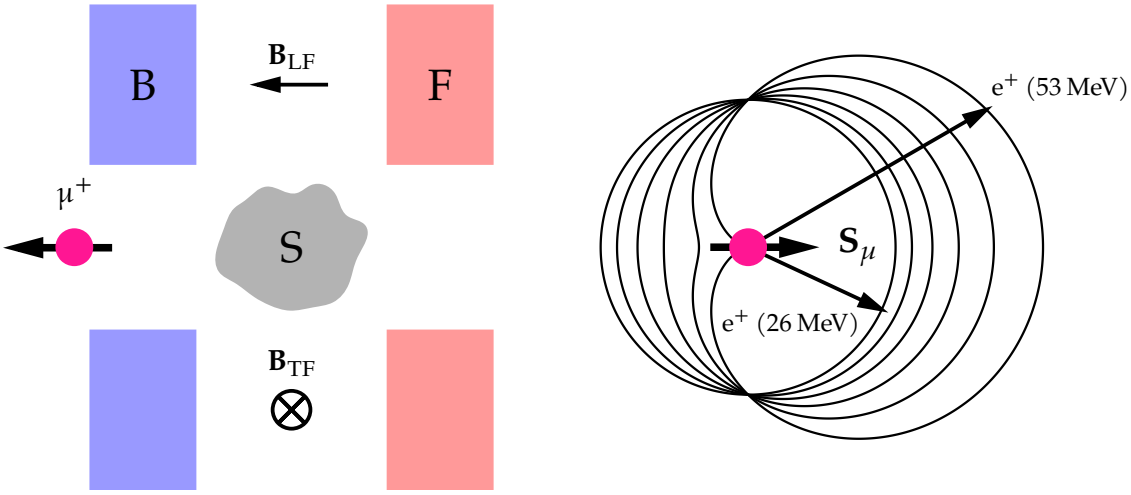

Figure 1.2 (a) Schematic diagram showing a typical μ^+SR experiment, with spin-polarised muons implanted into a sample surrounded by detectors. The magnetic field directions for the different geometries are also indicated. (b) Angular distribution of emitted positions relative to the muon spin at the time of decay for energies between $E_{\mathrm{max}}/2$ and E_{max}.

Another consideration is the type of muon source used in an experiment, distinguished by how the initial muon implantation time is determined. In a continuous muon source, only one muon is present in the sample at any given time, so that there is no ambiguity about when the decay occurs. This method has the advantage of a very high time resolution, which allows the detection of high magnetic fields at the cost of a very low count rate and short sampling windows. In contrast, in a pulsed source, a large number of muons are implanted into the sample in a short burst and assumed to be simultaneous, so that we lose time resolution, and so accessible magnetic fields, but gain in count rate and can collect data for longer. There is always a trade-off between the two approaches and both have their uses.

1.1.3 Muon sites and magnetic fields

For a given muon site with position $\mathbf{r}_\mu$, we can calculate the local magnetic field as the sum of many different contributions

$$\mathbf{B} = \mathbf{B}_{\mathrm{ext}} + \mathbf{B}_{\mathrm{dia}} + \mathbf{B}_{\mathrm{con}} + \mathbf{B}_{\mathrm{trans}} + \mathbf{B}_{\mathrm{dip}} + \mathbf{B}_{\mathrm{lor}} + \mathbf{B}_{\mathrm{dem}}\,, \tag{1.3}$$

where the different terms [15] are:

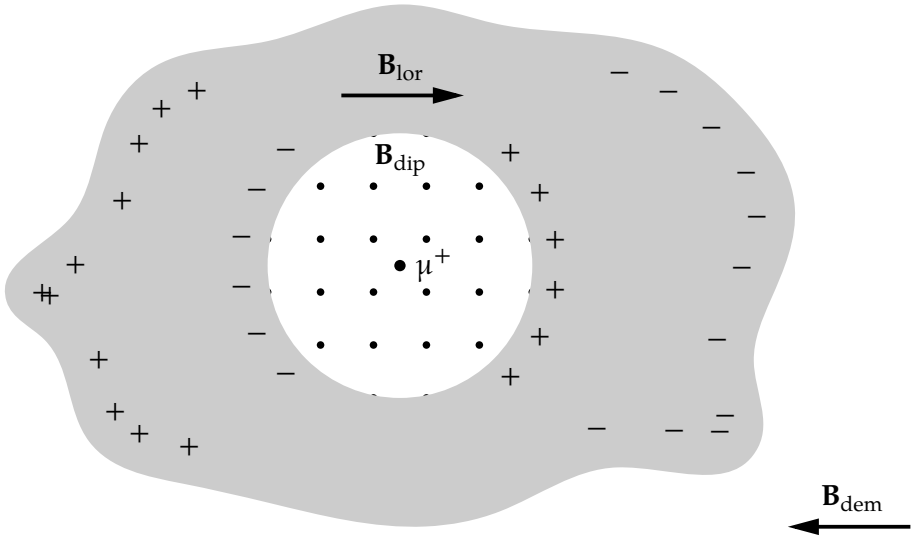

Figure 1.3 Schematic showing the calculation of dipolar fields in a sample, where the dipole field $\mathbf{B}_{\text{dip}}$ is calculated from the moments in the Lorentz sphere (in white), whilst the moments are responsible for the macroscopic $\mathbf{B}_{\text{lor}}$ and $\mathbf{B}_{\text{dem}}$ fields, caused by surface charges in the sphere and sample respectively.

- External Field ($\mathbf{B}_{\text{ext}}$): An externally applied field
- Diamagnetic Field ($\mathbf{B}_{\text{dia}}$): Induced magnetic field that opposes external field, especially important in superconductors which expel all internal fields and are perfect diamagnets.
- Contact hyperfine Field ($\mathbf{B}_{\text{con}}$): Caused by the spin density induced by the conduction electrons around the muon site [16].
- Transferred hyperfine Field ($\mathbf{B}_{\text{trans}}$): In metals, caused by the Rudermann-Kittel-Kasuya-Yosida (RKKY) interaction.
- Dipole Field ($\mathbf{B}_{\text{dip}}$): Direct lattice sum over magnetic moments in the Lorentz sphere [17]:

$$\mathbf{B}(\mathbf{r}_\mu) = \sum_i \frac{3(\mathbf{m}_i \cdot \mathbf{r}_i)\,\mathbf{r}_i}{(r_i)^5} - \frac{\mathbf{m}_i}{(r_i)^3}\,, \tag{1.4}$$

where $\mathbf{r}_i = \mathbf{R}_i - \mathbf{r}_\mu$ is the vector to each of the magnetic atoms and $\mathbf{m}_i$ is the magnetic moment of that atom.

- Lorentz Field ($\mathbf{B}_{\text{lor}}$): Caused by magnetic medium outside Lorentz sphere and given by $\mathbf{B}_{\text{lor}} = (\mu_0 \mathbf{M}_{\text{sat}})/3$, where $\mathbf{M}_{\text{sat}}$ is the saturation magnetisation [18].

- Demagnetisation Field ($\mathbf{B}_{\text{dem}}$): Caused sample edge effects and is given by $\mathbf{B}_{\text{dem}} = -\mu_0 \mathbf{N} \mathbf{M}_{\text{bulk}}$, where $\mathbf{N}$ is the demagnetising tensor and depends on the shape and $\mathbf{M}_{\text{bulk}}$ is the bulk magnetisation.

We are usually most interested in the last three terms, which are caused by the dipolar interaction between the muon spin and localised lattice spins, as shown in **Figure 1.3**.

1.1.4 Common asymmetry functions

In a muon experiment, we measure the time evolution of the average muon polarisation $P_{\mathbf{n}}(t) = \left\langle \hat{S}_{\mathbf{n}}(t) \right\rangle$ along a detector direction $\mathbf{n}$, which is given by

$$P_{\mathbf{n}} = \text{Tr}[\hat{\rho}(t)\,(\hat{\sigma} \cdot \mathbf{n})]\,, \tag{1.5}$$

where $\hat{\sigma}$ is the vector of Pauli spin matrices and $\hat{\rho}(t)$ is the density matrix, which for a time-independent Hamiltonian evolves in time as

$$\hat{\rho}(t) = \exp\left(\frac{-i\hat{H}t}{\hbar}\right)\hat{\rho}_0 \exp\left(\frac{i\hat{H}t}{\hbar}\right), \tag{1.6}$$

where $\hat{\rho}_0 = \hat{\rho}(t=0)$ is the initial value [19, 20]. If we treat the muon as an isolated system[2] where both the initial polarisation and the detector are along the z-axis we have $\hat{\rho}_0 = \left(\hat{I} + \hat{\sigma}_z\right)/2$. This means that for a diagonalisable Hamiltonian $\hat{H}|n\rangle = E_n|n\rangle$, we have

$$P_z(t) = \text{Tr}[\hat{\rho}(t)\,\hat{\sigma}_z] = \frac{1}{2}\left[\sum_{mn} |\langle m \mid \hat{\sigma}_z \mid n\rangle|^2 \cos(\omega_{mn} t)\right], \tag{1.7}$$

where $\omega_{mn} = (E_m - E_n)/\hbar$ and we have used the fact that $\text{Tr}(\hat{\sigma}_z) = 0$.

If we now consider the Hamiltonian for the muon ($S = 1/2$) in a constant magnetic field with direction (θ, ϕ), which can be expressed in a basis with the spin being aligned $|\uparrow\rangle = (1, 0)$ and anti-aligned $|\uparrow\rangle = (0, 1)$ with the z-axis, giving

$$\hat{H} = -\left(\frac{\gamma_\mu \hbar}{2}\right)(\hat{\sigma} \cdot \mathbf{B}) = -\frac{\gamma_\mu \hbar B}{2}\begin{pmatrix} \cos(\theta) & \sin(\theta)\exp(-i\phi) \\ \sin(\theta)\exp(i\phi) & -\cos(\theta) \end{pmatrix}, \tag{1.8}$$

[2] We can include the effect of the environment by considering a larger matrix using the tensor product $\rho = \rho_\mu \otimes \rho_{\text{sys}}$.

which can be diagonalised to give

$$\begin{aligned} |+\rangle &= \sin\left(\frac{\theta}{2}\right)|\uparrow\rangle - \cos\left(\frac{\theta}{2}\right)\exp(i\phi)\,|\downarrow\rangle \\ |-\rangle &= \cos\left(\frac{\theta}{2}\right)|\uparrow\rangle - \sin\left(\frac{\theta}{2}\right)\exp(i\phi)\,|\downarrow\rangle\,, \end{aligned} \tag{1.9}$$

and $E_{\pm} = \pm\gamma_\mu\hbar\,\|\mathbf{B}\|/2$, where the eigenstates represent the cases where the spin is aligned and anti-aligned with the external field respectively. And so finally substituting back into **Equation 1.7** we arrive at

$$P_z(t) = \cos(\theta)^2 + \sin(\theta)^2\cos\left(\gamma_\mu\|\mathbf{B}\|t\right)\,. \tag{1.10}$$

Since we chose to measure along the z-axis without loss of generality, this result applies to any measurement direction $\mathbf{n}$ as long as the angle θ is measured between this axis and the field $\mathbf{B}$ (see **Figure 1.4** for a diagram of the geometry).

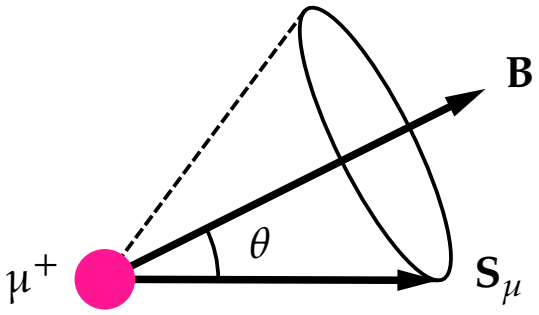

Figure 1.4 Precession of the muon spin $\mathbf{S}_\mu$ around a static magnetic field $\mathbf{B}$, describing a cone with semi-angle θ.

We can then generalise to a probability distribution of magnetic fields $p(\mathbf{B})$ by taking an integral

$$P_{\mathbf{n}}(t) = \int p(\mathbf{B})\left[\cos(\theta)^2 + \sin(\theta)^2\cos\left(\gamma_\mu\|\mathbf{B}\|t\right)\right]d^3\mathbf{B}\,, \tag{1.11}$$

which for a polycrystalline sample where the field distribution is isotropic, so that $p(\mathbf{B}) = p(\|\mathbf{B}\|)$, gives

$$P_{\mathbf{n}}(t) = \int 4\pi\|\mathbf{B}\|^2 p(\|\mathbf{B}\|)\left[\frac{1}{3} + \frac{2}{3}\cos\left(\gamma_\mu\|\mathbf{B}\|t\right)\right]d\|\mathbf{B}\|\,. \tag{1.12}$$

1.1.4.1 Static field distributions

Three common cases of particular interest for ZF μ^+SR experiments [12]:

- When the muons in a powder sample are subject to a finite number of fields with random directions but magnitudes B_i and probabilities p_i, so that we have $p(B) = \sum p_i \delta(B - B_i)$, the integral in the previous section gives

$$P_z(t) = \frac{1}{3} + \frac{2}{3}\left[\sum_i p_i \cos(\gamma_\mu B_i t)\right]. \tag{1.13}$$

- For a disordered material where each field component is given by an independent Gaussian distribution with standard deviation $\sigma = \Delta/\gamma_\mu$ and zero mean, which in many cases can be justified by the central limit theorem[3], we obtain the Kubo-Toyabe relaxation function [21]

$$\begin{aligned} P_z(t) &= \frac{1}{3} + \frac{2}{3}\left[\frac{(\gamma_\mu)^2}{2\pi\Delta^2}\right]^{\frac{3}{2}}\left[\int_0^\infty 4\pi B^2 \exp\left[-\frac{(\gamma_\mu)^2 B^2}{2\Delta^2}\right]\cos(\gamma_\mu B t)\, dB\right] \\ &= \frac{1}{3} + \frac{2}{3}(1 - \Delta^2 t^2)\exp\left(-\frac{\Delta^2 t^2}{2}\right). \end{aligned} \tag{1.14}$$

  Note that the function initially resembles a Gaussian, since its Taylor expansion for small times is parabolic, which is the only part that can sometimes be observed experimentally.

- Similarly, in a material which is ordered magnetically so that the field distribution is Gaussian but with mean value of B_m we have

$$P_z(t) = \frac{1}{3} + \frac{2}{3}\exp\left(-\frac{\Delta^2 t^2}{2}\right)\cos(\gamma_\mu B_m t). \tag{1.15}$$

- We can also consider the incommensurate case where the field varies in space as $B(x) = B_0 \cos(kx)$ [22,23], so that defining $\phi = kx$ we have

$$p(B) = \left(\frac{1}{2\pi}\right)\left(\int_0^{2\pi} \delta[B_0\cos(\phi) - B]\, d\phi\right) = \frac{1}{\pi}\frac{1}{\sqrt{(B_0)^2 - B^2}}, \tag{1.16}$$

  and the corresponding polarisation function is

$$P_z(t) = \frac{1}{\pi}\left[\int_{-B_0}^{-B_0} d\frac{\cos(\gamma_\mu B t)}{\sqrt{(B_0)^2 - B^2}}\right] = J_0(\gamma_\mu B t), \tag{1.17}$$

[3] This theorem states that under certain conditions the mean of many independent and identical random variables with arbitrary distribution will tend to a Gaussian distribution.

where $J_0(x)$ is the zero-order Bessel function of the first kind, which can be approximated for $x \gg 1$ as

$$P_z(t) = J_0(\gamma_\mu B t) \approx \sqrt{\frac{2}{\pi \gamma_\mu B_0 t}} \cos\left(\gamma_\mu B t - \frac{\pi}{4}\right). \tag{1.18}$$

1.1.4.2 Dynamic field distributions

Up until now, we have considered only the asymmetry due to static fields, which is a valid assumption when dealing with static electronic moments and all nuclear moments (since they have a relaxation time $\sim 35\,\mu s$ much larger than the muon lifetime) [24]. A different approach is needed, however, when accounting for muon diffusion or other effects that lead to a time-varying local field. The process by which the change happens is usually assumed to be Gaussian and Markovian, meaning that the next value depends only on the current one and is sampled from a Gaussian distribution centred around it [12].

The simplest method of obtaining a dynamic polarisation function is to use the strong collision approximation, where we assume that the muon spin evolves in a static field which changes suddenly after certain times t_i. These times are distributed according to $p(t) \propto \exp(-t/\tau)$ so that τ is the mean time between changes (collisions) and after each one the polarisation resets to $P_z(t - t_i)$. This process then allows us to transform a static asymmetry function into a dynamic one. Applying this to the Kubo-Toyabe relaxation described in the previous section and using the fast fluctuation limit $\nu/\Delta \gg 1$ we have

$$\begin{aligned} P_z(t) &= \exp\left(\frac{-2\Delta^2}{\nu}\left[\exp(-\nu t) - 1 - \nu t\right]\right) \\ &\simeq \exp(-\lambda t) \quad \text{where} \quad \lambda = \frac{2\Delta^2}{\nu}, \end{aligned} \tag{1.19}$$

where $\nu = \tau^{-1}$ is the fluctuation rate and we expect that $\Delta = \sqrt{\gamma_\mu^2 \langle (B - \langle B \rangle)^2 \rangle}$ in this limit. We also find that as the fluctuation rate increases the relaxation decreases, an effect known as motional narrowing, because the muon spins can't precess fast enough in the rapidly changing field.

1.1.4.3 Muon-fluorine entangled states

In some cases, the assumption of an isolated quantum system used to derive **Equation 1.11** is not applicable and the quantum entanglement of the muon with other nuclei must be

considered to calculate the polarisation. A common case of this is the interaction of the muon with fluorine atoms [25], which must be simulated using the density matrix formalism. Consider the case of a single fluorine atom with a dipolar interaction [26] so that the Hamiltonian is:

$$\begin{aligned}\hat{H} &= \underbrace{\left(\frac{\mu_0\hbar^2\gamma_\mu\gamma_F}{4\pi r^3}\right)}_{\hbar\omega_\mathrm{d}}\frac{1}{4}\left[\boldsymbol{\sigma}_\mu\cdot\boldsymbol{\sigma}_F - 3\left(\boldsymbol{\sigma}_\mu\cdot\hat{\mathbf{r}}\right)\left(\boldsymbol{\sigma}_F\cdot\hat{\mathbf{r}}\right)\right] \\ &= \left(\frac{\hbar\omega_\mathrm{d}}{2}\right)\begin{pmatrix} -1 & 0 & 0 & 0 \\ 0 & 1 & 1 & 0 \\ 0 & 1 & 1 & 0 \\ 0 & 0 & 0 & -1 \end{pmatrix},\end{aligned} \tag{1.20}$$

where $\mathbf{r}$ is the vector between the positions of the muon and fluorine, with $r = \|\mathbf{r}\|$ and $\hat{\mathbf{r}} = \mathbf{r}/\|\mathbf{r}\|$. This means that the polycrystalline polarisation is given by:

$$P_z(t) = \frac{1}{6}\left[1 + \cos(\omega_\mathrm{d}t)\right] + \frac{1}{3}\left[\cos\left(\frac{\omega_\mathrm{d}t}{2}\right) + \cos\left(\frac{3\omega_\mathrm{d}t}{2}\right)\right]. \tag{1.21}$$

A similar analysis can be applied to the common $\mathrm{F}-\mu-\mathrm{F}$ case, where we have a muon between two fluorine atoms [27–29]. This gives a 8×8 Hamiltonian, which ignoring the interaction between the fluorine atoms and assuming a straight bond can be solved to obtain

$$\begin{aligned}P_z(t) = \frac{1}{6}\Bigg(3 + \cos\left(\sqrt{3}\omega_\mathrm{d}t\right) + \left(1 - \frac{1}{\sqrt{3}}\right)\cos\left[\left(\frac{3-\sqrt{3}}{2}\right)\omega_\mathrm{d}t\right] \\ + \left(1 + \frac{1}{\sqrt{3}}\right)\cos\left[\left(\frac{3+\sqrt{3}}{2}\right)\omega_\mathrm{d}t\right]\Bigg),\end{aligned} \tag{1.22}$$

where we have a signal with three distinct related frequencies.

1.1.5 Avoided level crossing resonances

The avoided level crossing (ALC) μ^+SR technique uses muonium, which is formed when an implanted muon captures an electron to make a hydrogen atom analogue, to probe the energy levels of a system. The muonium will usually combine with a radical (a reactive part of the system with at least one unpaired electron), interacting through terms like the hyperfine or quadrupolar interaction with nearby electrons, protons and atoms to

form a quantised system whose energy levels can be tuned by applying an external magnetic field [30]. This can induce avoided level crossings where mixing occurs between the eigenstates of two levels, which appears in the time-integrated polarisation as a resonance when scanning through the applied field. We can then extract information about the system from the shape and location of the peaks, like the strength of the coupling responsible or dynamics in the system.

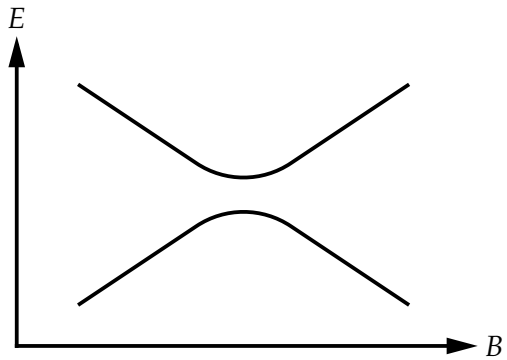

Figure 1.5 Schematic of an avoided crossing in energy levels as a function of the applied external magnetic field.

We start with the same expression for the polarisation in terms of the density matrix formalism described in **Section 1.1.4**, with the additional simplification that the strong applied magnetic fields means that the oscillations will be too fast to be measured experimentally, and so only terms with $E_n = E_m$ (i.e. a level crossing) will contribute [31]:

$$P_z(t) = \mathrm{Tr}[\hat{\rho}(t)\,\hat{\sigma}_z] = \frac{1}{2}\left[\sum_{mn}\langle m \mid \hat{\sigma}_z \mid n\rangle \left\langle m \mid \hat{\rho}_0 \mid n\right\rangle \delta(E_n - E_m)\right], \tag{1.23}$$

where $\delta(x)$ is the Dirac delta function which is only non-zero when $x = 0$. Since we are also no longer dealing with an isolated system we also use the Kronecker matrix product, defined as

$$A \otimes B = \begin{pmatrix} a_{11}B & \dots & a_{1n}B \\ \vdots & \ddots & \vdots \\ a_{m1}B & \dots & a_{mn}B \end{pmatrix}, \tag{1.24}$$

to construct operators that act on the combined system. This means that for a system of n particles with dimensions $p_1, \dots, p_n$ the j-th particle has spin operators

$$S_j^\alpha = I_{p_1} \otimes \dots \otimes S_{p_j}^\alpha \otimes \dots I_{p_n}, \tag{1.25}$$

where I_n is an identity matrix of size $n \times n$ and $\alpha = x, y, z$. In the simplest case we consider Zeeman Hamiltonian terms describing the effect of the applied magnetic field

$$\hat{H}_j^{\mathrm{Z}} = -\sum_{\alpha} \gamma_\mu \mathbf{B}_\alpha S_j^\alpha \,, \tag{1.26}$$

and hyperfine terms describing pairwise interactions between spins

$$\hat{H}_{ij}^{\mathrm{HF}} = \sum_{\alpha\beta} A_{\alpha\beta} S_i^\alpha S_j^\beta \,, \tag{1.27}$$

where the hyperfine tensor $A_{\alpha\beta}$ describes a general anisotropic coupling.

1.2 Density functional theory

The locations of muon stopping sites in a material are in general expected to be close to the local minima in the electrostatic potential and so as a first approximation, this potential can be constructed from the atomic positions [32] to calculate the sites. This method is very inexpensive computationally and gives good results in systems like metals, where the delocalised electrons shield the muon from the atoms and so prevent any large distortions. Unfortunately, this effect is not present in insulators or semiconductors and so this approach, which ignores the effect of the muon on the atomic positions and the quantum nature of the electrons, is not sufficient [7].

Instead, a more expensive full *ab initio* electronic structure calculation might be preferred or even required. This thesis focuses on using the framework of DFT, which has seen great advancements in recent years, to do this. The main idea is to solve the many-body Schrödinger equation for the electrons by minimising an energy functional of the electron density, which can be used to completely determine the ground state wavefunction. To locate the stopping site of the muon and account for its effect on the other atoms geometry optimisation is also employed to minimise the energy of the system with respect to the atomic positions (see **Section 1.2.5.1**).

1.2.1 Hohenberg-Kohn theorems

The objective of DFT is to solve the Schrödinger equation for a system of N interacting electrons

$$\left[\sum_i^N \frac{-\nabla_i^2}{2} + \frac{1}{2}\left(\sum_{i\neq j} \frac{1}{\|\mathbf{r}_i - \mathbf{r}_j\|}\right) + \sum_i V_{\text{ne}}(\mathbf{r}_i)\right]\psi(\mathbf{r}_1, \dots, \mathbf{r}_N) = E\psi(\mathbf{r}_1, \dots, \mathbf{r}_N)\,, \tag{1.28}$$

where ∇_i^2 is the Laplacian with respect to the position of the i-th electron $\mathbf{r}_i$ and $V_{\text{ne}}(\mathbf{r})$ is the external electrostatic potential on the electrons due to the atomic nuclei. We usually make the simplifying assumption that the nuclei have classical positions and are fixed with respect to the electronic motion (called the Born-Oppenheimer approximation). This is justified by the observation that the nuclear masses are many times greater than the electron mass and so their kinetic energy term in the Hamiltonian can be neglected [33]. To simplify the notation, we will only consider the real-space part of the wavefunction $\psi(\mathbf{r}_1, \dots, \mathbf{r}_N)$ here.

The ground state of the system can be found by applying a variational principle on the energy with respect to the single-particle density, which is defined as:

$$\begin{aligned} \rho(\mathbf{r}) &= \int d\mathbf{r}_2 \ \dots \int d\mathbf{r}_N \, |\psi(\mathbf{r}_1, \dots, \mathbf{r}_N)|^2 \\ \text{where} \quad &\int \rho(\mathbf{r})\, d\mathbf{r} = N \quad \text{and} \quad \rho(\mathbf{r}) \geq 0\,. \end{aligned} \tag{1.29}$$

This quantity is much simpler than the $3N$-dimensional many-body wavefunction $\psi(\mathbf{r}_1, \dots, \mathbf{r}_N)$ but is related to it by the Hohenberg-Kohn theorems [34], which state that the wavefunction is uniquely determined by the potential (**Theorem 1.1**) and that the density uniquely determines the wavefunction (**Theorem 1.2**). This means that given an external potential we can find a unique ground state charge density.

Theorem 1.1. *Different potentials $\hat{V}(\mathbf{r})$ and $\hat{V}'(\mathbf{r})$ lead to different ground states ψ and ψ' (with $\hat{V} \neq \hat{V}' + c$).*

We proceed by contradiction, subtracting the two equations assuming that the wavefunctions are equal:

$$\begin{cases} \hat{H}\psi = E\psi \\ \hat{H}'\psi' = E'\psi' \end{cases} \rightarrow \left(\hat{V} - \hat{V}'\right)\psi = \lambda\psi\,. \tag{1.30}$$

Since we specified that the potentials differ by more than a constant, $\hat{V} - \hat{V}'$ cannot be equal to λ.

Theorem 1.2. *Different wavefunctions ψ and ψ' lead to different densities ρ and ρ'.*

Assuming that the two states are not degenerate, we have that:

$$\begin{cases} \langle \psi \mid \hat{H} \mid \psi \rangle < \langle \psi' \mid \hat{H} \mid \psi' \rangle \\ \langle \psi' \mid \hat{H}' \mid \psi' \rangle < \langle \psi \mid \hat{H}' \mid \psi \rangle \end{cases} \rightarrow \int \left(\hat{V} - \hat{V}'\right)(\rho - \rho')\, d\mathbf{r} < 0\,. \tag{1.31}$$

So that if $\rho = \rho'$ we have a contradiction.

We can now define the total energy functional to be minimised, distinguishing between the internal energy functional $F[\rho]$, containing the kinetic energy T and the electron-electron interaction V_{ee}, and a term that depends on the external field

$$E[\rho] = F[\rho] + \int \rho(\mathbf{r})\, V(\mathbf{r})\, d\mathbf{r}\,. \tag{1.32}$$

For any other density $\rho'(\mathbf{r})$ we have $E \leq E[\rho']$ so that the ground state can be found by minimising the energy:

$$\begin{aligned} E_0 &= \min_{\psi \to N} \langle \psi \mid \hat{H} \mid \psi \rangle \\ &= \min_{\rho \to N} \left[\min_{\psi \to \rho} \langle \psi \mid \hat{T} + \hat{V}_{\text{ee}} \mid \psi \rangle + \int \rho(\mathbf{r})\, V_{\text{ne}}(\mathbf{r})\, d\mathbf{r} \right] \\ &= \min_{\rho \to N} \left[F[\rho] + \int \rho(\mathbf{r})\, V_{\text{ne}}(\mathbf{r})\, d\mathbf{r} \right] \\ \rightarrow \frac{\delta F}{\delta \rho} &+ V_{\text{ne}} - \mu = 0\,, \end{aligned} \tag{1.33}$$

where μ is an arbitrary constant that arises from using the method of Lagrange multipliers to fix the total number of electrons. This means that solving the Schrödinger equation has been expressed as a constrained minimisation problem, which can be further simplified by separating the interacting electrons.

1.2.2 Kohn-Sham equations

To approximate the value of $F[\rho]$, and especially the kinetic energy $\hat{T}[\rho]$, for minimisation Kohn and Sham [35] used a non-interacting fictitious system with the same charge density $\rho(\mathbf{r})$. This means that the energy functional now becomes

$$\begin{aligned} F[\rho] &= T[\rho] + E_{\text{ee}}[\rho] \\ &= T_{\text{S}}[\rho] + \underbrace{\frac{1}{2}\left[\iint \frac{\rho(\mathbf{r})\rho(\mathbf{r}')}{\|\mathbf{r}-\mathbf{r}'\|} d\mathbf{r}\, d\mathbf{r}'\right]}_{E_{\text{H}}[\rho]} + E_{\text{xc}}\,, \end{aligned} \tag{1.34}$$

where we separated the mean-field part of E_{ee} into a Hartree term E_{H} and collected the rest of our ignorance about the electronic interactions into the exchange-correlation functional

$$E_{\text{xc}} = T[\rho] - T_{\text{S}}[\rho] + E_{\text{ee}}[\rho] - E_{\text{H}}[\rho]\,. \tag{1.35}$$

This means that we can define the Kohn-Sham kinetic energy T_{S} in terms of the single-particle wavefunctions ϕ_i, which depend on the density, giving

$$T_S[\rho] = -\frac{1}{2}\left(\sum_{i=0}^{N} \int \phi_i^*(\mathbf{r}) \left[\nabla^2 \phi_i(\mathbf{r})\right] d\mathbf{r}\right), \tag{1.36}$$

and so the problem can be recast using a fictitious potential V_S through which each electron experiences the effect of the others by minimising **Equation 1.34** to get

$$V_{\text{S}}(\mathbf{r}) = V_{\text{ne}}(\mathbf{r}) + \underbrace{\frac{1}{2}\left[\int \frac{\rho(\mathbf{r}')}{\|\mathbf{r}-\mathbf{r}'\|} d\mathbf{r}'\right]}_{V_{\text{H}}} + V_{\text{xc}}(\mathbf{r}) + \mu''\,, \tag{1.37}$$

where μ'' is a second arbitrary constant related to μ'.

We now compute the ground state density using a self-consistent field procedure by starting with a trial $\rho(\mathbf{r})$ from which we can compute $V_S(\mathbf{r})$. The Kohn-Sham orbitals are then solved to obtain a new estimate and the procedure repeated until the calculation converges. The Kohn-Sham independent Schrödinger equation to solve is

$$\left[\frac{-\nabla^2}{2} + V_{\text{S}}(\mathbf{r})\right]\phi_n = \epsilon_n \phi_n\,, \tag{1.38}$$

and from the Slater determinant description of the wavefunction, the electron density is given by

$$\rho(\mathbf{r}) = \sum_n f_n |\phi_n(\mathbf{r})|^2\,, \tag{1.39}$$

where we sum over the orbitals ϕ_i each with occupancy $f_i \in [0, 1]$. We can then use the Kohn-Sham energies ϵ_n to estimate the band structure of the material, although the

results are not very accurate with quantities like band gaps consistently underestimated [36].

1.2.3 Exchange-correlation functionals

Except for the exchange-correlation term $E_{xc}[\rho]$, the DFT formulation of many-body quantum mechanics is exact (up to the details of the numerical implementation), and so having concentrated all of our ignorance here, a useful calculation requires a good approximation for it:

$$E_{\mathrm{xc}}[\rho] = F[\rho] - T_{\mathrm{S}}[\rho] - \frac{1}{2}\left[\iint \frac{\rho(\mathbf{r})\,\rho(\mathbf{r}')}{\|\mathbf{r}-\mathbf{r}'\|}\,d\mathbf{r}\,d\mathbf{r}'\right]. \tag{1.40}$$

The simplest functional, which is nonetheless quite effective and very cheap computationally is the Local Density Approximation (LDA), where we treat the electrons as locally homogeneous and use the E_{xc} of a uniform electron gas [37]

$$E_{\mathrm{xc}}[\rho] = \int \rho(\mathbf{r})\, e_{\mathrm{xc}}^{\mathrm{LDA}}[\rho(\mathbf{r})]\,d\mathbf{r}\,. \tag{1.41}$$

The exchange contribution can be solved analytically but not the correlation one, so very accurate simulations performed using Quantum Monte Carlo methods must be used to determine $e_{\mathrm{xc}}^{\mathrm{LDA}}$ [38].

We can improve the LDA result by taking the gradient of the density $\nabla\rho$ at the point into account to obtain the Generalised Gradient Approximation (GGA) $e_{\mathrm{xc}}^{\mathrm{GGA}}[\rho(\mathbf{r}), \nabla\rho(\mathbf{r})]$, providing a semi-local approximation that is still quite fast. Many different parametrisations of GGA exist; we usually distinguish between empirical functionals constructed to be accurate for certain classes of materials from experimental data[4] and functionals constructed to preserve certain quantities and obey certain physical scaling laws[5]. In general, we find that GGA functionals are more accurate than LDA but tend to under-bind molecules and atoms instead of over-binding like LDA. More complicated functionals can be obtained by using higher derivatives of the density and including the kinetic energy density (meta-GGA) but the returns are diminishing and calculations become more expensive [37]. Some other examples are non-local functionals, which explicitly make use

[4] The most famous being B3LYP (Becke, 3-parameter, Lee–Yang–Parr) for molecular systems [39].
[5] An example is PBE (Perdew-Burke-Ernzerhof), which is commonly used for crystals [40].

of information at other points instead of just derivatives at the cost of much more computation, and functionals constructed by fitting to experimental data, which are not very general but can give very good results (see [41] for a review).

1.2.4 Practicalities and convergence

There are multiple ways of calculating the ground state of a system using DFT but a popular method for periodic crystals (and implemented in CASTEP [8]) involves defining the wavefunction in terms of a plane wave basis set and then using the conjugate gradients method with respect to the Fourier coefficient vector to obtain the ground state [42].

1.2.4.1 Plane-wave basis set

One complication of solving the Schrödinger equation for a crystal is that we have a practically infinite number of unit cells to consider. We can overcome this by taking advantage of the periodicity of the system in real space, since by definition a crystal is composed of infinitely repeating unit cells we can calculate macroscopic quantities by considering only the electrons in a single cell.

Theorem 1.3 (Bloch's theorem)**.** *The solutions to the Schrödinger equation for any periodic potential V can be expressed as plane waves modulated by a periodic Bloch function $u(\mathbf{r})$:*

$$\psi(\mathbf{r}) = \exp[i(\mathbf{k}\cdot\mathbf{r})]\,u(\mathbf{r})\ . \tag{1.42}$$

A derivation can be found in **Appendix A** and the result is used to write the Block functions $u_{n\mathbf{k}}(\mathbf{r})$, which are periodic in space, as a Fourier series, giving

$$\psi_{n\mathbf{k}}(\mathbf{r}) = \sum_{\mathbf{G}} c_{n\mathbf{k}+\mathbf{G}} \exp(i[(\mathbf{k}+\mathbf{G})\cdot\mathbf{r}])\ . \tag{1.43}$$

This reduces the problem of an infinite number of electrons to a calculation over a discrete but still infinite set of $\mathbf{k}$ points and $\mathbf{G}$ vectors for the basis. We can then proceed by introducing a plane-wave energy cut-off E_c by considering that terms $c_{n,\mathbf{k}+\mathbf{G}}$ with lower energy $\|\mathbf{k}+\mathbf{G}\|^2/2$ will contribute more to the final result, since ϕ is assumed to be relatively smooth and so the high frequency components will contribute less. The plane wave with the largest value of $\mathbf{G}$ then is

$$\frac{1}{2}\|\mathbf{k}+\mathbf{G}\|^2 \leq E_{\mathrm{c}}\,. \tag{1.44}$$

1.2.4.2 Brillouin zone sampling

Although Bloch's theorem makes DFT calculations possible, we still have an infinite number of **k**-points at which the wavefunction must be considered. This can be resolved by making the approximation that the wavefunction varies smoothly in **k**-space, and so we only need to sample at a finite number of points

$$F = \left[\frac{\Omega_{\mathrm{cell}}}{(2\pi)^3}\right]\left[\int f(\mathbf{k})\,d^3\mathbf{k}\right] = \sum_i w_i f(\mathbf{k}_i)\,, \tag{1.45}$$

where Ω_{cell} is the volume of the unit cell and the special points $\mathbf{k}_i$ have weights w_i which depend on the number of other symmetry-equivalent points. A general method for choosing the points of an $N_1 \times N_2 \times N_3$ grid was suggested by Monkhorst and Pack [43], using an expression of the form

$$\mathbf{k}_{n_1 n_2 n_3} = \sum_i^3 \left(\frac{2n_i N_i - 1}{2N_i}\right)\mathbf{b}_i\,, \tag{1.46}$$

where $\mathbf{b}_i$ are the reciprocal lattice vectors and $n_i = 1, \ldots, N_i$ giving a total of $\prod_i N_i$ points.

1.2.4.3 Energy minimisation

Given all the details described above, we are now left with the task of calculating the total energy of the system. Using a plane-wave basis, the Kohn-Sham equations can be expressed as a non-linear eigenvalue problem of the form

$$\sum_{\mathbf{G}'}\Big[\frac{1}{2}\|\mathbf{k}+\mathbf{G}\|^2\,\delta_{\mathbf{G}\mathbf{G}'} + V_{\mathrm{ee}}(\mathbf{G}-\mathbf{G}') + V_{\mathrm{ne}}(\mathbf{G}-\mathbf{G}') + V_{\mathrm{xc}}(\mathbf{G}-\mathbf{G}')\Big]c_{n\mathbf{k}+\mathbf{G}'} = \epsilon_i c_{n\mathbf{k}+\mathbf{G}}\,, \tag{1.47}$$

where the potentials depend on the eigenvectors (orbitals) through the electron density $\rho(\mathbf{r})$. The problem then has to be solved by an iterative procedure called a self-consistent field (SCF) calculation, where at each step we construct the Hamiltonian for a given density, solve the corresponding eigenvalue problem and then use the result to calculate a new density, repeating until a fixed point is reached [44].

We could directly diagonalise the Hamiltonian at each iteration, but the number of plane-waves required to accurately describe most physical systems makes this too expensive in most cases. Since most of the eigenstates will be unoccupied and we only need to compute one for each electron, a more performant approach is to minimise the energy with respect to the occupied Kohn-Sham orbitals, and so ultimately the plane wave coefficients, under the constraint that the orbitals must remain orthonormal. Two common iterative methods of performing the minimisation are:

- Steepest Descent (SD): We always move in the direction of greatest change in the function value given by the gradient ($\Delta\mathbf{x} = -\eta\nabla F$). This results in a fast and simple method but doesn't guarantee convergence of the minimisation.

- Conjugate Gradient Descent (CG): Instead of always moving in the steepest direction, at each iteration we pick a search direction linearly independent from all previous directions using the Gram-Schmidt procedure, ensuring that we need at most one step per dimension of the problem to reach the minimum [45].

During each iteration of the SCF procedure, we can decide whether to keep the density and orbitals consistent with each other, producing a trade-off between performance and stability in the calculation:

- Density Mixing (DM): Update the density only once per SCF cycle, mixing with the previous value to prevent instabilities. This gives a fast method which might not always converge properly with the default mixing parameters.

- Ensemble DFT (EDFT): Recalculate the density every time the wavefunctions or occupancies change, giving a slower but more stable method where the energy always decreases at each step [46].

Some of the muon site calculations presented in this thesis required the more expensive EDFT method, most likely because the SCF convergence of the calculation is very sensitive to the hydrogen defect state caused by adding the muon.

1.2.4.4 Pseudopotentials

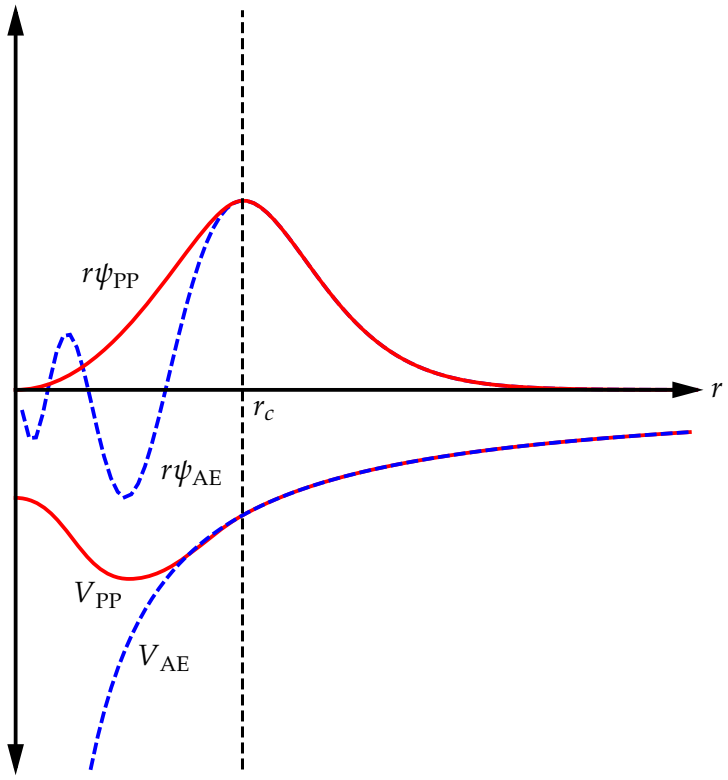

Figure 1.6 Schematic of pseudopotential (V_{PP}) and resulting wavefunction (ψ_{PP}) compared to the exact all-electron potential (V_{AE}) and wavefunction ψ_{AE}.

It has been shown that by using Bloch's theorem with a plane-wave basis with an energy cut-off and careful sampling of the Brillouin zone at a finite number of **k**-points it becomes possible to solve the Schrödinger equation for a crystal. Unfortunately, since the plane-wave basis makes no assumptions about the shape of the orbitals, a prohibitively high value of the energy cut-off is required to describe the rapid variation in the wavefunction close to the nuclei due to the steep Coulomb potential.

Recognising that valence electrons far from the nuclei contribute much more to the physical properties of interest than electrons close to the core, we can introduce an effective pseudopotential which matches the Coulomb potential outside some cut-off radius r_c but produces a smoother wavefunction in the core region, requiring fewer plane-waves.

- Norm-conserving (NCP): A potential which produces the same charge density $n(\mathbf{r})$ as the all-electron potential outside the core region.

- Ultrasoft (USP): A potential where norm-conservation is relaxed, allowing charge density to be moved outside the core region by using an auxiliary function [47].

In general, Ultrasoft potentials offer both better performance and higher accuracy, and so unless stated otherwise all calculations in this thesis used the on-the-fly USP generated by CASTEP.

1.2.4.5 Convergence testing

Using DFT provides a first-principles method of solving the electronic structure of a physical system, but any calculation involves a series of approximations, where we distinguish between physical (e.g. Born-Oppenheimer, XC functional) and numerical ones. The second arise from the practical implementation of the method and require the convergence of a series of parameters to ensure that the results are reliable.

The two most important parameters to converge in a DFT+μ calculation with CASTEP are:

- Energy cut-off (E_c): Determines the size of the plane-wave basis set and so how accurately the shape of the wavefunction can be calculated (see **Section 1.2.4.1**). We usually find that energy differences (and the properties that depend on them) converge more quickly than the energies themselves. This is because higher energy plane waves contribute more to the wavefunction the near nuclei than to bonding between atoms and we get cancellation of errors.

- **k**-point grid size: This usually depends on the parameters that generate the Monkhorst-Pack sampling grid used (see **Section 1.2.4.2**) and determines how well the Brillouin zone is sampled. To ensure that values are transferable between systems like with E_c, we sometimes consider the minimum spacing between sampled **k**-points instead of the grid size itself.

When performing a convergence test we usually vary the value of each parameter to increase the accuracy of a calculation (which also increases its computational cost) to determine when the error in the total energy or forces falls below a certain threshold. Fortunately, in the case of the two parameters mentioned previously, calculations can be converged independently by using a cheaper value in one when determining the optimal value for the other. An example of a convergence test for a unit cell containing carbon can

be found in **Figure 1.7**, showing the error in the total energy decrease as we increase the cut-off energy E_c.

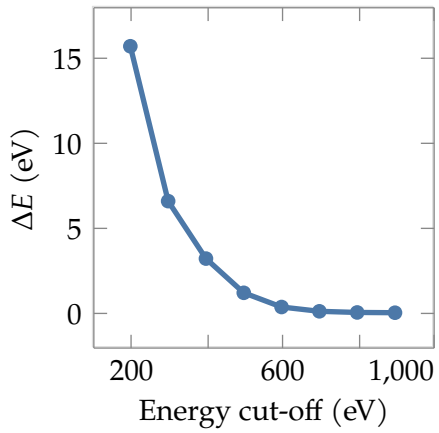

Figure 1.7 Convergence testing of E_c for pure carbon showing the error in the total energy.

1.2.5 Force, vibrations and barriers

1.2.5.1 Geometry Optimisation

We can obtain optimised atomic positions in a local energy minimum from a DFT calculation by performing a geometry optimisation of the unit cell, where the energy is minimised with respect to the atomic positions by calculating the forces on each atom using the Feynman-Hellman theorem [48] and then adjusting positions and iterating until the unit cell is relaxed.

Theorem 1.4 (Feynman-Hellman theorem)**.** *Given an eigenstate $\hat{H}_\lambda|\psi_\lambda\rangle = E_\lambda|\psi_\lambda\rangle$, the derivative of an eigenvalue energy with respect to a parameter λ is given by:*

$$\frac{dE_\lambda}{d\lambda} = \left\langle \psi_\lambda \left| \frac{d\hat{H}_\lambda}{d\lambda} \right| \psi_\lambda \right\rangle . \tag{1.48}$$

We start by using the fact that $\langle \psi_\lambda \mid \psi_\lambda \rangle = 1$, we have

$$\frac{d}{d\lambda}\langle \psi_\lambda \mid \psi_\lambda \rangle = \left\langle \psi_\lambda \left| \frac{d\psi_\lambda}{d\lambda} \right\rangle + \left\langle \frac{d\psi_\lambda}{d\lambda} \right| \psi_\lambda \right\rangle = 0 , \tag{1.49}$$

so that by differentiating the energy eigenvalue E_λ we find

$$\begin{aligned}\frac{dE_\lambda}{d\lambda} &= \frac{d}{d\lambda}\left\langle \psi_\lambda \mid \hat{H}_\lambda \mid \psi_\lambda \right\rangle \\ &= \Bigg\langle \frac{d\psi_\lambda}{d\lambda} \Big| \underbrace{\hat{H}_\lambda \Big| \psi_\lambda \Big\rangle}_{\epsilon|\psi_\lambda\rangle} + \underbrace{\Big\langle \psi_\lambda \Big| \hat{H}_\lambda}_{\epsilon\langle\psi_\lambda|} \Big| \frac{d\psi_\lambda}{d\lambda} \Bigg\rangle + \left\langle \psi_\lambda \left| \frac{d\hat{H}_\lambda}{d\lambda} \right| \psi_\lambda \right\rangle \\ &= \left\langle \psi_\lambda \left| \frac{d\hat{H}_\lambda}{d\lambda} \right| \psi_\lambda \right\rangle . \end{aligned} \tag{1.50}$$

By treating each of the three position coordinates for each atom as a parameter, the force on the I^{th} nucleus is given by

$$\mathbf{F}_I = -\frac{\partial E}{\partial \mathbf{R}_I} = \left\langle \Psi_{\mathbf{R}_I} \left| -\frac{\partial \hat{H}}{\partial \mathbf{R}_I} \right| \Psi_{\mathbf{R}_I} \right\rangle, \tag{1.51}$$

where $\mathbf{R}_I$ is the position of the I^{th} nucleus and $|\Psi_{\mathbf{R}_I}\rangle$ the electronic wavefunction parametrised by all the atomic positions. This means that having performed a single-point DFT calculation to obtain the ground state energy, the forces can be easily determined without considering derivatives of the Kohn-Sham orbitals but of only the Hamiltonian, many terms of which can be effectively evaluated.

The procedure described above to calculate the ground state atomic positions using the Feynman-Hellman theorem is also the basis for finding the classical muon stopping sites in a material. This is done by performing a geometry optimisation with an additional hydrogen atom with a smaller mass representing the muon. Since there are many possible sites, the result depends on the initial position of the muon in the simulation cell. This means that we can either predict the most likely positions (i.e. next to electronegative atoms or in positions where one would find a hydrogen atom) or perform a series of calculations with random initial positions to sample all possible sites (more details can be found in **Section 1.3**).

1.2.5.2 Phonons

Many properties of a material are determined by the variation of the total energy around the ground state configuration in the form of higher-order derivatives, and so their calculation using the framework of DFT is of particular interest. We can also compare these

simulations with the result of experimental methods that probe the response of a material to a range of different stimuli, obtaining information like vibrational spectra, dielectric functions, magnetic excitations and many others.

In the case of muons in a material, at least in this thesis, we are most interested in a method of investigating the vibrations of a system, also called its lattice dynamics (see [49] for a review). Within the limitations of the harmonic approximation, this will give us information about the movement of the muon in the system, like its zero-point motion and its degree of entanglement with other atoms, providing a first look at quantum muon effects (see **Section 1.3.1**).

Using $a = 1, \dots, N$ to label the different atoms in the unit cell and $\alpha = x, y, z$ for the three spatial dimensions, we can define $\mathbf{u}_{a\alpha} = \mathbf{x}_{a\alpha} - \mathbf{R}_{a\alpha}$ as the displacement from the equilibrium positions. Using a Taylor expansion the total energy of the system up to second order [50] we then have

$$E = E_0 + \underbrace{\sum_{a\alpha} \frac{\partial E}{\partial \mathbf{u}_{a\alpha}}}_{0} + \frac{1}{2} \underbrace{\left(\sum_{aa'\alpha\alpha'} \frac{\partial E}{\partial \mathbf{u}_{a\alpha} \partial \mathbf{u}_{a'\alpha'}} \right)}_{\Phi^{aa'}_{\alpha\alpha'}}, \tag{1.52}$$

where the quantity of interest is the force constants matrix $\Phi^{aa'}_{\alpha\alpha'}$. Assuming Born-von Karman boundary conditions we can substitute a plane-wave solution of the form

$$\mathbf{u}_{a\alpha} = \sum_{i\mathbf{q}} \mathbf{V}_{ia\alpha\mathbf{q}} \exp[i(\mathbf{q} \cdot \mathbf{R}_{a\alpha}) - \omega_i t] \tag{1.53}$$

to obtain an eigenvalue equation

$$D^{aa}_{\alpha\alpha'}(\mathbf{q})\, \mathbf{V}_{ia\alpha\mathbf{q}} = \omega^2_{i\mathbf{q}} \mathbf{V}_{ia\alpha\mathbf{q}}\,. \tag{1.54}$$

We have also defined the dynamical matrix as

$$D^{aa'}_{\alpha\alpha'}(\mathbf{q}) = \frac{1}{\sqrt{M_a M_{a'}}} \left(\sum_b \Phi^{aa'}_{\alpha\alpha'} \exp[-i(\mathbf{q} \cdot \mathbf{R}_b)] \right), \tag{1.55}$$

where the sum is over all periodic images of the unit cell with vectors $\mathbf{R}_b$ and $\Phi^{aa'}_{\alpha\alpha'}$ is the Fourier transform of the force constant matrix. Some of the most common *ab initio* methods of calculating phonons using DFT are:

- Frozen phonons: The simplest and most direct approach, where the necessary derivatives are calculated by performing energy calculations with displaced atomic positions. Unfortunately the displacement direction must be guessed, so the method is not very general (useful for small symmetric systems). Another limitation is that this method only works with $\mathbf{q} = 0$.

- Finite displacement: A systematic alternative to the frozen phonon approach where every ion is displaced in 3D to compute the dynamical matrix, but the method has the same limitation on the $\mathbf{q}$ vector.

- Supercell method: An extension to the previous methods where a supercell of the system is used to produce results for $\mathbf{q} \neq 0$ at the cost of more expensive calculations. The performance of this method can be greatly improved by using Fourier interpolation to limit the number of $\mathbf{q}$-points requiring a full calculation.

- Linear response: The most efficient method, using density functional perturbation theory (DFPT) to directly compute the linear change in the wavefunction with atomic displacements at any $\mathbf{q}$. Unfortunately, the additional terms that need to be calculated when using this method with an ultrasoft pseudopotential negates any advantage that they give over a simpler norm-conserving pseudopotential (see **Section 1.2.4.4**), and so CASTEP only implements the latter [51].

In general, unless only a small number of modes for a small system are desired, the linear response method of calculating the muon is preferred, at least when using CASTEP.

1.2.5.3 Transition state search

A common method of understanding the possible transitions between muon sites is to consider it as a chemical reaction where the atoms move between the two configurations. We can then model the problem as one-dimensional by defining a reaction path $\mathbf{R}(\eta)$ for the atomic positions along the reaction coordinate η, to give a potential $V(\eta)$ between the initial and final structures. We are then most interested in the transition state, defined as the highest energy configuration along the reaction path, which will determine the

probability of a given reaction happening [52]. The most useful transition state search (TSS) methods to determine this state implemented in CASTEP are:

- Linear Synchronous Transit (LST): The maximum is bracketed by performing a series of single-point energy calculations with a linearly interpolated reaction path.
- Quadratic Synchronous Transit (QST): Alternates between quadratic interpolation between the endpoints and an intermediate state to find the maximum and constrained minimisation to improve this intermediate state, producing a more accurate transition state.
- Nudged Elastic Bands (NEB): The transition is discretised into individual frames between the two endpoints by interpolation, which are then connected to adjacent frames by a quadratic constraint (to reduce the effect of local minima, hence the name *elastic band*) and nudged towards the minimal energy path by optimisation. The resulting method is more expensive, but each frame calculation can be performed in parallel and the resulting reaction path is much better [53].

1.3 Introduction to MuFinder

The MuFinder program [54] is a set of routines implemented in the Python programming language to simplify the process of performing DFT+μ muon site calculations. A graphical user interface (GUI) is also included, allowing a user to perform and analyse the results of calculations without writing any code. It was initially developed by Ben Huddart as part of his PhD Thesis [20] and I have improved its performance and extended its functionality as part of my thesis work (see **Section 1.3.1**).

The current implementation of MuFinder performs the geometry optimisation calculations using the CASTEP program [8], but we have been considering the best way of allowing users to use other codes instead. In the structural relaxation of the atomic positions, the muon is represented by a classical hydrogen atom with an artificially reduced mass. The algorithm used to generate the initial muon site positions is based on the one described by Liborio, Sturniolo *et al.* [55]:

1. Random initial positions are sampled uniformly from the unit cell.

2. A site is accepted if all its symmetry equivalent positions are:

   – At least a distance r_μ from all other sites.

   – At least a distance r_a from all atoms.

3. Repeat until the required number of sites has been generated or a certain fraction of the cell volume has been covered.

Once the geometry optimisation calculations converge, the MuFinder program includes code to cluster similar sites into groups by computing a distance matrix (accounting for the periodicity and symmetry of the system) and then employing the connected components graph algorithm [56]. Another useful part of the program is the ability to calculate the dipole magnetic field (see **Section 1.1.3**) at each of the candidate site using the MuESR library [57]. To account for the distortion that the muon causes in the unit cell we also take advantage of the fact that the fields combine linearly, so that

$$\mathbf{B}_{\text{dip}} = \mathbf{B}^{\text{undist}}_{\text{super}} + \mathbf{B}^{\text{dist}}_{\text{single}} - \mathbf{B}^{\text{undist}}_{\text{single}}, \tag{1.56}$$

where $\mathbf{B}^{\text{undist}}_{\text{super}}$ is the field at the site due to the undistorted supercell, $\mathbf{B}^{\text{dist}}_{\text{single}}$ is the field due to a single distorted unit cell and $\mathbf{B}^{\text{undist}}_{\text{single}}$ is the same but for an undistorted cell.

1.3.1 Phonon quantum methods

With the aim of providing MuFinder users with a simple method of determining if a muon at their calculated sites might be subject to quantum effects, I extended the program with the ability to parse the output of DFT phonon calculations from CASTEP and use the result to calculate a series of useful metrics for the behaviour of the muon, mostly based on suggestions from Matjaž Gomilšek.

1.3.1.1 Zero-point energy

We start by estimating the muon zero-point energy, meaning that minimum energy that the muon can have in its potential well approximated as a harmonic oscillator. After

performing a DFT+μ calculation, we run a set of phonon calculations with the muon in each of the optimised sites (see **Section 1.2.5.2**). If we are interested only in the muon motion the calculations can be performed only for $\mathbf{q} = 0$ because as a localised defect it will have no $\mathbf{q}$-space dispersion. In the common case where the muon position is not entangled with those of nearby nuclei, we find that the light muon mass means that there will be three high frequency modes which describe only its motion [58]. The zero-point energy can then be approximated by summing over the frequencies of those modes

$$E_{\mathrm{ZPE}} = \sum_{i=3}^{3} \frac{\hbar\omega_i}{2} . \tag{1.57}$$

1.3.1.2 Entanglement from normal modes

We can confirm the assumption of low entanglement between the muon and nearby atoms by calculating the entanglement witness $w_1(a, \mathbf{q})$ [59], which we define by projecting the phonon normal modes onto the muon motion and summing over the squared norms of the three most active. Since we expect that when the muon modes don't mix with the rest of the nuclei this will add up to 3, we have that

$$w_1(a, \mathbf{q}) = -\left(3 - \sum_{i=1}^{3} \sum_{\alpha} \left|V_{\mathbf{q}a}^{i\alpha}\right|^2\right)^{1/2} , \tag{1.58}$$

where $V_{\mathbf{q}a}^{i\alpha}$ are the phonon eigenvectors for a given atom a and point $\mathbf{q}$, whilst $\alpha = x, y, z$ and i ranges over the phonon modes as defined in **Equation 1.54**. Since we have $w_1 \in [-\sqrt{3}, 0]$, this means that a value close to $w_1 = 0$ will indicate a system where the muon motion is independent from the crystal lattice.

1.3.1.3 Entanglement from covariance

We can also explicitly calculate the covariance between the displacement of different nuclei in the harmonic approximation [60]. Let the elementary displacement vectors at finite temperature T be

$$\tilde{V}_{\mathbf{q}a}^{i\alpha} = V_{\mathbf{q}a}^{i\alpha} \exp[i(\mathbf{q} \cdot \mathbf{R}_a)] \sqrt{\frac{\hbar}{2m_a\omega_{\mathbf{q}i}}} \sqrt{\coth\left(\frac{\hbar\omega_{\mathbf{q}i}}{2k_B T}\right)} , \tag{1.59}$$

so that the correlation matrix between atoms a and b is given by

$$C_{ab}^{\alpha\beta} = \sum_{\mathbf{q}l} w_{\mathbf{q}} \tilde{V}_{\mathbf{q}a}^{l\alpha} \tilde{V}_{\mathbf{q}b}^{l\beta}, \tag{1.60}$$

where $w_{\mathbf{q}}$ is the weight of each point when integrating over $\mathbf{q}$-space (i.e. $\sum w_{\mathbf{q}} = 1$).

A second entanglement witness w_2 related to the Pearson correlation coefficient between the nuclear positions can then be defined as

$$w_2(a,b) = -\left| \frac{\mathrm{Tr}(C_{ab})}{\sqrt{\mathrm{Tr}(C_{aa}C_{bb})}} \right|, \tag{1.61}$$

where $w_2 \in [-1, 0]$ and as with w_1 a value of $w_2 = 0$ indicates that the motions of the two atoms are independent.

Chapter 2

Magnetism in a spin 1/2 honeycomb coordination polymer antiferromagnet

In recent years there has been great interest in engineering materials with desirable magnetic properties through careful selection of their components. An example of this is the apparently simple honeycomb lattice, a hexagonal structure with a two-atom basis, which can exhibit complex states of matter like the massless Dirac fermions in graphene or the topological quantum spin liquid (QSL) phase proposed by the Kitaev model [61–64]. The latter is an elusive state of matter where strong quantum fluctuations prevent magnetic order down to the lowest temperatures and give rise to unusual excitations, with possible application in topological quantum computing and understanding unconventional superconductivity. This has brought great interest to magnetic systems which adopt this structure but have enough flexibility that subtle structural changes can be used to tune the strength of the interactions. A promising avenue of research is molecular magnets like the novel antiferromagnetic coordination-polymer-based $S = 1/2$ honeycomb lattice $Cu(pym)_{1.5}(H_2O)(BF_4)_2$ (pym = pyrimidine), which will be abbreviated as CHC and will be the focus of our investigation. As a first step in tuning its properties, we use muons to determine its low-temperature behaviour and ground state.

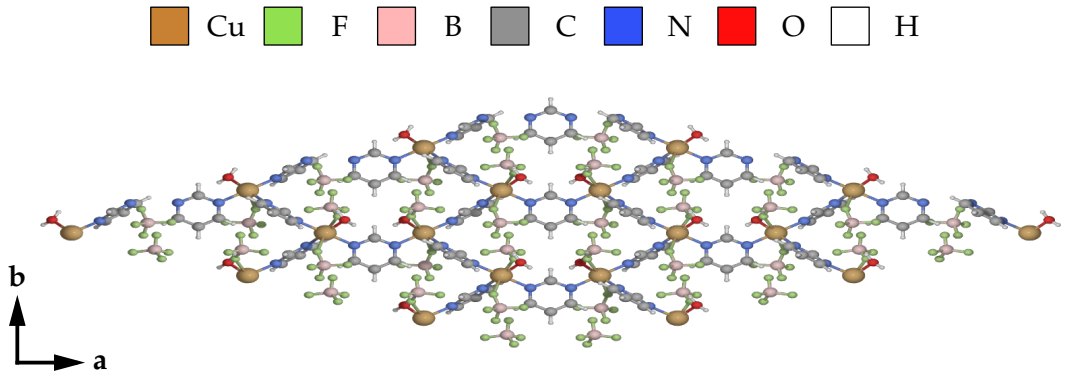

Figure 2.1 Atomic structure of honeycomb compound $Cu(pym)_{1.5}(H_2O)(BF_4)_2$.

In the CHC material, as shown in **Figure 2.1**, we find that each copper atom is connected to another three by a bridging pyrimidine ligand. This produces a nearly perfect honeycomb lattice with one of the neighbouring copper atoms being slightly closer at 4.8 Å than the other two at 5.9 Å. The honeycomb layers are also well separated from each other, giving rise to the highly two-dimensional structure. We also find that the $\mathrm{Cu-pym-Cu}$ interactions are all antiferromagnetic and expected to be relatively large, suggesting that this might be a first step towards a molecule-based Kitaev lattice [65]. In this analytically solvable model we have an infinite set of $S = 1/2$ particles arranged into a honeycomb lattice interacting through a Hamiltonian of the form

$$H = -J_x\left(\sum_{\langle ij\rangle_x}\sigma_i^x\sigma_j^x\right) - J_y\left(\sum_{\langle ij\rangle_y}\sigma_i^y\sigma_j^y\right) - J_z\left(\sum_{\langle ij\rangle_z}\sigma_i^z\sigma_j^z\right), \tag{2.1}$$

where the sums $\langle ij\rangle_\alpha$ for $\alpha = x, y, z$ are taken over the three different directions of links between atoms in the lattice. This model provides a surprisingly rich variety of different phases depending on the relative strength of the interactions J_α, including a spin-liquid ground state [66]. Although the CHC material under investigation is not thought to be a Kitaev lattice, understanding the effect of the honeycomb lattice on its properties and making use of the precise control of the interactions allowed by the molecular structure will bring us closer to understanding QSLs and other exotic states of matter.

Since magnetic susceptibility measurements of the material show no evidence of the long-range order expected in an AFM system down to 2 K, the main aim of this investigation will be to understand the ground state of the CHC system. This will require a combination of different techniques, with μ^+SR being an important part due to its sensitivity to long-range order in the small magnetic moments involved.

The work in this chapter is based on data analysis performed by myself at the University of Durham using measurements taken by myself, Tom Lancaster and collaborators at the ISIS Neutron and Muon Source. The measured sample was prepared by Jamie Manson at Eastern Washington University.

2.1 Experimental ZF μ^+SR measurements

A series of μ^+SR measurements were performed on a polycrystalline sample of CHC material at different temperatures and applied fields using the EMU spectrometer at the

ISIS Neutron and Muon Source which is part of the Rutherford Appleton Laboratory. An example of the measured ZF spectra can be found in **Figure 2.2**, where we see clear evidence of a phase transition with a sharp change in the oscillation and relaxation of the asymmetry with temperature.

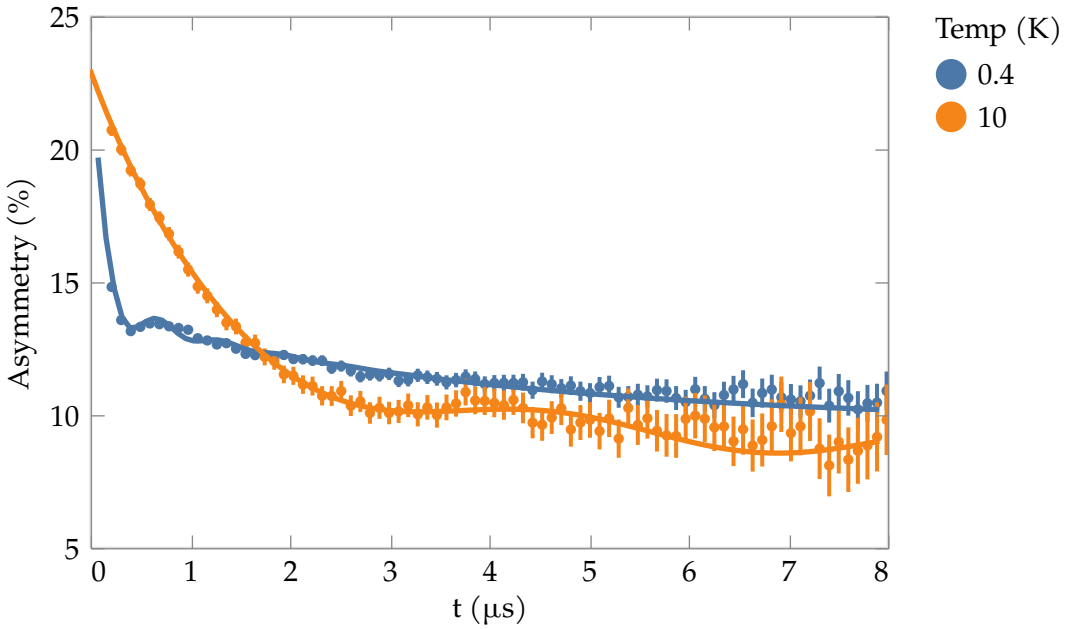

Figure 2.2 Example ZF spectra below the transition temperature fitted to a Bessel function (blue) and above the transition fitted to a F − μ model (orange).

2.1.1 Low-temperature measurements

The sample was first cooled to $T = 0.3\,\mathrm{K}$ and a series of zero-field measurements were made at increasing temperatures. At low temperatures, we see a fast oscillation which after the first period is well approximated by a damped cosine function with a $-45°$ phase shift. This is characteristic of incommensurate long-range magnetic order with a field distribution varying sinusoidally in space (see **Section 1.1.4.1**) and is more accurately described by a Bessel function of the first kind $J_0(\omega_B t)$. As the temperature increases the frequency of the oscillation decreases whilst the relaxation rate increases and we approach the phase transition. The resulting asymmetry spectra were fitted to the function

$$A(t) = A_B \exp(-\lambda_B t)\, J_0(\omega_B t) + A_L \exp(-\lambda_L t) + A_l \exp(-\lambda_l t) + A_b\,. \tag{2.2}$$

In addition to the oscillation, we also have two Lorentzian exponential relaxation terms with amplitudes A_L and A_l which suggest two different muon sites and give a fast and

a slow relaxation respectively, which is typical in this type of molecular antiferromagnet [1]. After fixing the values of $A_B = 2.6\%$, $A_L = 6\%$ and $A_l = 4.3\%$ and globally fitting $A_b = 9.69 \pm 0.02\%$, $\lambda_B = 1.32 \pm 0.04\,\mu s^{-1}$ and $\lambda_L = 7.31 \pm 0.12\,\mu s^{-1}$ across all spectra, the temperature dependence of the remaining model parameters can be found in **Figure 2.3**, where we notice that we have an anomaly at $T_A = 0.45\,K$ in the temperature-dependent parameters ω_B and λ_l.

We analyse the transition by identifying the Bessel function frequency ω_B, which is related to the magnetic field B_0 at the muon sites by $\omega_B = \gamma_\mu B_0$, as an effective order parameter and fitting it to a phenomenological model

$$\omega_B = \omega_0 \left[1 - \left(\frac{T}{T_N} \right)^\alpha \right]^\beta , \tag{2.3}$$

which allows us to extract the transition parameters. This gives a transition temperature of $T_N = 4.02 \pm 0.01\,K$ whilst the exponents are $\alpha = 1.44 \pm 0.14$ and $\beta = 0.44 \pm 0.02$. The value of the β exponent is unusual, being larger than expected from common theoretical models for magnetic systems (for example, a 3D Heisenberg model [67] has $\beta \simeq 0.366$). The model seems to accurately capture the behaviour of the phase parameter close to the transition, giving a reasonable value for the transition temperature, and even fixing $\alpha = 1$ and fitting close to the transition gives a similar value of β. This is closest to the mean field result of $\beta = 1/2$, which is observed primarily in materials with long-range interactions like superconductors, and so although the fluctuations are most likely 3D further research is required.

As mentioned previously, the possible anomaly in the Bessel function frequency below 1 K with a characteristic feature around $T_A = 0.45\,K$ is of interest, being unusual for this class of materials. We also note that the amplitude of A_l decreases sharply below T_A, indicating that fewer muon sites contribute to this part of the signal. The cause of this anomaly is not clear, although it is possibly a magnetic transition caused by an incomplete ordering at the higher T_N from magnetic frustration [68], or is perhaps due to the influence of magnetic impurities or disorder in the material (e.g. stacking faults, etc) [69]. Interestingly, this anomaly might be related to the unusual results of SQUID magnetometry measurements in the material, which is found to deviate from the expected Curie-like behaviour with a shoulder at $T = 7\,K$. A slight inflection around 4 K might correspond

to the transition but the susceptibility keeps increasing at lower temperatures suggesting paramagnetic behaviour, perhaps from impurities. We expect that these impurities arise from intrinsic disorder in the system as observed in some molecular superconductors [70, 71], and not from extrinsic imperfections caused by contamination during synthesis or radiation damage.

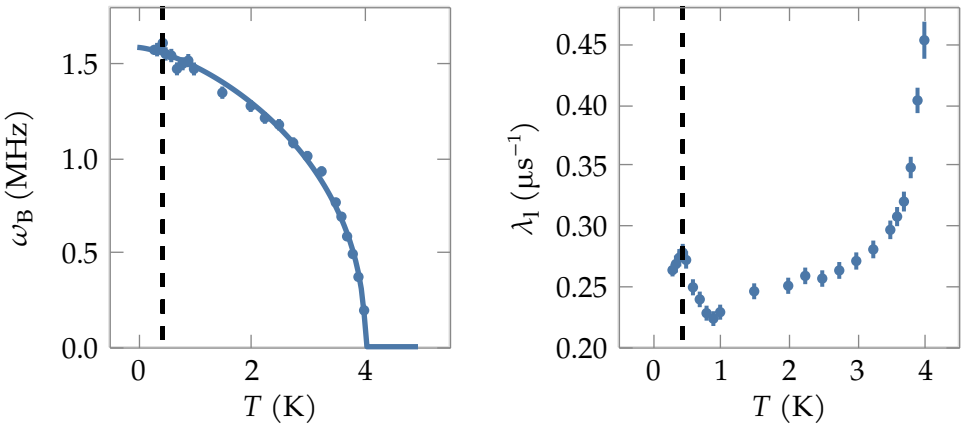

Figure 2.3 Dependence of asymmetry fitting parameters with temperature below the phase transition, including the curve in ω_B used to fit T_N and a dashed line indicating T_A.

2.1.2 High-temperature measurements

Additionally, μ^+SR ZF measurements were also taken at temperatures above the magnetic transition where the low-frequency oscillations in the asymmetry no longer match a Bessel function but were identified as similar to those seen in fluorine-containing materials and so were fitted to a so-called $F-\mu$ signal [25], which arises from the dipole-dipole interactions between a fluorine nuclei and the muon spin (see **Section 1.1.4.3**). The asymmetry can then be fitted to a combination of this characteristic combination of cosines and two Lorentzian exponential relaxation terms

$$A(t) = A_b \exp(-\lambda_b t) + A_L \exp(-\lambda_L t) + A_F \exp(-\lambda_F t) \times \frac{1}{6}\left[1 + 2\cos\left(\frac{\omega_F t}{2}\right) + \cos(\omega_F t)\right], \tag{2.4}$$

where we can estimate the separation between the fluorine atom and the muon from the calculated frequency using the fact that $\hbar\omega_F = (\mu_0\hbar^2\gamma_\mu\gamma_F)/\left[4\pi(d_F)^3\right]$. After fixing the values of $A_F = 2\%$ and $\lambda_F = 0\,\mu s^{-1}$ and globally fitting $A_b = 10.12 \pm 0.11\%$, $\lambda_b =$

$0.014 \pm 0.002\,\mu s^{-1}$ and $A_L = 10.85 \pm 0.09\%$, the temperature dependence of the remaining model parameters can be found in **Figure 2.4**.

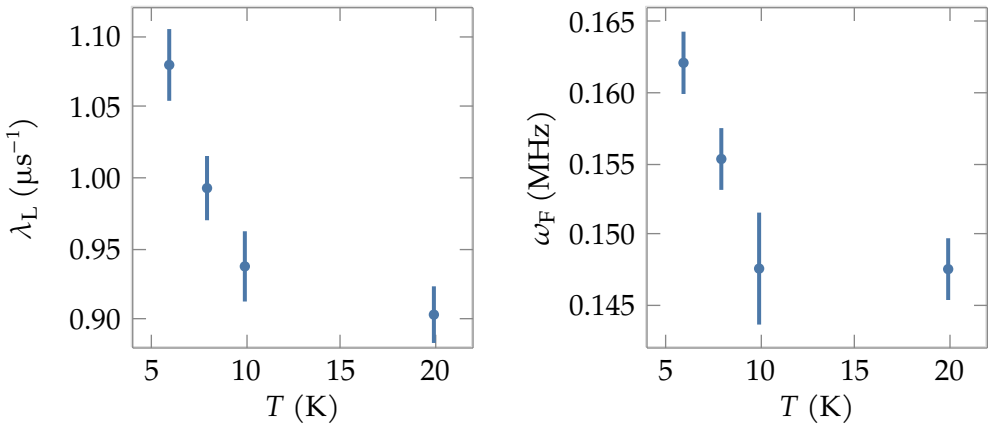

Figure 2.4 Dependence of the asymmetry fitting parameters with a temperature above the phase transition.

Using the frequencies ω_F fitted from the asymmetry spectra the average muon-fluorine distance was estimated to be $d_F = 1.33\,\text{Å}$. We also performed a series of DFT+μ site calculations (as described in **Section 1.3**) and found that all the low-energy sites have the muon close to an oxygen atom (1.02 Å). These sites were, however, still close enough to a fluorine atom (with a distance of 1.51 Å) to possibly explain the experimental results. The fact that we also have a group of three other fluorine atoms slightly further away from the muon might also be responsible for giving a higher frequency (and so a smaller distance) than suggested by the DFT calculations, since the asymmetry might be better described by a more complex function involving all nearby fluorine atoms instead of the basic $F-\mu$ used. In the future, it might be possible to construct an accurate model of the asymmetry above the transition by combining the structural information obtained from the DFT simulations with a density matrix calculation of the polarisation [26] as described in **Section 1.1.4.3**.

2.2 Conclusions

Our aim with this investigation was to probe the low-temperature behaviour and ground state of the novel CHC compound, a molecular antiferromagnet with a honeycomb lattice structure. By using a series of zero-field μ^+SR measurements we find that the material undergoes a phase transition at $T_N = 4.02 \pm 0.01\,\text{K}$ into an ordered magnetic state which

was found to be incommensurate, an unusual feature in a molecular magnet. We also find that above the transition the system becomes disordered and the interaction between the muon and nearby fluorine atoms (as confirmed by DFT muon site calculation) dominates. The hope is that by taking advantage of the fact that the material is a coordination polymer we can more easily tune the structure and interactions to study the effect on the magnetism and better understand this class of materials.

Chapter 3

Muon-spin relaxation investigation of magnetic bistability in a crystalline organic radical compound

---

Understanding the link between hysteresis and structure is an important theme in materials design, since systems that exhibit hysteretic effects intrinsically possess memory and are therefore of potential technological interest [72]. Recently, the crystalline organic radical compound 4-(2-benzimidazolyl)-1,2,3,5-dithiadiazolyl (HbimDTDA) was reported [73] to exhibit bistability in its magnetic and structural properties near room temperature. In the solid state, the neutral radical crystallises into the orthorhombic *Pbca* space group (see **Figure 3.1**). The magnetic switching effect follows from a subtle single-crystal-to-single-crystal structural phase transition that occurs without symmetry breaking, but involves a significant reorganisation of the molecules. Structural analysis at $T = 100\,\mathrm{K}$ shows that the low-temperature structure of the material involves one-dimensional linear arrays of HbimDTDA molecules, with each molecule forming part of a pancake-bonded pair with a partner molecule on a neighbouring array **Figure 3.1a**. The geometry of the pancake bonds, determined by overlap of the four lobes of each molecule's singly-occupied molecular orbital, orients the molecules to create a dense 3D network of supramolecular contacts. In contrast, the high-temperature structure of the system determined at $T = 340\,\mathrm{K}$ does not feature the pancake bonds, which are broken and replaced with new electrostatic contacts **Figure 3.1b**. These two structural phases are related by a translation in the [010] direction, such that the one-dimensional supramolecular structures (defined by hydrogen bonding between neighbouring molecules) shift with respect to one another. Analysis of the temperature dependence of the structural phase transition confirms a first-order transition between two unique phases, occurring around $T \approx 270\,\mathrm{K}$, with significant thermal hysteresis [73].

Each radical unit carries a $S = 1/2$ spin and the magnetism of the system is closely linked to the structural transition. Magnetic susceptibility data were reported to indi-

cate diamagnetic low-temperature behaviour, which was explained in terms of electronic overlaps promoted by the pancake bonds between π-radicals [73]. At high temperature the susceptibility increases dramatically, consistent with the non-pancake bonded phase being paramagnetic and comprising an unpaired $S = 1/2$ spin per molecule, with some degree of antiferromagnetic coupling between them.

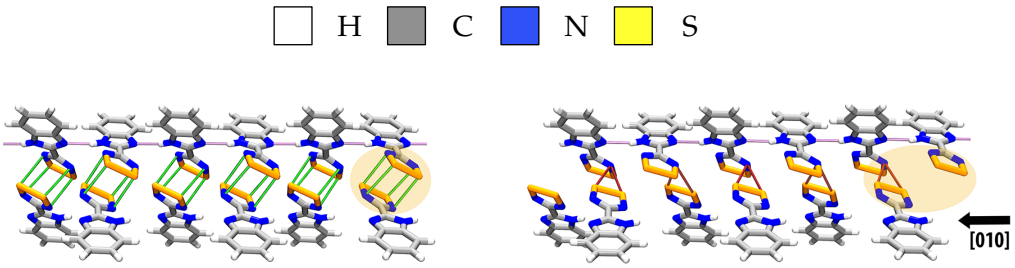

(a) 100 K (b) 340 K

Figure 3.1 (a) Low-temperature structure of HbimDTDA, with pancake bonds between the linear arrays of molecules arranged along [010]. (b) High-temperature structure following a shift along [010] that breaks the pancake bonds.

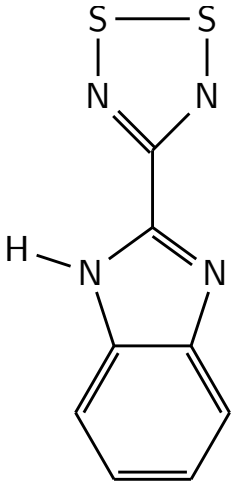

Figure 3.2 Chemical structure diagram of single HbimDTDA molecule.

Implanted muons are widely used as local probes of magnetism [12], with their extreme sensitivity motivating their use to determine the magnetic order and dynamics in low-moment, molecule-based magnets. Muons have been used rather less to look at magnetic bistability, though they have proved an effective probe of molecular spin-crossover (SCO) materials formed from bistable molecules that are able to switch from low to high spin states via a cooperative phase transformation [74]. In this chapter, we report the use of

muon-spin relaxation (μ^+SR) techniques to examine the cooperative magnetic switching in HbimDTDA from a local perspective. We show that muons are sensitive to the bistability of the magnetic state and use this to elucidate the nature of the low- and high-temperature regimes, and provide a determination of the characteristic field fluctuation rate in the low-temperature regime. We also determine the muon sites using first-principles electronic structure methods to demonstrate how the muon is sensitive to the magnetic environment in this chemically-complex material.

The work in this chapter is based on data analysis and DFT muon site calculations performed by myself at the University of Durham using measurements taken by Tom Lancaster and collaborators at the ISIS Neutron and Muon Source. Help in understanding the results and performing the simulations was given by Francis Pratt and Kathryn Preuss.

3.1 Experimental μ^+SR measurements

To investigate the hysteresis effect and the magnetism of the two phases of the compound, μ^+SR measurements were performed using the HiFi spectrometer at the STFC-ISIS Facility (Rutherford Appleton Laboratory, UK). We employed the longitudinal field (LF) geometry where an external magnetic field is applied along the initial muon-spin direction. Initially, a series of measurements were made in zero applied magnetic field, sweeping temperatures such that each measurement was made at a fixed temperature for 35 min, with temperature changes taking 7 min. Measurements were also made as a function of applied field at fixed temperature, for 40 min per point. We also performed weak transverse field (wTF) measurements, where a small magnetic field (2 mT) is applied perpendicular to the initial muon-spin direction. Each measurement took 24 min, with 7 min for temperature adjustment. A polycrystalline sample of HbimDTDA was prepared as described previously [73]. For the measurement it was wrapped in Ag foil, sealed in an airtight Cu holder and then loaded into a ^{4}He cryostat.

3.1.1 Zero-field measurements

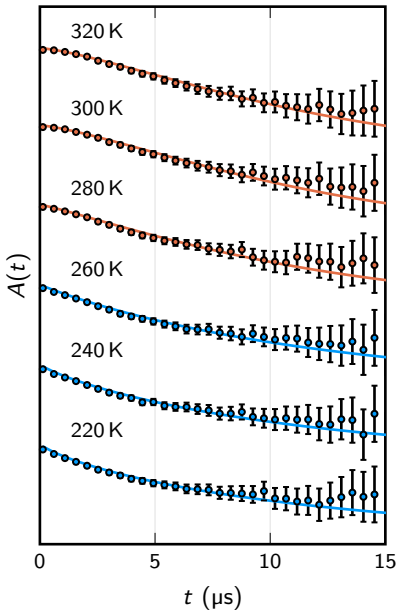

Figure 3.3 ZF asymmetry spectra measured on HbimDTDA at increasing temperatures across the transition, offset for clarity and in arbitrary units.

The sample was first cooled to $T = 220\,\mathrm{K}$ and a series of measurements in zero-applied field (ZF) were made in increments of 10 K up to 350 K. Measurements were then repeated for decreasing temperature. Example spectra for measurements taken on increasing temperature are shown in **Figure 3.3**. The observed trend is that spectra resemble an exponential relaxation at low temperatures and become more Gaussian in character as the temperature increases. To track their evolution, the spectra were fitted to a stretched exponential relaxation function

$$A(t) = A_{\mathrm{R}}^{\mathrm{ZF}} \exp\left[-\left(\lambda^{\mathrm{ZF}} t\right)^{\beta}\right] + A_{\mathrm{B}}^{\mathrm{ZF}}, \tag{3.1}$$

where the final term $A_{\mathrm{B}}^{\mathrm{ZF}}$ accounts for muon spins that do not relax, including those from muons implanted in the sample holder. To simplify the fitting procedure we fix the parameters which vary the least in a free fit, in this case $A_{\mathrm{B}}^{\mathrm{ZF}} = 12\%$ and $\lambda^{\mathrm{ZF}} = 0.08\,\mu\mathrm{s}^{-1}$ by taking an average. We also find that the relaxing asymmetry $A_{\mathrm{R}}^{\mathrm{ZF}}$ increases from 15.1% to 16.9% between the low- and high-temperature phases. The parameter β allows us to interpolate between an (i) approximately exponential decay, which results from a combination of dynamically fluctuating, disordered magnetic moments in the fast fluctuation

limit; and (ii) behaviour approaching Gaussian decay, which approximates the initial relaxation of the Kubo-Toyabe function caused by static magnetic moments sampled from a normal distribution [12].

The results of the fitting procedure are shown in **Figure 3.4**, where the fitted stretching parameter is seen to change as a function of temperature across a transition region **Figure 3.4a**. We can clearly see the hysteresis effect with the decreasing-temperature measurements (down triangles) consistently at higher values than the increasing-temperature ones (up triangles) over a region centred on $T = 274 \pm 11\,\mathrm{K}$. This was extracted from the values of β by fitting both sets of measurements to the phenomenological functional form

$$A_{\mathrm{R}}^{\mathrm{wTF}}(T) = A_{\mathrm{H}} \tanh[k_{\mathrm{H}}(T - T_0)] + c_{\mathrm{H}}\,, \tag{3.2}$$

where A_{H}, k_{H} and c_{H} are parameters which determine the shape and position of each curve and are kept constant between them whilst T_0 determines the centre and is different between the increasing and decreasing temperature curves. We can therefore determine an approximate value for the width of transition by taking the difference between the T_0 values. This value for the centre of the hysteresis loop also agrees with the values of $T \approx 270\,\mathrm{K}$ and $\Delta T \approx 9\,\mathrm{K}$ calculated from magnetic susceptibility and confirmed by X-ray powder diffraction measurements reported in Ref [73].

The difference between the two regimes can be explained by the different distributions of fluctuating magnetic moments in each. In the low-temperature phase we have randomly oriented electronic moments (in a distribution of width $\Delta/\gamma_\mu = \sqrt{\langle B^2 \rangle}$, where $\gamma_\mu = 2\pi \times 135.5\,\mathrm{MHz/T}$ is the muon gyromagnetic ratio) fluctuating at rate ν in the fast fluctuation limit $\nu \gg \Delta$. As the temperature increases through the transition, the density of moments increases due to the structural transition. Crucially, these moments fluctuate at a much faster rate in the higher temperature phase, with the result that the muon spin, whose evolution is limited by the value of its gyromagnetic ratio, cannot complete a rotation before the local field fluctuates and changes value [12]. The electronic moments are therefore motionally narrowed from the spectra in the high-T regime. This leaves only the random nuclear moments to account for a large part of the relaxation. The nuclear spins are quasistatic and so are described by a Kubo-Toyabe-like function (of which we only

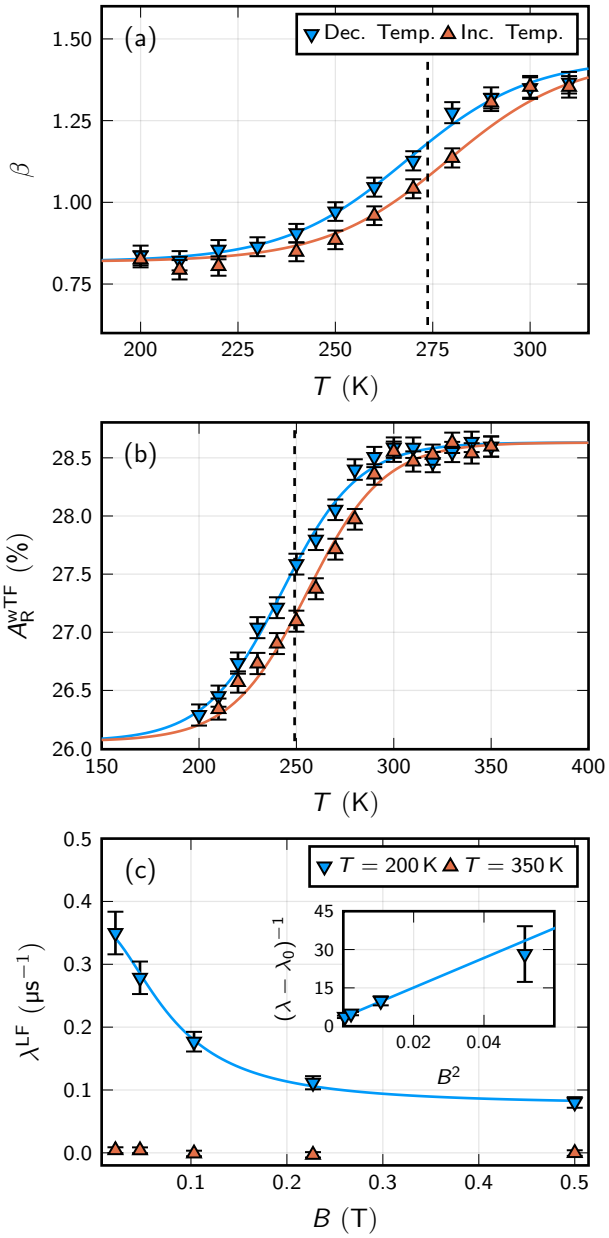

Figure 3.4 (a) The result of fitting a stretched exponential function (**Equation 3.1**) to the ZF results, showing the temperature dependence of the line-shape parameter β for increasing (Inc.) and decreasing (Dec.) temperature.(b) The result of fitting an exponentially decaying cosine curve (**Equation 3.3**) to the wTF results, for which we show the relaxing asymmetry A_R^{wTF}.(c) The result of fitting an exponential decay (**Equation 3.4**) to the field-dependent LF data, giving the relaxation parameter λ^{LF} fitted to the Redfield formula (**Equation 3.5**).

observe the early-time, Gaussian part). The fact that the value of β appears to plateau

below $\beta \approx 1.5$ suggests that the motional narrowing is not complete.

3.1.2 Weak transverse-field measurements

In order to confirm the existence of the hysteresis loop, the temperature-dependent measurements were also repeated over the same range but in a weak transverse magnetic field ($B = 2\,\mathrm{mT}$). Since the external field is so low, the only muon spins that will oscillate are those in sites where the local field almost vanishes in zero field, and which are not rapidly relaxed by dynamics. The size of the change we observe in amplitude with temperature is small, suggesting that those muons contributing to this effect constitute only a small fraction of the total ensemble, which might be explained by the change in the nature of the muon sites with structural phase, as discussed below. The results were fitted to a decaying cosinusoidal curve

$$A(t) = A_{\mathrm{R}}^{\mathrm{wTF}} \exp\left(-\lambda^{\mathrm{wTF}} t\right) \cos(\omega t + \phi) + A_{\mathrm{B}}^{\mathrm{wTF}}, \tag{3.3}$$

with the resulting relaxation asymmetry shown in **Figure 3.4b**. We again see a consistent separation between the measurements made in increasing and decreasing temperature over the transition region, but compared to those above, the fitted parameters have a much lower uncertainty (in part because fitting a periodic cosine wave has less margin of error than an exponential), and so the hysteresis loop is clearer. Repeating the fitting procedure used in the previous section, we find that the loop for these measurements is centred on the slightly lower temperature of $T = 249 \pm 13\,\mathrm{K}$. The discrepancy between this and the transition derived from the change in the β parameter suggests the two measurements are sensitive to different aspects of the muon's interaction with the system: β reflects the distribution of local magnetic fields; $A_{\mathrm{R}}^{\mathrm{wTF}}$ reflects the availability of muon sites in the two regimes, as described below. We note also that for both sets of measurements the transition appears to be continuous, although the resolution is not sufficient to rule out steps on the scale of $\approx 10\,\mathrm{K}$.

3.1.3 Longitudinal-field measurements

To elucidate the dynamic response, a series of LF measurements were performed at both $T = 200\,\mathrm{K}$ and $T = 350\,\mathrm{K}$ by applying a series of external magnetic fields (up to $B = 0.5\,\mathrm{T}$)

along the direction of the muon spin. As the field magnitude increases the Zeeman term in the muon's Hamiltonian dominates, and the muon spin is pinned along its initial direction. Time-varying local fields can then cause a muon spin-flip and relax the asymmetry. This state of affairs allows us to investigate the magnetic-moment dynamics in the two phases by fitting the results to a series of exponential functions, quantifying the relaxation due to the fluctuating magnetic fields. This is appropriate even in the high T limit, since the applied field rapidly quenches the Gaussian relaxation, leaving residual exponential relaxation reflecting electronic dynamics. The model used is therefore

$$A(t) = A_{\mathrm{R}}^{\mathrm{LF}} \exp\left(-\lambda^{\mathrm{LF}} t\right) + A_{\mathrm{B}}^{\mathrm{LF}}, \tag{3.4}$$

where we fix the parameter $A_{\mathrm{B}}^{\mathrm{LF}} = 10\%$ to simplify the fitting procedure. The value of the relaxation rate λ^{LF} is also shown in **Figure 3.4c** for both temperatures. We see that only the low-temperature measurements show a decrease with increasing magnetic field. This relationship can be fitted to the Redfield formula [12]

$$\lambda^{\mathrm{LF}} = \frac{2\Delta^2 \nu}{\left[\nu^2 + \left(\gamma_\mu\right)^2 \left(B_0\right)^2\right]} + \lambda_0, \tag{3.5}$$

where Δ is the fluctuating amplitude ($\Delta^2/\gamma_\mu^2 = \langle(\delta B)^2\rangle$), ν is the fluctuation rate (related to $\tau = \nu^{-1}$ the correlation time between changes), B_0 is the applied external field and λ_0 is an offset accounting for the component of the relaxation not reduced by the external field. (Such an offset is often observed in dynamically-fluctuating molecular systems [75]). This gives values of $\nu = 66 \pm 12\,\mathrm{MHz}$ and $\Delta = 3.1 \pm 0.3\,\mu\mathrm{s}^{-1}$ for the parameters. In the high-temperature phase a very small relaxation rate is observed in applied field, confirming that the ZF relaxation is caused by static nuclear moments, which are unable to cause the required spin flips. On the other hand, the successful description of the low-temperature relaxation parameters with the Redfield formula confirms that the muon-spin relaxation is caused by randomised electronic moments with dynamics in the fast-fluctuation limit.

3.2 Muon site analysis

The candidate muon sites for HbimDTDA were calculated using DFT geometry optimisation following the procedure described in **Section 1.3** using the CASTEP code [8] with

files generated by the MuFinder program [54], producing 30 candidate sites for each phase in a 8.6 Å × 9.9 Å × 21.4 Å unit cell of the crystal. The calculations were run with both a bare muon (Mu^+) or a muonium (Mu^0) atom by changing the number of electrons in the system. The relaxed unit cells were analysed first by considering the distortions to the atomic positions caused by the muon, which in this case are minimal between atoms of the same molecule but more considerable between molecules, with a maximum radial displacement of ≈ 1.0 Å, especially for the sites $\bar{\mathsf{H}}$ / ■ and H / ■ described below. Muon sites corresponding to different relaxed structures were compared by using the vector between the site and closest atom to position the muons in an undistorted cell. Finally, the symmetry of the crystal was used to move all the sites to the same molecule and nearby sites ($d < 1$ Å) were grouped by averaging their positions. All the bare muon site simulations were also repeated for muonium, by adding an extra electron to the system for the muon. This gave similar results, so that sites were matched with the bare muon ones by assuming that ones closer than 0.5 Å are equivalent. All sites were realised in both cases with the exception of a single muon site (denoted S_1 / ■ below) which was not found in the high-temperature phase.

The positions of the calculated candidate muon sites are shown in **Figure 3.5** (only for the case of Mu^0 but the others are similar) and their respective energies are listed in **Table 3.1**. Energies are given relative to the lowest-energy site for each column. The similarity in energy between the candidate sites in each class suggests that we might expect each of them to be realised. We first find a set of candidate sites common to both structures close to the nitrogen atoms in the sulphur-containing rings. Two of them (S_1 / ■ and S_2 / ■) are located *outside* the region between rings in adjacent chains (see the shaded area in **Figure 3.1a**), with the second being *closer* to the atoms which form the contact bond between chains in the high-temperature phase (see **Figure 3.1b**). Another site (S_3 / ■) is located *inside* the region but *away* from the contact sulphur atoms, which might explain why it has a similar energy at the lower temperature but is higher in energy at 340 K. The other low-temperature site ($\bar{\mathsf{H}}$ / ■) has the muon attached to the non-hydrogenated nitrogen atom in the central ring and is higher in energy for muonium but the lowest energy site in the case of the bare muon.

Apart from these common sites, for the 340 K structure we also find two new lower-energy sites. One (H / ■) is found sharing the nitrogen atom with a hydrogen atom in the central ring (see **Figure 3.2**) and the other (S_4 / ■) is again attached to one of the nitrogen atoms in the sulphur-containing ring, but in this case is *inside* the inter-ring region and *closer* to the contact atoms. To explain the presence of the new sites we note that the main difference between the two structural phases is the presence of the pancake bonds between the sulphur rings in the lower-temperature state and the relative position of the chain. The breaking of these bonds at higher temperatures seems to make the new positions available.

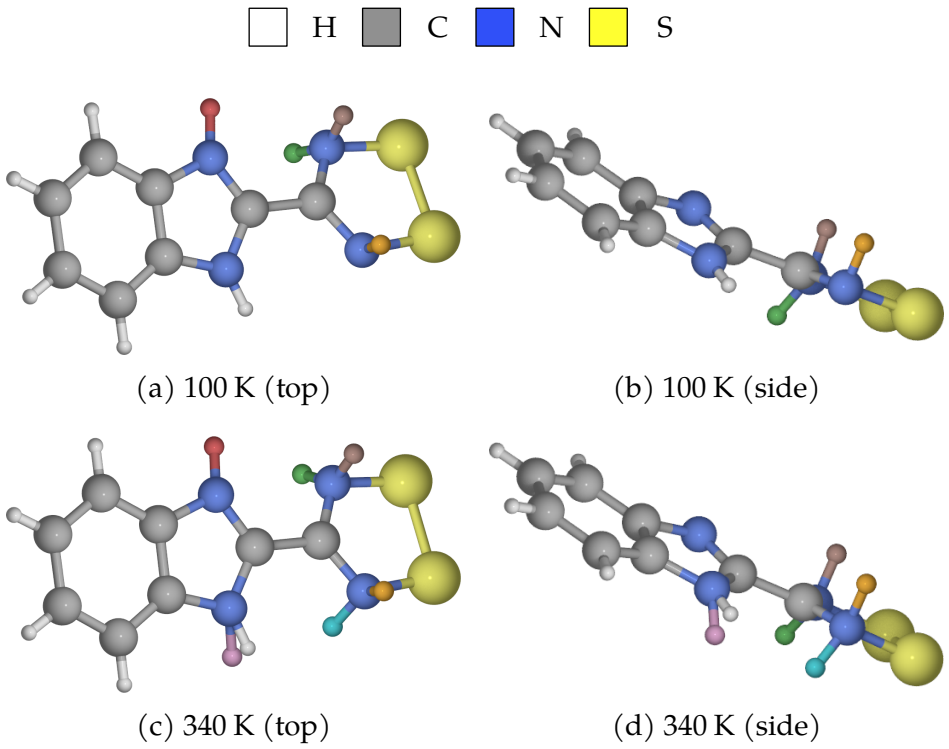

Figure 3.5 Diagrams showing the main sites for muonium at (a,b) 100 K, with three low-energy sites (■, ■ and ■) and a slightly higher-energy site (■) (c,d) 340 K, with two new lower energy sites (■ and ■).

3.3 Discussion

Conventionally we assume that a bare (or diamagnetic) muon spin couples to the local magnetic field in a material, and probes the local field distribution without causing an appreciable perturbation. The relevant muon sites from the previous section would then

Site	Energy (eV)			
	Mu^0		Mu^+	
	100 K	340 K	100 K	340 K
S_1 (■)	0.01	0.06	0.43	-
S_2 (■)	0.01	0.17	0.38	0.93
S_3 (■)	0.12	0.14	**0.00**	**0.00**
$\bar{H}$ (■)	**0.00**	0.06	0.37	0.24
H (■)	-	0.05	-	**0.00**
S_4 (■)	-	**0.00**	-	0.23

Table 3.1 Table comparing the energies of the unit cell with the muon at the different bare muon (Mu^+) and muonium (Mu^0) sites calculated using DFT, and given relative to the lowest energy found in each column.

be the bare ones. The low-temperature regime of this material, which is thought to be formed from singlet spins, was previously suggested to be diamagnetic on the basis of bulk susceptibility measurements. However, if the muon takes the form of an unperturbing, diamagnetic probe, then the low-temperature relaxation cannot simply be explained by the presence of highly-dilute magnetic impurities in a diamagnetic background, since the Redfield behaviour observed relies on the presence of a dense array of magnetic moments that rapidly fluctuate in time. It is therefore unlikely that the material is non-magnetic in this regime. We suggest that instead we have fluctuating moments of sufficient density to be approximated as giving rise to a Gaussian distribution of fields at any instant. One possibility here is the imperfect formation of the pancake bonds. This is caused by normal crystal defects and for this type of DTDA dimer it is common to observe a few percent of free Curie spins in an otherwise diamagnetic solid [76]. We distinguish the local magnetic field distribution in the low-temperature phase, featuring this distribution of moments fluctuating in the fast fluctuation limit, from that in the high-temperature regime, which likely comprises a denser distribution of moments, with a far greater characteristic fluctuation rate.

Since the muon is a local probe, the transition we observe likely reflects muons locally detecting the switching of nearby clusters of molecules in the sample. A cluster in the low-temperature state giving an exponential relaxation and one in the high-temperature state

a Gaussian one. The stretched exponential used in the intermediate regime then models the sum of contributions, whose relative size varies with temperature. We note that our results in this system resemble those measured in spin-crossover systems based on iron (II) ions which show a crossover between a low-spin ($S = 0$) state at low temperature and a high-spin ($S = 2$) state at high temperature [74]. In those materials the muon spectra were also fitted to a stretched-exponential function with $\beta < 1$ in the low temperature, low-spin configuration and β approaching $\beta = 2$ at high temperature. It was suggested that the relaxation at low temperature reflected an incomplete crossover, with some spins remaining in the high-spin configuration at low temperature and forming a very dilute distribution leading to root-exponential relaxation [77]. A similar picture could be the case here, with any regions that avoid the low-temperature structural transition giving rise to a distribution of disordered spins, causing the observed relaxation. However, the fact that we find $\beta \lesssim 1$ suggests that the density of moments in our system at low temperatures is greater than the highly-dilute one that would be expected to give rise to $\beta \approx 0.5$, which was the value observed in some of the low-temperature phases of the iron-based spin-crossover systems [78].

Another possibility which could account for our data is that the muon's sensitivity to the magnetism in the low-temperature, singlet state is caused by a perturbation the muon makes to the system, as was suggested to be the case in molecular spin-ladder materials [79]. This might involve the bare, charged muon causing a local distortion to the nearest spin singlet, or that the sensitive species is derived from muonium, whose extra electron is involved in causing the necessary distortion. The muon, along with its local distortion, would then become the sensitive species, whose interactions give rise to the observed relaxation. We note that the observed fluctuation amplitude Δ in this regime corresponds to the magnetic field from an electron spin around $\approx 8\,\text{Å}$ from a muon, providing a rough length scale for the interaction. If this is the case, then the material could adopt a fairly uniform singlet ground state with few additional intrinsic magnetic impurities. However, even in this case, the transition to a regime of large, dense magnetic moments at high temperatures would continue to allow the muon to faithfully probe the magnetic switching transition.

Finally, the difference in the low-energy muon sites in this material's two structural phases is a noteworthy feature which has not been discussed previously in materials of this type. Since we find a range of muon sites in this system with very similar energy, we would expect the muons to sample a range of internal magnetic fields. Although both a bare muon and muonium allow several different low-energy candidate sites in the two temperature regimes, owing to the range of fields probed, the two cases are unlikely to lead to significant differences in the measured spectra. However, the observation of new sites becoming available after a structural change likely applies well beyond this material.

Important questions remain about the nature of the phase transition in this system, particularly related to the broadness of the transition compared to the width of the hysteretic region. Inspection of the magnetic susceptibility data suggests the presence of steps in the response [73]. Indeed, tracking the structural component of the transition as a function of T by powder x-ray diffraction also suggests a stepwise progression, with reflections consistent with the high temperature phase appearing over a range of temperatures. There has been recent interest in the possibility of realizing the devil's staircase structure in such systems [80], where step-like transitions between the spin states have been observed.

3.4 Conclusions

Muon-spin relaxation measurements, paired with muon-site analysis, have allowed us to probe the hysteretic magnetic switching behaviour of HbimDTDA from a local perspective. We identify a hysteresis width of $\Delta T \approx 22\,\mathrm{K}$, centred on $T = 274\,\mathrm{K}$. The low-temperature state gives rise to muon-spin relaxation which is well described by a model that assumes a dense arrangement of disordered, dynamically-fluctuating moments. The structural transition causes the muon sites in the two regimes to differ. However, in a chemically-complex material such as this, a large number of sites of similar energy occur in both regimes, with the result that we expect the muon to faithfully probe the system across the transition. Although this latter feature of differing muon sites in different structural regimes has yet to be widely investigated, it may be a general feature that we should expect in numerous systems.

Chapter 4

Current-mediated control of magnetism in Sr_2IrO_4

The focus of this chapter will be the strontium iridate compound Sr_2IrO_4 (SIO), which is a Mott insulator with $J_{\text{eff}} = 1/2$ [81]. The material is expected to be a metal from both conventional band theory and from a simple Mott-Hubbard picture, but the strong spin-orbit interaction (SOI) from the 5*d* transition metal, which is in competition with the on-site Coulomb energy U, is enough to open up an insulating gap (see [82,83]). The metal-insulator transition into the antiferromagnetic ground state happens at $T_N = 240\,\text{K}$. An interesting property of this material is the strong coupling between its physical properties and the crystal lattice, especially the $\text{Ir}-\text{O}-\text{Ir}$ bond angle (see **Figure 4.1**). It has been found that applying an external electric current can induce a straitening of the bond and a corresponding weakening in the antiferromagnetic order [84], as discussed later.

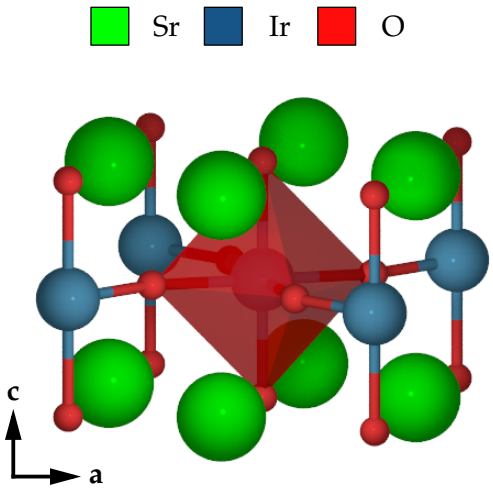

Figure 4.1 Diagram showing part of the crystal structure of Sr_2IrO_4, with the IrO_6 octahedra highlighted and not including the additional rotated layers along the *c*-axis.

The compound under study crystallises in a layered cubic perovskite structure with a long *c*-axis which can be understood as composed of rotated layers (see **Figure 4.1**) [85]. The

material has space group $I4_1/acd$ and lattice parameters $c = 26.24$ Å and $a = b = 5.52$ Å. Its oxygen octahedra are also distorted from the typical arrangement, being stretched by 0.1 Å and rotated around the c-axis by 12°. The full unit cell can then be constructed by rotating each layer by a quarter turn around the $(1/4, 1/4, z)$ point where the oxygen atoms would be if the octahedron wasn't distorted. The magnetic structure is also known to be canted and antiferromagnetic, as shown in **Figure 4.2** and calculated from single crystal neutron diffraction measurements by Ye, Chi *et al.* [86]. When an electric current is applied along the $a - b$ plane, the canting along the b-axis disappears and a decrease in the bulk magnetisation is observed [84]. It is also important to note that below 100 K, and especially below 20 K, evidence exists for a reorientation of the magnetic moment along the c-axis, with the magnetisation measured along the c-axis increasing whilst the ab-plane value decreases [87]. This suggests a potential change in the magnetic structure with canting of spins along the long c-axis of the crystal, the addition of which will help explain the experimental results later.

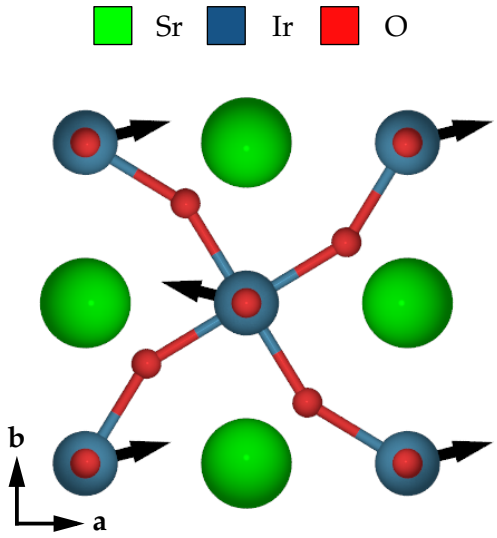

Figure 4.2 Magnetic structure for Sr_2IrO_4 without an applied current as seen along the c-axis.

Some previous studies have also used ZF μ^+SR measurements to probe the magnetic ground state of SIO without an applied current. First the older work by Franke, Baker *et al.* [88], which observed two muon precession frequencies at low temperatures and then the study by Miyazaki, Kadono *et al.* [89] which identified four candidate muon sites

located close to the oxygen atoms. The location of the sites was determined by searching the undistorted structure for local potential minima close to the oxygen atoms where a comparison of the local dipole magnetic field and experimental measurements suggests a value of the Ir moment close to 0.36 μ_B, from x-ray and neutron diffraction measurements. In our analysis we used the smaller value of 0.208 μ_B obtained by Ye, Chi *et al.* [86], explaining some differences in our results which are discussed in **Section 4.3.2**.

The work in this chapter is based on simulations performed by myself at the University of Durham, with the aim is of explaining the unusual results of a series of μ^+SR measurements on Sr_2IrO_4 with and without an applied current performed by collaborators from the Paul Scherrer Institut (PSI) led by Dr Chennan Wang.

4.1 Experimental ZF μ^+SR measurements

To investigate the effect of applying an external current to SIO as series of zero-field μ^+SR measurements were performed on the GPS spectrometer at the Paul Scherrer Institut (PSI) in Switzerland. The sample was composed of a set of small SIO crystals with the long *c*-axis parallel to the muon beam and electrically connected in series with the current running along the *ab*-plane (see **Figure 4.3**).

Figure 4.3 A photograph of the Sr_2IrO_4 sample in the sample holder before measurement.

A series of measurements were taken both with and without applying an external current, to ensure sample quality and that the electrical leads were not interfering with the results.

The results can be found in **Figure 4.4**, showing the magnetic fields corresponding to the two observed muon frequencies with increasing temperature. We find good agreement with previous measurements reported in the literature for the zero-current case whilst when applying a current of 100 mA we observe a reduction in the site fields and a clear splitting in fields at the two muon sites below 100 K, which will be explained later in this chapter with the aid of DFT muon site calculations.

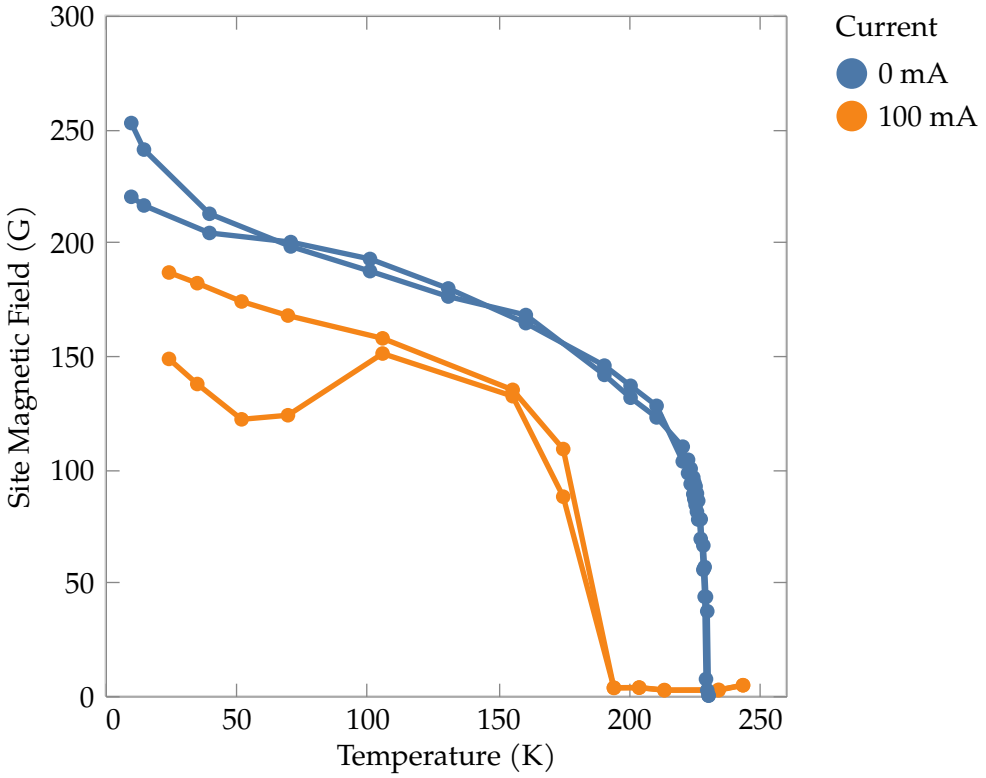

Figure 4.4 Temperature dependence of magnetic field at the muon sites B_i calculated from precession frequencies with and without an external current.

During the current-on measurements, we also had the additional complication that the sample was generating joule heat. An additional flow of helium gas was used to remove the heat and the temperature difference between the sample and cryostat sensors stabilised at around 5 K. This does mean however that the sample temperature is not exactly known and the results in **Figure 4.4** with the applied current are subject to a rescaling, but we expect that there is no significant temperature gradient within the sample.

4.2 Muon site DFT simulation

The muon sites in Sr_2IrO_4 (without an applied external current) were calculated by performing a series of geometry optimisation calculations using the CASTEP program [8] with input files generated by the MuFinder [54] software following the procedure described in **Section 1.3**. A total of 25 initial muon sites were generated and then symmetry reduced in a $1 \times 1 \times 4$ super-cell with the four-fold glide symmetry along the *c*-axis applied. A summary of the parameters of the DFT geometry optimisation calculations can be found in **Table 4.1**.

The muon sites after an external current is applied can be approximated by using the more regular atomic structure determined experimentally, which lacks the rotation of the octahedra, and fixing all the atoms in the unit cell, since the current is expected to hold them in place. We then leave the muon free to relax from its previously calculated site (where there was no current and the atoms were also free to move) in another geometry optimisation calculation.

The dipole field from the iridium magnetic moments is assumed to be the main contribution to the magnetic field at each muon site. It was calculated using the procedure described in **Section 1.1.3** with the muESR library [57], using a $40 \times 40 \times 40$ super-cell and accounting for the distortion caused by the presence of the muon.

Quantity	Value
Energy Cut-off	544.2277 eV
MP k-point grid	$2 \times 2 \times 1$
Supercell	$1 \times 1 \times 1$
Functional	LDA
Spin-polarized?	No
$\Delta E/N_{\text{ion}}$	1.36×10^{-6} eV
$\|\mathbf{F}\|_{\text{max}}$	3.81×10^{-2} eV/Å
$\|\Delta\mathbf{R}\|_{\text{max}}$	4.59×10^{-4} Å

Table 4.1 Parameters of DFT muon site calculations for Sr_2IrO_4 without external current.

4.2.1 Effect of current on muon sites

We first consider the change in the muon site positions as the current is applied, shown in Figure 4.5. For simplicity we show only a single layer of the material, instead of the $1 \times 1 \times 4$ cell with the four-fold glide symmetry used in the DFT simulation, and include only symmetry-inequivalent sites, having averaged over sites with similar positions. The low-energy sites all have the muon close to an oxygen atom (with a distance of 1 Å). We distinguish in-plane sites, where the muon is attached to an oxygen atom in the main octahedral plane (see Figure 4.5a), and apical sites (in the unit cell apex), where the muon is attached to one of the other two vertices of the octahedron (see Figure 4.5b). When the external current is applied the muon sites remain very similar but we have fewer distinct positions, most likely because of the more regular atomic structure.

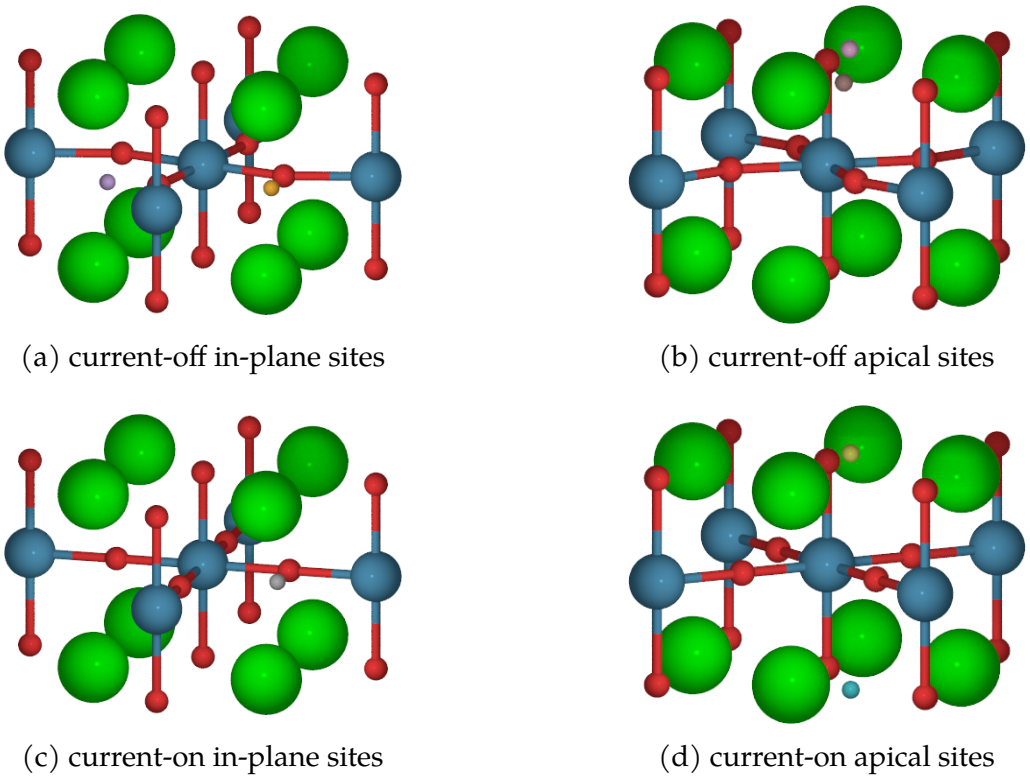

(a) current-off in-plane sites

(b) current-off apical sites

(c) current-on in-plane sites

(d) current-on apical sites

Figure 4.5 Diagrams showing the main symmetry inequivalent muon sites (a) in plane with lower (■) and higher (■) local fields, (b) in the apex with lower (■) and higher (■) energy, (c) in-plane with the current on (■) and (d) in the apex with lower (■) and higher (■) field (but only when $m_z \neq 0$), all with a ferromagnetic magentic structure.

4.3 Simulation of magnetic fields

We can quantify the effect of applying an external current to Sr_2IrO_4 by considering the change to the magnitude of the dipole magnetic field and in general find that with the current on we have fewer distinct muon sites and that the field magnitudes at those sites tend to be higher.

4.3.1 Effect of magnetic moment along *c*-axis

The magnetic structure is not entirely determined, so we consider a small variable magnetic component along the c-axis (in the out-of-plane direction) and that the coupling between adjacent layers can be either ferromagnetic (FM) or antiferromagnetic (AFM). By increasing this m_z component we increase the calculated dipole fields but also induce a splitting in the field predicted at two of the sites. If these sites are realised experimentally, this additional m_z component would explain the observed splitting in the muon frequencies when an external current was applied (see **Figure 4.4**). Note that to simplify the visualisations, which can be found at **Figure 4.6** and **Figure 4.7**, the sites have been grouped in the same way as in **Figure 4.5**, using both the muon positions in the unit cell and the location of the site in the energy-local field magnitude plane. Each site has also been identified with a colour, for two in-plane (■ and ■) and two apical (■ and ■) sites without the current, which changes to three sites, one in-plane (■) and two apical (■ and ■) when it is applied.

4.3.2 Comparison with experimental data

Identifying the different muon sites by the colours used in **Figure 4.5**, we now compare our simulations with the experimental results in **Section 4.1** to determine which ones are realised in each case. When the current is off we have two low-energy and high-field muon sites at 258.93 G (■) and 162.86 G (■) respectively, both at an in-plane position within the unit cell. The first gives a precession frequency that is in agreement with the experimental results, whilst the second site gives a lower field than measured, perhaps because this is not the site that is realised experimentally but a perturbation of the first

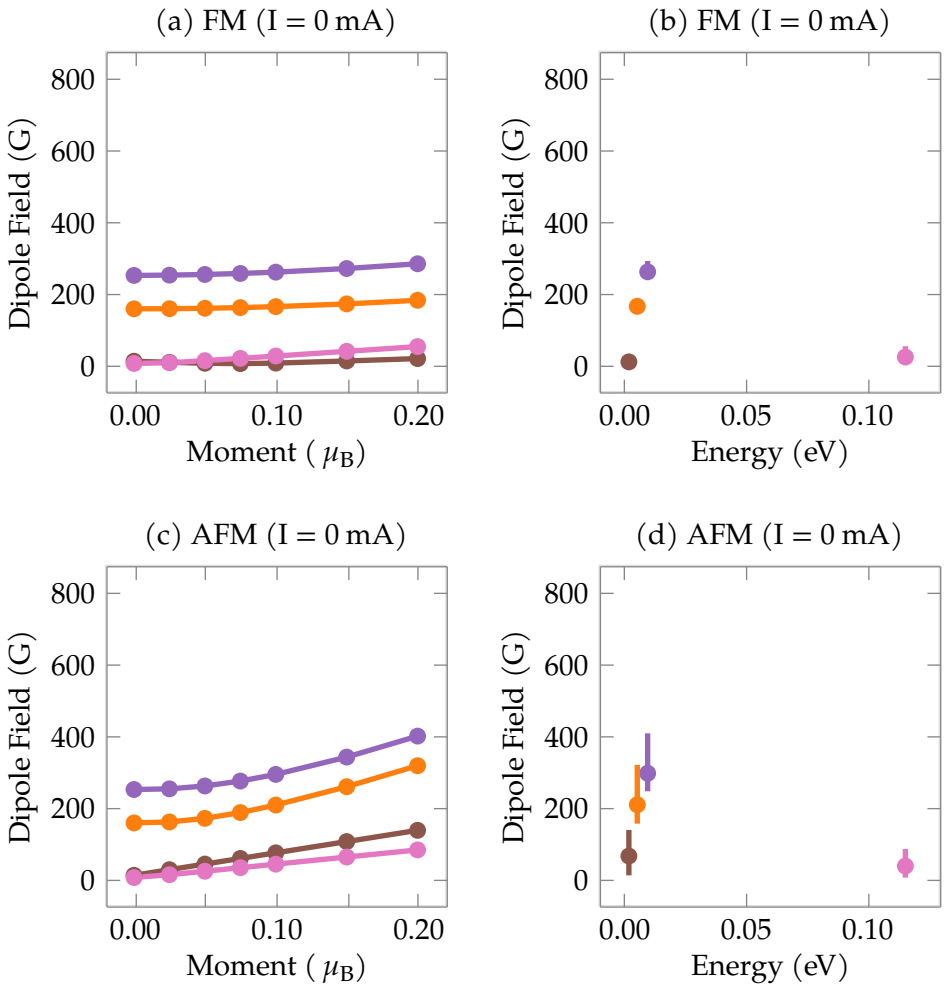

Figure 4.6 Dependence of muon site dipole field on the magnitude of the *c*-axis magnetic moment m_z with FM (top) and AFM (bottom) coupling between layers.

one with a slightly lower local field. The apical sites that we obtained from the simulation in this case don't seem to appear experimentally.

To compare our simulations with the experimental results with the external current we first have to determine a value for the *z*-axis component of the iridium magnetic moment m_z, which had little effect on the calculated fields without the current. To do this we use the field splitting observed with the current on, comparing the ratio B_1/B_2 of the smaller (B_1) and larger (B_2) experimental magnetic fields with the value simulated from the matching muon sites with the ferromagnetic structure which also show the splitting (■ and ■ in **Figure 4.7**). We start by using cubic spline interpolation [90] to fit both the experimental and simulated curves using the `interpolate.CubicSpline` function from

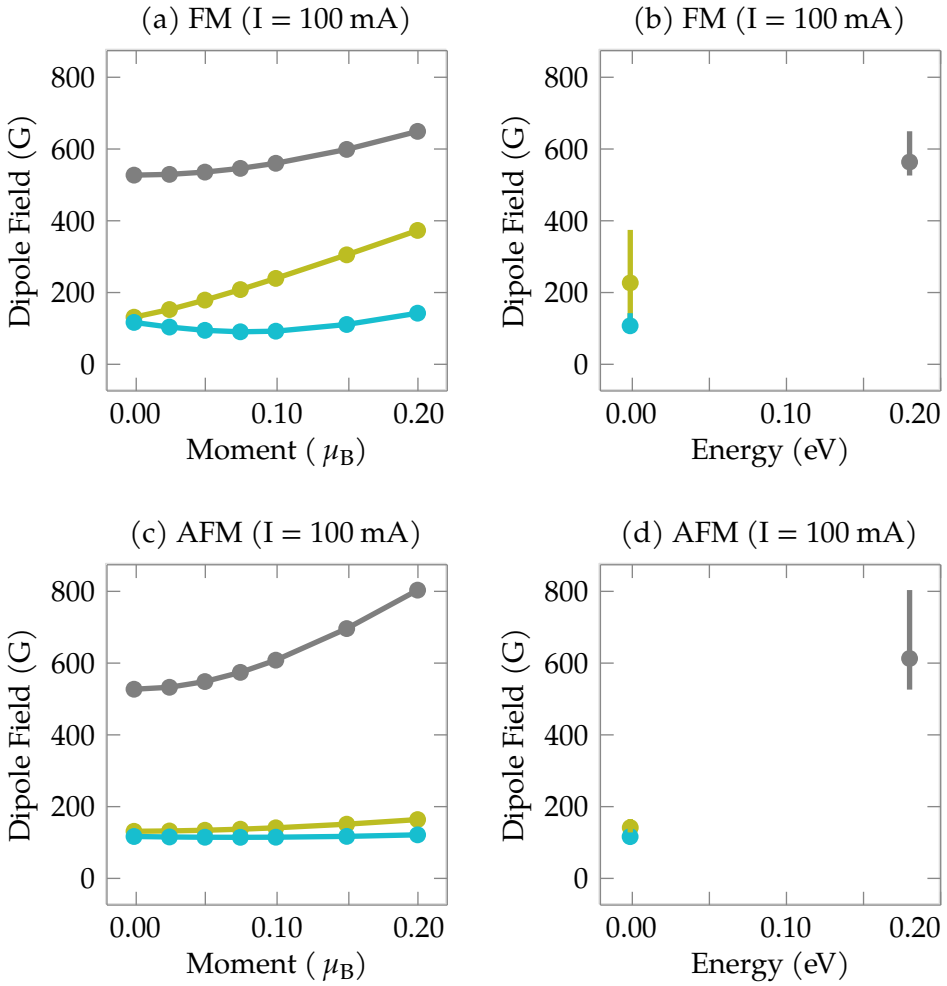

Figure 4.7 Dependence of muon site dipole field on the magnitude of the c-axis magnetic moment m_z with FM (top) and AFM (bottom) coupling between layers.

the `scipy` python library and then calculate the ratio between the two curves (see **Figure 4.8**). Since the simulated ratio (right panel) is a decreasing function of the moment size m_z we can obtain an upper bound to finding the minimal value of the experimental ratio (0.7 at 54.6 K), which corresponds to a value of $m_z \leq 0.0214\,\mu_B$. A comparison of the experimental data and the simulation with the new value of m_z can be found in **Figure 4.9**.

Using this value of m_z we find that when the current is on (at 100 mA) the two muon sites have $B_1 = 102.01\,\text{G}$ (■) and $B_2 = 145.76\,\text{G}$ (■). An interesting observation is that applying the current seems to change the type of site which is realised, making the apical sites more energetically favourable when compared to the in-plane sites which had lower energy without the current (with a difference of 0.2 eV). This change also explains the

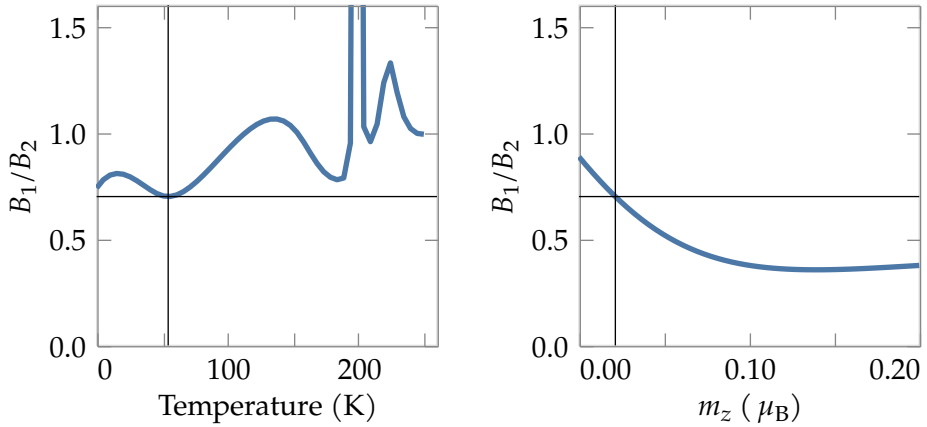

Figure 4.8 Estimation of m_z by matching the minimum ratio between site magnetic fields B_1/B_2 observed experimentally when a current is applied.

observed splitting in field, which is observed only in the apical sites located between layers of Ir atoms and caused by $m_z \neq 0$.

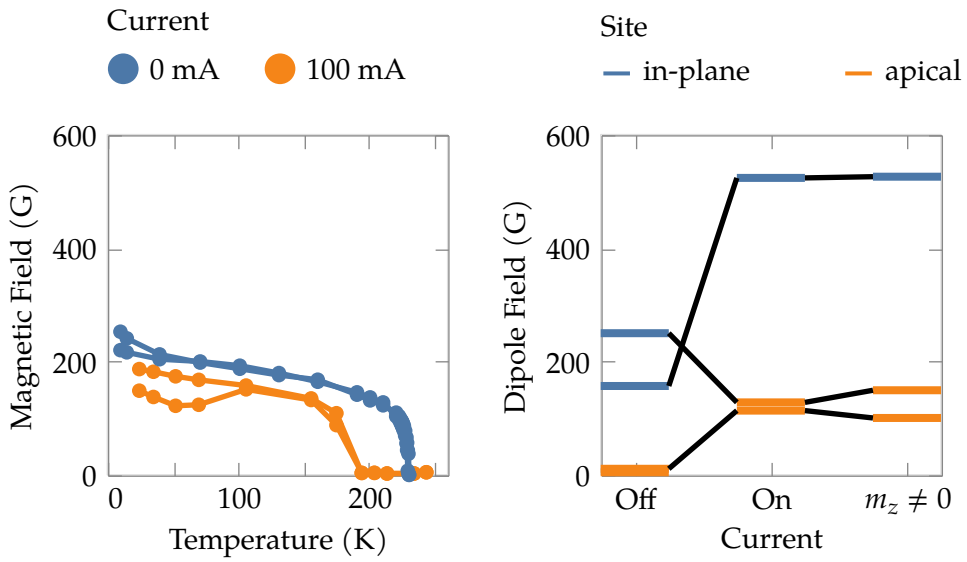

Figure 4.9 Comparison of site magnetic fields calculated from μ^+SR measurements against temperature compared to values simulated from DFT calculations (assuming $T = 0\,\mathrm{K}$) with and without the external current.

Finally, we can compare our results for the calculated muon sites without the external current with those obtained by Miyazaki, Kadono *et al.* [89]. The site positions were given in terms of the spherical polar displacement (radial distance r, polar angle θ and azimuthal angle ϕ) from the closest oxygen atom to each site. A comparison with the DFT calculated sites can be found in **Figure 4.10**, where the lines show the values estimated by Miyazaki, Kadono *et al.* [89] whilst the points show the two polar angles and radius

calculated for each muon site, with reasonable agreement, especially in the azimuthal angle.

The dipole fields reported by Miyazaki, Kadono *et al.* [89] for their different sites can also be found in **Table 4.2**, where we have matched them with our results by first distinguishing between in-plane and apical sites and then sorting by the local field. The discrepancy might be explained by considering the highest frequency site "in-site 1" in their results as not being realised in the DFT simulations and instead matching the in-plane sites with the frequencies identified as belonging to the apical sites.

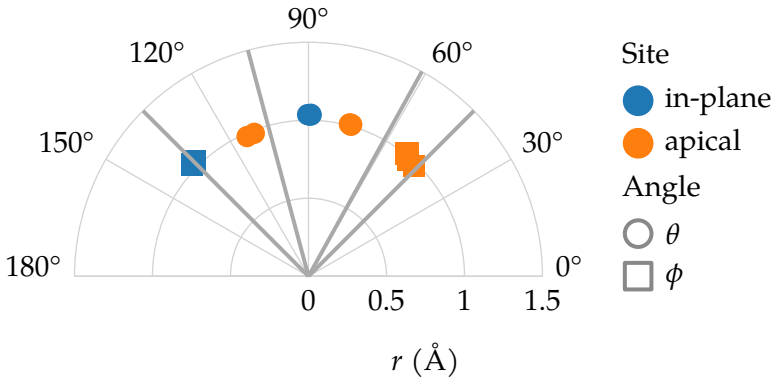

Figure 4.10 Comparison of the spherical polar coordinates θ and ϕ between the calculated muon sites and the nearest oxygen atom with the values calculated by Miyazaki, Kadono *et al.* [89] (shown as dark lines).

Site	Report		Miyazaki	
	f (MHz)	μ_{Ir}/μ_B	f (MHz)	μ_{Ir}/μ_B
in-plane (■)	3.51	0.206	8.2(4)	0.426(2)
in-plane (■)	2.21	0.206		
apical (■)	0.34	0.206	2.941(3)	0.4205(4)
apical (■)	0.07	0.206	2.79(4)	0.389(6)

Table 4.2 A table comparing the results of the DFT simulations with the muon site frequencies measured by Miyazaki, Kadono *et al.* [89], where the muon site have been matched by first distinguishing between in-plane and apical sites and then sorting by the frequency within each category.

4.4 Conclusions

We have used a combination of DFT simulations and dipole field calculations to determine the most likely muon sites responsible for our experimental results. We identify two

classes of sites (in-plane and apical) and find that the first are most likely realised without the current, which when applied changes the relative energies of the two classes and makes the second more energetically favourable. The apical sites also have lower dipole fields, explaining the decrease with current seen in experimental measurements (see **Figure 4.9**). Additionally, we can explain the splitting in field seen with the current applied by adding a slight ferromagnetic canting to the magnetic structure along the c-axis (with $m_z \leq 0.0214\,\mu_B$), which differentiates two previously degenerate apical sites.

In conclusion, knowing that the applied current induces a change in the atomic and magnetic structure of SIO, we would expect the experimental results to be explained by a corresponding change in the environment of the same muon site. We instead find that muon sites from a different class are realised, an unusual feature which confirms the usefulness of calculating possible muon sites through a method like DFT+μ when analysing the results of an experiment. Interestingly, a similar feature of a structural phase transition changing which muon sites are likely realised was also seen in the crystalline organic compound HbimDTDA as described in **Chapter 3**. Unfortunately, although we have used the energy of each site for this purpose, it is not always an indicator of how likely a given site is to be realised experimentally or the relative occupancy of many possible sites. The process by which a muon that enters a sample with an initial energy of around 4 MeV thermalises through interactions with other particles before settling into a site (ignoring possible quantum effects) is not well understood and depends on the capture cross-section of the different local minima in the electronic structure and the effect that the presence of the muon itself has on the other atoms. An avenue of further work is therefore the simulation of the muon stopping process itself, with the aim of approximating this cross-section, a topic which is discussed in more detail in **Chapter 7**.

Chapter 5

Determining low-temperature magnetic order in chiral spin chains

---

With the aim of engineering molecules with desirable quantum magnetic properties, we consider the chiral spin chains $[Cu(pym)(H_2O)_4]SiF_6 \cdot H_2O$ and $[Ni(pym)(H_2O)_4]SO_4$ (pym = pyrimidine), abbreviated as CPM and NPM respectively. Their structures are analogous, with each unit cell containing one-dimensional chains of magnetic ions (Cu and Ni respectively) related by a 4_1 screw symmetry along the chain (see **Figure 5.11**). One important difference is that CPM has $S = 1/2$ whilst NPM, due to its different magnetic ion, has a spin of $S = 1$.

The compounds belong to the larger class of 1D spin chains, where we have one dimensional arrangements of spins which are assumed to approximately interact only with their nearest neighbours along the chain. One of the simplest models of this is the Heisenberg isotropic antiferromagnetic $S = 1/2$ chain (sometimes called the XXX model), which has a Hamiltonian of the form

$$H = -J\left(\sum_i \mathbf{S}_i \cdot \mathbf{S}_{i+1}\right). \tag{5.1}$$

This system can be solved exactly using the Bethe Ansatz [91], with the resulting ground state being disordered and supporting fractionalised spinon excitations. There exist several good experimental realisations of this model (see [92, 93]), for example, copper pyrazine dinitrate $Cu(pyz)(NO_3)_2$ (pyz = pyrazine) [94], composed of $S = 1/2$ copper atoms linked by pyrazine rings and well-separated from other chains by the nitrates, follows the predicted behaviour until very low temperatures.

Another interesting example of a spin chain is the staggered $Cu(pym)(NO_3)_2(H_2O)_2$ (pym = pyrimidine) [95], where we still have copper magnetic ions but the nitrogen atoms in the rings are in a different position. This means that the copper ions are not arranged linearly but in a zig-zag pattern, giving rise to a staggered internal field perpendicular to any applied field. This is due to the alternating g-tensors along the chain as well

as Dzyaloshinskii-Moriya (DM) interactions. The resulting system is well described by the sine-Gordon quantum field theory, which predicts a soliton / anti-soliton excitation spectrum and a field-dependent spin gap [96].

A question about a spin chain which μ^+SR is especially well suited to answer is the nature of the ground state and its magnetism. On theoretical grounds the ground state should be disordered for both the linear and staggered chains, but the realisations described above are only quasi-1D due to a small but non-zero inter-chain coupling, which dominates at very low temperatures and induces a magnetic order.

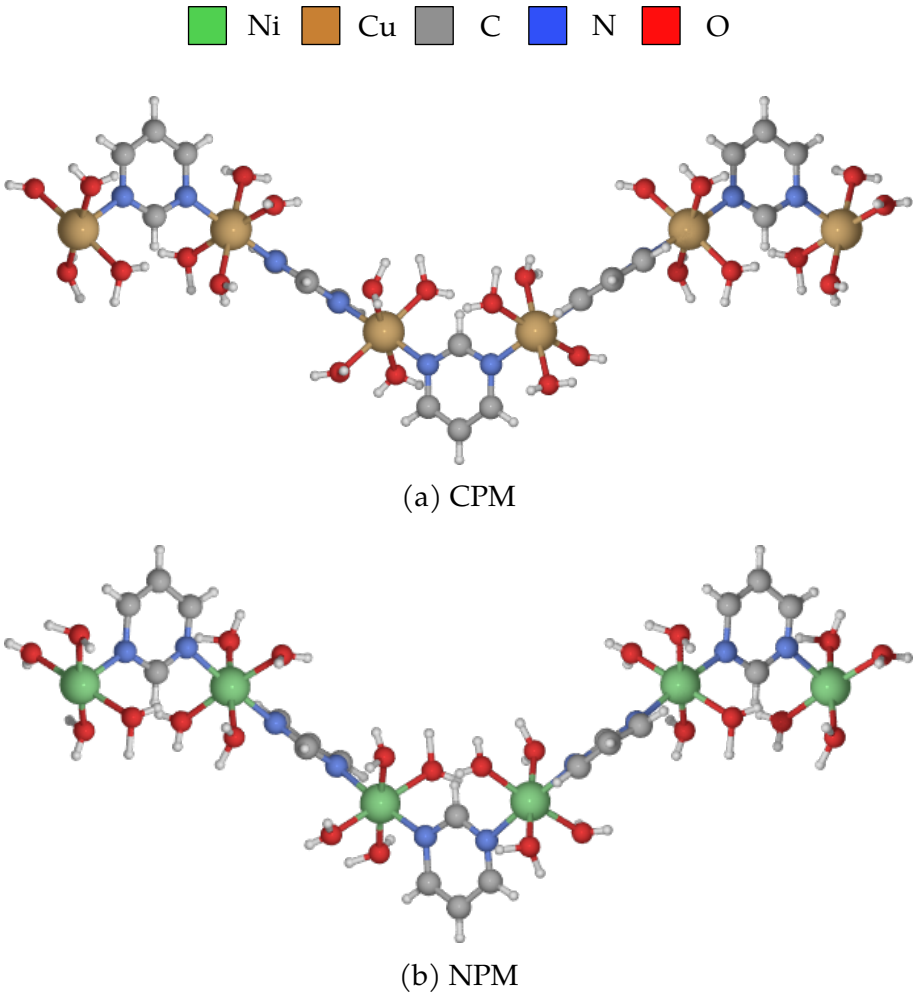

(a) CPM

(b) NPM

Figure 5.1 Diagram showing the atomic structure of both chiral compounds, ignoring all atoms between chains.

The work in this chapter is based on data analysis and simulations performed by myself at the University of Durham. The measurements for CPM were taken by Tom Lancaster and

collaborators whilst the NPM ones were taken by myself with help from Thomas Hicken. The analysis was also supported by neutron scattering measurements performed by Paul Goddard and collaborators from the University of Warwick. Both samples were prepared by Jamie Manson at Eastern Washington University.

5.1 Nickel chiral chain

5.1.1 Zero-field μ^+SR measurements

To investigate the low-temperature behaviour and ground state magnetism of the NPM spin chain a series of zero-field μ^+SR measurements were performed using the FLAME instrument at the Paul Scherrer Institut (PSI) facility in Switzerland on a polycrystalline sample of $[Ni(pym)(H_2O)_4]SO_4$ (pym = pyrimidine). We started by cooling the sample down to the lowest temperature reachable by the cryostat of around 20 mK and then took a series of measurements at increasing temperatures in steps of 0.2 K. Each measurement recorded 35 MEv in about 60 min, with the temperature changes taking 5 min between them. An example of the measured spectra can be found in **Figure 5.2**.

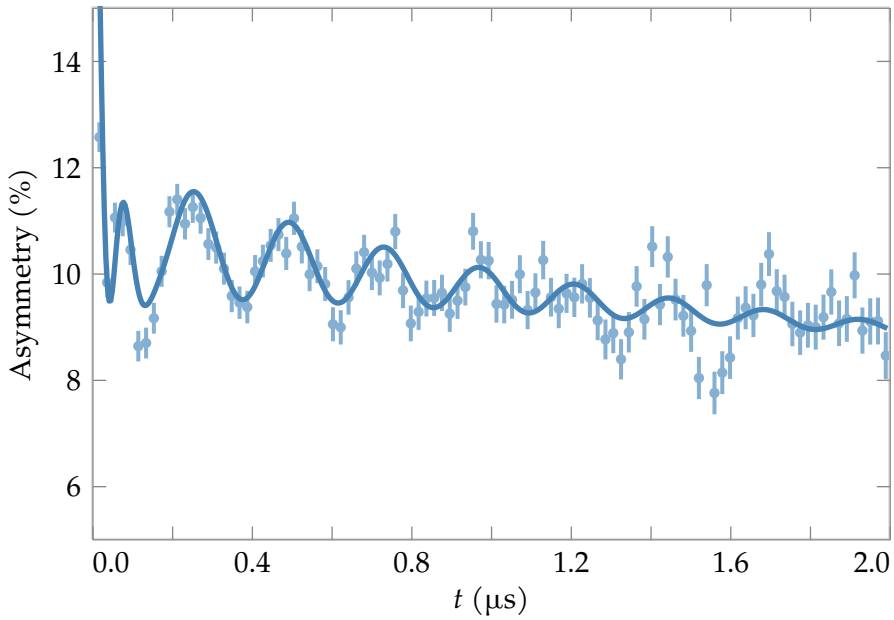

Figure 5.2 Example of ZF μ^+SR spectra measured on NPM at $T = 0.2$ K.

We found evidence for a phase transition and that the spectra in the low-temperature phase are well described by a sum of two oscillating relaxing components, giving a fitting function of the form

$$\begin{aligned} A(t) = & A_{\mathrm{R}} \cos(\omega t + \phi_{\mathrm{R}}) \exp(-\lambda_{\mathrm{R}} t) \\ & + A_{\mathrm{r}} \cos(a\omega t + \phi_{\mathrm{r}}) \exp(-\lambda_{\mathrm{r}} t) \\ & + A_{\mathrm{l}} \exp(-\lambda_{\mathrm{l}} t) \\ & + A_{\mathrm{b}} \,, \end{aligned} \tag{5.2}$$

where we fix the values of $A_{\mathrm{b}} = 8\%$ and $\lambda_{\mathrm{l}} = 0.55\,\mu\mathrm{s}^{-1}$. We also performed a global fit across all temperatures for some of the parameters, obtaining $A_{\mathrm{l}} = 2.92 \pm 0.02\%$, $A_{\mathrm{R}} = 2.23 \pm 0.07\%$, $A_{\mathrm{r}} = 11.1 \pm 0.1\%$, $\phi_{\mathrm{R}} = -31 \pm 2°$ and $\phi_{\mathrm{r}} = -20 \pm 1°$. The most important parameter, which was also fitted globally, is $a = 2.66 \pm 0.04$ the ratio between the two oscillating frequencies. The evolution of the remaining parameters as a function of temperature can be found in **Figure 5.3**. The fact that the above model fits the experimental data below the phase transition suggests that we have an ordered magnetic structure experienced by muons stopping at two different sites. We can characterise the transition by fitting the two frequencies to a phenomenological model of the form

$$\omega(T) = \omega_0 \left[1 - \left(\frac{T}{T_{\mathrm{N}}} \right)^{\alpha} \right]^{\beta}, \tag{5.3}$$

where all the parameters are kept equal between them expect ω_0. Since we have so few points around the transition, we fix $\alpha = 3$ to obtain $T_{\mathrm{N}} = 1.82 \pm 0.02\,\mathrm{K}$ and $\beta = 0.22 \pm 0.07$. The value of β would usually give the value of the critical exponent around the transition, but in this case the fit should be treated more as a parametrisation with little physical meaning due to the small number of data points close to T_{N}.

In conclusion, by fitting the measurements of the ZF μ^+SR spectra at different temperatures we confirm that a phase transition from a magnetically ordered low-temperature state to a more disordered state at higher temperatures exists, with the change happening around $T_{\mathrm{N}} = 1.82 \pm 0.02\,\mathrm{K}$. The fitting of the two distinct oscillation frequencies will also help us understand the nature of the magnetic ground state, since it suggests that

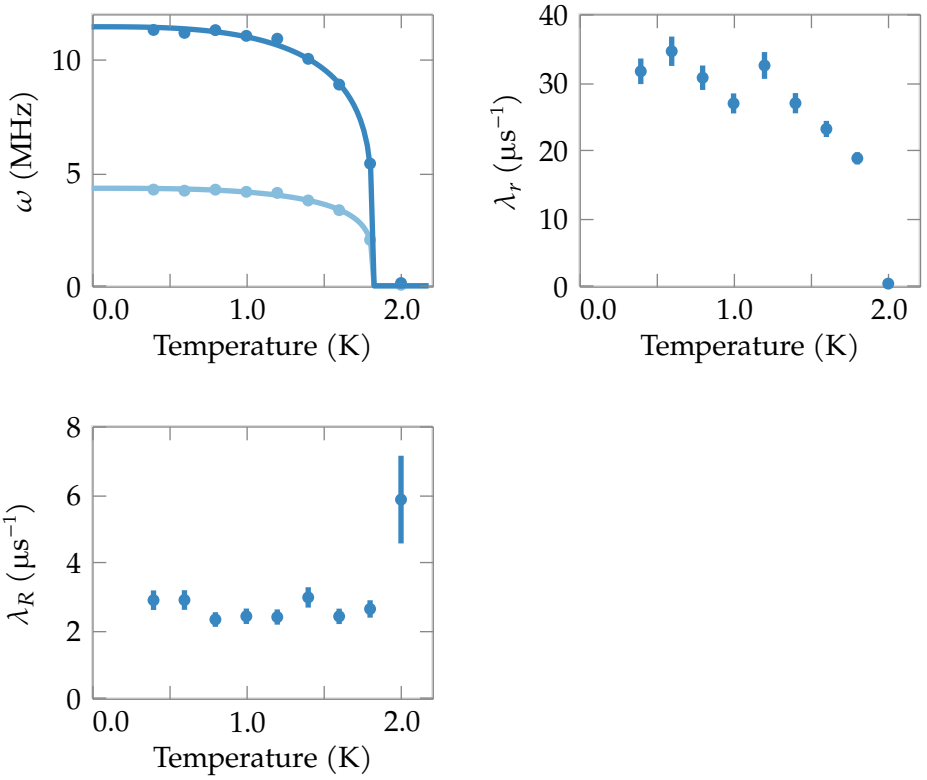

Figure 5.3 Temperature dependence of parameters in fitting of low-temperature ZF measurements of NPM chain.

the muons in the system realise two distinct sites and that the ratio between the magnetic fields at the muon sites is given by

$$\frac{B_1}{B_2} = \frac{\omega_1}{\omega_2} = a = 2.66 \pm 0.04\,, \tag{5.4}$$

where we have assumed that the magnetic moments on all the nickel atoms in the chain are equal. We can then compute a set of candidate muon sites by using DFT and simulate the expected field at each site given different possible magnetic structures to determine the most likely one.

5.1.2 Calculation of candidate muon sites

The muon sites in the NPM chain material were calculated by performing a series of geometry optimisation calculations using the CASTEP program using the method described in **Section 1.3** and making use of the ensemble DFT procedure mentioned in **Section 1.2.4.3**, since the faster density mixing method failed to converge for this system. The MuFinder [54] program was used to generate the CASTEP input files required to

run the calculations. A total of 30 initial muon sites were generated in a compromise between computational cost and finding all low-energy sites, since the unit cell has a large size (7.93 Å× 7 . 93 Å× 18 . 45 Å). A summary of the DFT parameters can be found in Table 5.1.

Quantity	Value
Energy Cut-off	625.862 eV
MP k-point grid	2 × 2 × 1
Supercell	1 × 1 × 1
Functional	LDA
Spin-polarized?	No
$\Delta E/N_{\text{ion}}$	1.18×10^{-6} eV
$\|\mathbf{F}\|_{\text{max}}$	0.026 eV/Å
$\|\Delta\mathbf{R}\|_{\text{max}}$	7.31×10^{-4} Å

Table 5.1 The parameters of DFT muon site calculations for NPM.

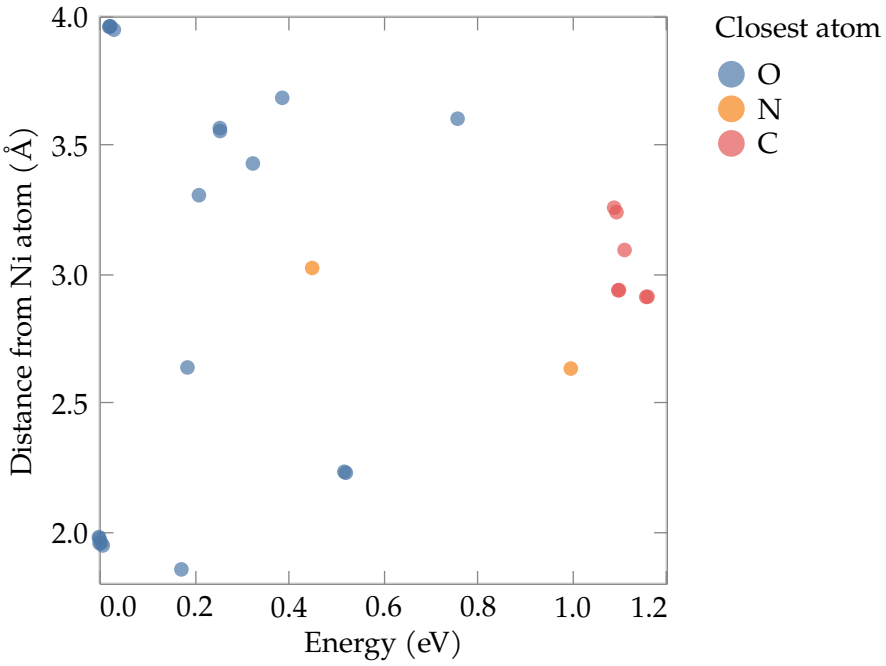

Figure 5.4 The energy of candidate muon sites above the minimum one against distance to the closest nickel atom.

After relaxation, we find a large set of possible sites, with the lowest energy ones having settled close to the most electro-negative atoms in the unit cell (mainly O atoms). This means that we can classify the sites by the nearest element, giving three classes: O, N and C. We can then plot the energy of each structure against the distance to the nearest nickel

atom (as a proxy for the distance from the chain), giving the plot found in **Figure 5.4**. The lowest energy sites have the muon positioned close to one of the 4 oxygen ions around the nickel ions in the chain (see **Figure 5.11b**), either along the Ni−O bond or between the oxygen atoms of two adjacent chains.

To summarise, by performing a series of DFT calculations we have found many candidate sites, which is not unexpected considering the complexity of the atomic structure, but can conclude that the most likely to be occupied by a muon (due to having the lowest energies) are very close to the oxygen atoms in the structure.

5.1.3 Calculation of dipole fields

Once the muon sites have been simulated we can calculate the dipole field contribution at each location for different magnetic structures, with the ultimate aim of matching a pair of sites to the experimental results. The field at a given site can have multiple contributions (see **Section 1.1.3**), but in this case the dominant term is the dipole interaction [17] with the nickel electronic moments in the chain which is given by

$$\mathbf{B}(\mathbf{r}_\mu) = \sum_i \frac{3(\mathbf{m}_i \cdot \mathbf{r}_i)\,\mathbf{r}_i}{(r_i)^5} - \frac{\mathbf{m}_i}{(r_i)^3}\,, \tag{5.5}$$

where $\mathbf{r}_\mu$ is the muon position, $\mathbf{r}_i = \mathbf{R}_i - \mathbf{r}_\mu$ is the vector to each of the magnetic atoms and $\mathbf{m}_i$ is the magnetic moment of that atom. The sum is usually performed over all the atoms in a sphere of comparable diameter to the super-cell, since the magnitude of the field decays relatively quickly.

The most likely magnetic structure, as deduced by our collaborators at the University of Warwick led by Dr Paul Goddard using neutron scattering measurements, is a canted antiferromagnetic one. The spins point mainly along the length of the chain, but the moments are anti-aligned both along it and between adjacent atoms in neighbouring chains (like XZA in **Figure 5.11**). We also expect a degree of canting away from this axis, as well as a quarter-turn rotation along each chain, to respect the four-fold screw symmetry of the atomic structure. An example of the proposed magnetic structure can be found in **Figure 5.5**. The magnitude of the nickel magnetic moment was also estimated to be about $1.55\,\mu_B$.

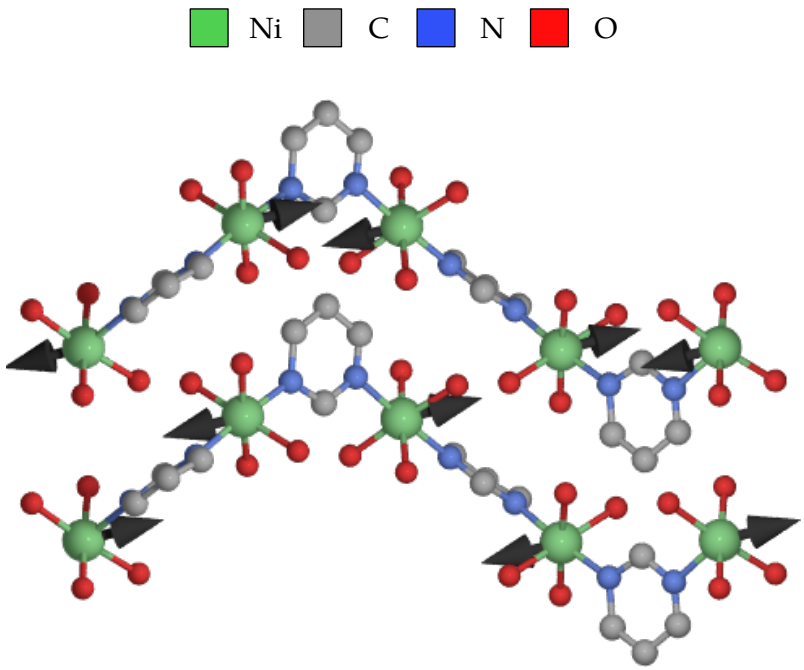

Figure 5.5 Candidate magnetic structure of nickel chiral chain.

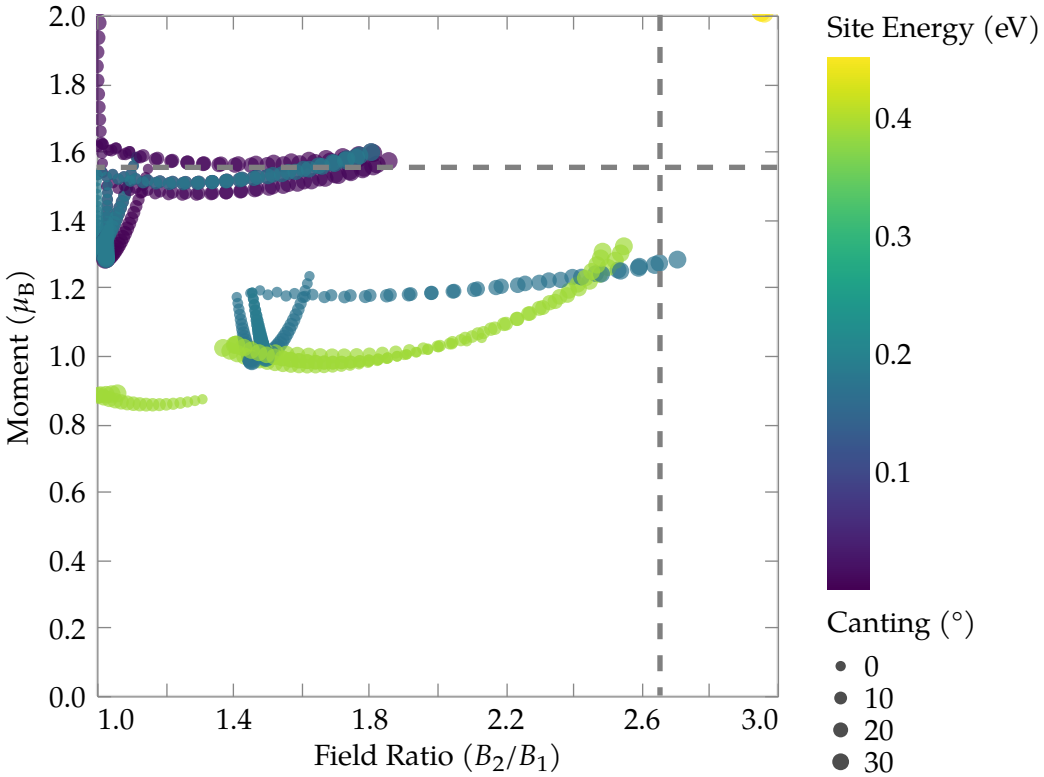

Figure 5.6 The ratio between site fields and required magnetic moment for all pairs of sites with different amounts of moment canting.

To perform the calculation of the dipole field the muESR library [57] was used. For

each possible value of the canting angle the field was calculated at each candidate site using a $40 \times 40 \times 40$ super-cell and the distortions due to the presence of the muon in the central cell were accounted for by adding the field due to a single distorted cell and subtracting the same for an undistorted one, taking advantage of the fact that magnetic fields combine linearly. We can then compare with the experimental results to deduce the most likely pair of sites and the amount of canting in the magnetic structure.

The results of this calculation can be found in **Figure 5.6**, where each point represents a pair of sites and all sites are considered. On the x-axis we have the ratio between the dipole fields at the sites whilst on the y-axis we have the nickel magnetic moment that would be required to match the observed frequencies in the muon asymmetry. The size of each point is proportional to the moment canting in the structure whilst its colour represents the higher single-point energy of the relaxed structures in the site pair above the lowest energy structure among all the sites (as a measure of how likely a given pair is to be realised).

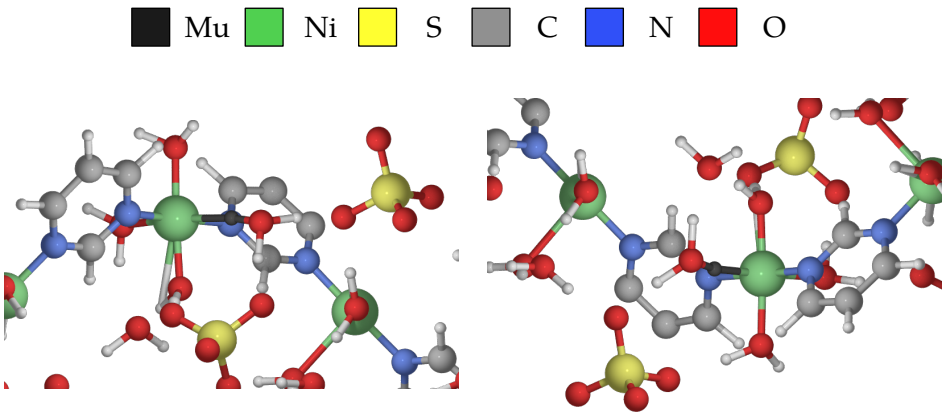

(a) Site 1 (b) Site 2

Figure 5.7 Location of most likely muon sites in nickel chiral chain.

From this analysis, we find that the most likely sites are between a nickel atom from the chain and a nearby oxygen atom (see **Figure 5.7**), which are also the lowest energy sites in **Figure 5.4**. The required nickel moment for this pair is around 1.27 μ_B, found by repeating the calculation for a range of canting angles in steps of 2°. The sites also have energies of 0 eV and 0.17 eV above the minimum, low enough that their realisation is plausible. We also find that the canting angle of the magnetic structure can significantly affect the

results, with the predicted angle being 34°, more than the 18° suggested by the neutron measurements. The fact that the analysis only considered the dipole contribution to the magnetic field should also be kept in mind, since including other terms might help to match the experimental results more closely.

In conclusion, by combining a series of ZF μ^+SR measurements with simulations of possible muon sites and the magnetic field expected at each one from different magnetic structures we can explain the observed results. We find that the candidate muon site between the nickel and oxygen atoms in the chiral chain is realised and can confirm that our measurements are consistent with the ferromagnetic canted structure suggested by neutron scattering measurements.

5.2 Copper chiral chain

An interesting property of the CPM chiral spin chain under consideration, with formula $[Cu(pym)(H_2O)_4]SiF_6 \cdot H_2O$ and spin $S = 1/2$, is that unlike most other examples it remains disordered to the lowest measured temperatures of 20 mK, as confirmed by ZF μ^+SR measurements [97]. Bulk magnetisation measurements $M(H)$ for both crystal and power samples of this compound [98] also provide subtle evidence of a phase transition starting at around 3 T, perhaps caused by the additional terms in the spin chain Hamiltonian arising from the four-fold chiral symmetry. Our investigation on this compound therefore focuses on whether the application of an external magnetic field serves to stabilise a magnetic order, and if so whether we can identify more than one ordered phase with increasing field.

5.2.1 Transverse Field MuSR measurements

To investigate the response of the CPM compound to an external magnetic field we use the transverse-field (TF) μ^+SR technique, where a field is applied perpendicular to the initial muon spin. This means that the spin will process around in the combined external and local magnetic field until decay, giving a polarisation that approximates the cosine transform of the field probability distribution $p(B)$ at the muon site

$$P(t) = \int_{-\infty}^{\infty} p(B) \cos\left(\gamma_\mu B t\right) dB \,. \tag{5.6}$$

The measurements were taken using the HAL-9500 instrument from the Swiss Muon Source (SμS) at the Paul Scherrer Institut (PSI). After cooling down the polycrystalline sample made by combining many small crystallites down to 100 mK, we performed a scan in increasing magnetic field in intervals of 1 T, measuring 3.5 MEv per detector over a period of 4 h for each point.

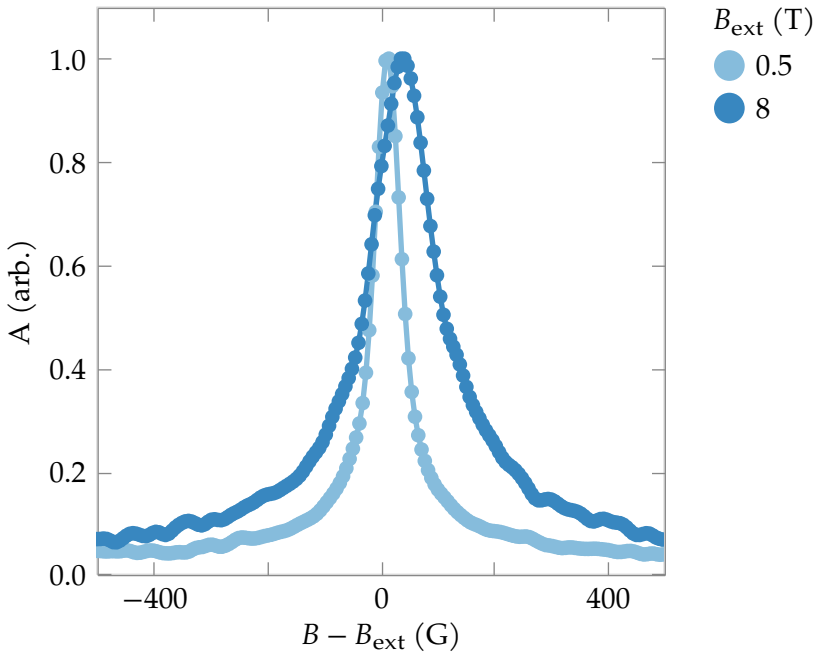

Figure 5.8 Examples of TF μ^+SR Fourier transformed polarisation spectra of CPM.

The resulting spectra for the CPM chain after applying the Fourier transform contained a single broad peak, as seen in **Figure 5.8**. As the external field increases the peaks become broader and shift away from the applied field. We can quantify this change by fitting each peak to a Lorentzian curve of the form

$$\hat{P}(B) = \frac{Aw^2}{\left[(B - B_0)^2 + w^2\right]} + A_0\,, \tag{5.7}$$

where A is the height of the peak, w its width, B_0 is center and A_0 a baseline. Since the external field B_{ext} is much higher than all the internal fields at the muon site it will dominate, and so the peak location B_0 will be at a small offset away from it.

As shown in **Figure 5.9**, after fitting the measurements to this model we find that as a function of the external field the field distribution gets wider and shifts away from the applied field. We also observe a discontinuity in the B_0 parameter around $B = 3\,\mathrm{T}$ which

provides evidence of a field-induced phase transition. We can then perform a series of simulations to explain the results, concluding that the most likely explanation is the the system remains disordered below the transition, but then orders into a commensurate magnetic structure above the phase transition.

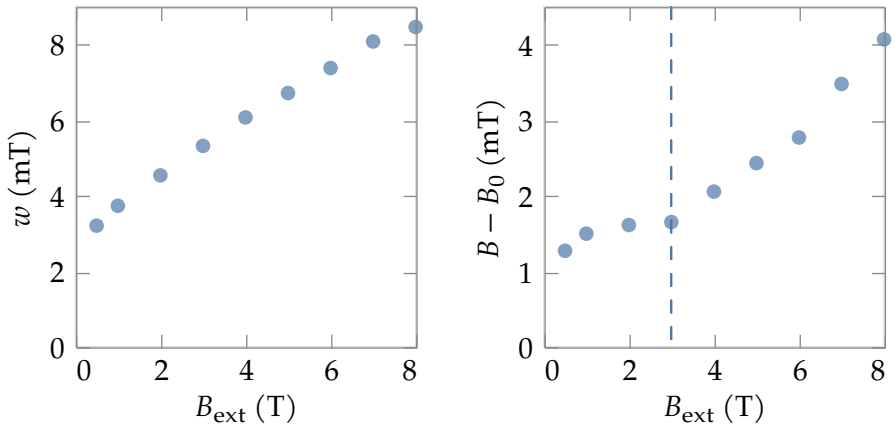

Figure 5.9 Parameters of fit to Lorentzian model of CPM TF μ^+SR spectra peaks.

5.2.2 DFT calculation of muon sites

Following a procedure identical to the one presented in **Section 5.1.2**, the muon sites for the CPM compound we calculated by randomly selecting initial candidate positions and then performing a structural relaxation using DFT. A total of 45 initial muon sites were generated in a compromise between computational cost and finding all low-energy sites, since the unit cell has a large size (11.2 Å×11.2 Å×19.3 Å). A summary of the parameters used in the DFT calculations can be found in **Table 5.2**.

After the geometry optimisation we find that most muons appear to have relaxed from their random positions into positions close to an atom, although the details are not very clear due to the complexity of the structure and large number of atoms. We therefore investigate the character of each site by considering the distance to its nearest atomic neighbours instead, focusing on those with a value between 1–2 Å and ignoring hydrogen. This reveals that each site is close to two atoms and that the muon appears to have settled in the middle of the bond between them (see **Figure 5.10**). An interesting observation is that for the most common O−F sites the presence of the muon distorts the unit cell by stretching the bond between the associated oxygen and a nearby copper atom, breaking the symmetry around the only magnetic ion.

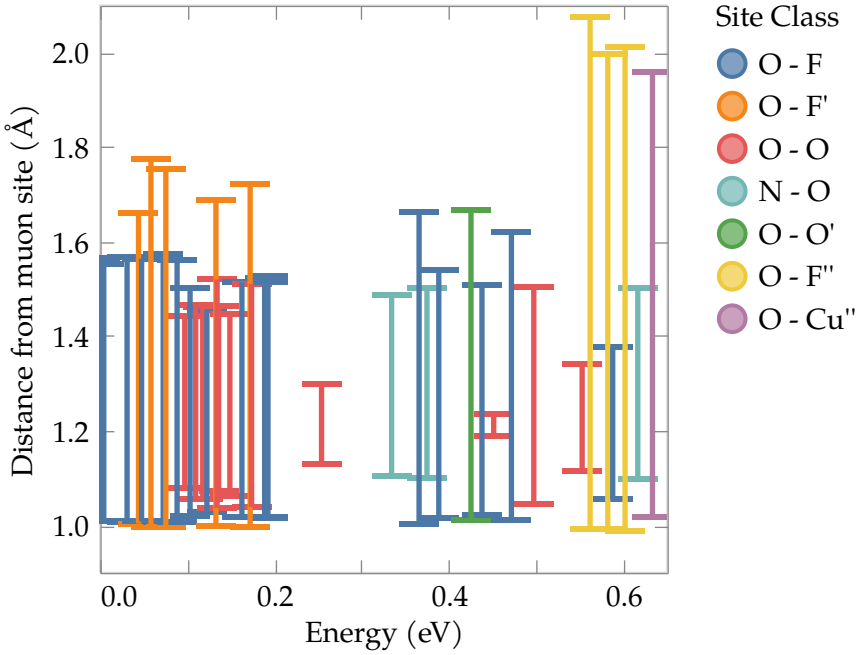

Figure 5.10 The distances from the muon site to the two nearest atoms (excluding hydrogen).

Quantity	Value
Energy Cut-off	544.23 eV
MP k-point grid	$1 \times 1 \times 1$
Supercell	$1 \times 1 \times 1$
Functional	LDA
Spin-polarized?	No
$\Delta E/N_{\text{ion}}$	1.73×10^{-6} eV
$\|\mathbf{F}\|_{\text{max}}$	0.043 eV/Å
$\|\Delta\mathbf{R}\|_{\text{max}}$	5.02×10^{-4} Å

Table 5.2 Parameters of DFT muon site calculations for CPM.

In summary, after performing a series of DFT calculations we have found a large number of possible muon sites in the CPM compound. This is not unexpected and very similar to the analogous NPM chiral chain (see **Figure 5.4**), with the lowest energy, and so most likely, sites located close to the oxygen atoms around the magnetic ion (Cu and Ni respectively). An interesting difference is that whilst the sites that were ultimately realised in NPM had the muon along the Ni − O bond, with CPM we find that the analogous low-energy site is instead on the other side of the oxygen atom, perhaps attracted by the nearby electro-negative F atom. The closeness to the fluorine nuclei is expected, since in a system

with them this is usually where the muon sites will be found, a fact that can usually be identified from a $F-\mu$ signal in the ZF asymmetry $A(t)$ (see [25,26]).

5.2.3 Dipole fields with possible magnetic structures

Once we have determined the possible muon sites in the CPM compound, the next step is to calculate the magnetic field at each muon position from the copper magnetic moments in the compound. The exact arrangement of the copper spins is not known, but a series of possible structures can be found in **Figure 5.11**, where we classify them according to the plane along which the spins lie (XZ or XY) and the relative orientation between spins in adjacent chains (ferromagnetic or antiferromagnetic). This means that we have four possible commensurate structures, two where the spins are aligned along the length of the chain and the spins are either parallel (XZF) or anti-parallel (XZA) between adjacent chains and two where the spins are perpendicular to the chain direction and the spins are again either parallel (XYF) or anti-parallel (XYA). In all cases adjacent spins in the same chain are anti-parallel.

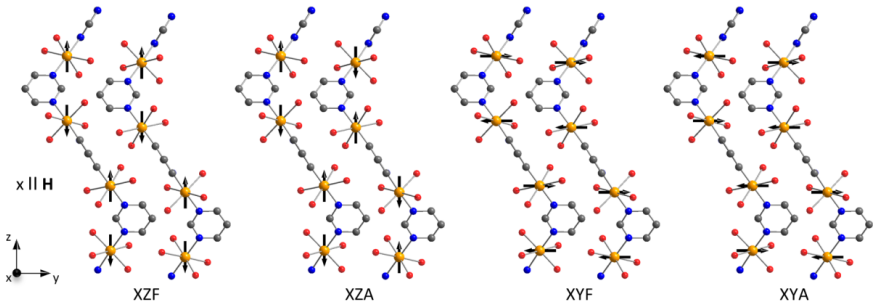

Figure 5.11 Possible magnetic structures when a magnetic field is applied perpendicular to the chiral chain [99].

We can then calculate the dipole field due to the commensurate magnetic structures in the same manner as with the NPM chiral chain (see **Section 5.1.3**) by computing a sum over the magnetic moments in a large super-cell of the compound. From neutron scattering measurements [100], we expect that above the transition the compound adopts the XYF structure and so a possibility that we considered is that below 3 T we have an incommensurate helix where the nearest neighbors along the chain are rotated by $180° + \epsilon$ to give a structure which is a small perturbation away from the XYF one. The magnetic moments

of the incommensurate helical structure [101] can be calculated by first computing the Fourier components $\mathbf{S}_{\nu\mathbf{k}}$ which reproduce the XYF magnetic moments $\mathbf{m}_{n\nu}$ at atom ν and unit cell n as a helix

$$\mathbf{m}_{n\nu} = \sum_{\mathbf{k}} \mathbf{S}_{\nu\mathbf{k}} \exp[-i(\mathbf{k}\cdot\mathbf{R}_n)] = \cos(\mathbf{k}\cdot\mathbf{R}_n + \phi_n)\,\mathbf{a} + \sin(\mathbf{k}\cdot\mathbf{R}_n + \phi_n)\,\mathbf{b}\,, \quad (5.8)$$

where $\mathbf{k}$ is a propagation vector which describes the direction and periodicity of the helix and the vectors $\mathbf{a}$ and $\mathbf{b}$ define the axis of its ellipse (see [102] for details). For the case of the chiral chain in the XYF arrangement we can choose the x and y axis as the ellipse vectors and $\mathbf{k} = (0, 0, 4\pi)$ as the propagation vector, adjusting the phases to match the spin directions in the unit cell. To then obtain a small helical perturbation we just need to increase the magnitude of the propagation vector to $k + \Delta k$. For the rest of this chapter unless stated otherwise calculations involving the helical magnetic structure use a value of $\Delta k = 2\pi \times 0.005$, which corresponds to a canting angle of $\epsilon = 0.45°$. This value was chosen as a placeholder until the effect of this parameter can be quantified better when fitting to experimental data.

For the incommensurate case of the helical structure the dipole field was calculated using the method described in the supplemental material of [103] on a larger super-cell comprising $100 \times 100 \times 100$ cells. In this case the result will not be a single magnetic field vector but a set of field vectors with magnitudes expected to follow a distribution of the form (see [104]):

$$p(B) = \frac{2}{\pi}\left[\frac{B}{\sqrt{B^2 - (B_{\min})^2}\sqrt{(B_{\max})^2 - B^2}}\right], \quad (5.9)$$

where $B_{\min}$ and $B_{\min}$ are the minimum and maximum field magnitudes respectively. An example of one such distribution as compared to a fit of the model can be found in **Figure 5.12**, showing excellent agreement.

We can use the fact that the helical distribution is characterised only by its limits to condense all the dipole field results into **Figure 5.13**. Here we see the magnetic fields calculated at each of the muon sites (differentiated by the energy excess calculated by CASTEP over the site with the lowest energy) for all the commensurate structures (represented by triangles with different directions) and the limits of the helical field distribution. Some features of note are that for the low-energy sites which are likely to be realised

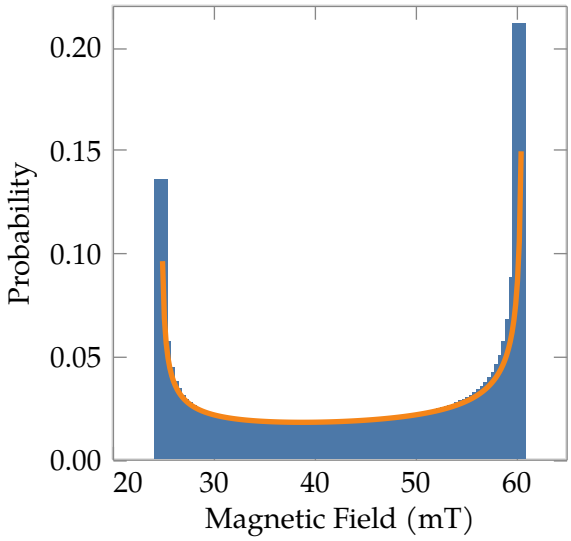

Figure 5.12 Comparison of the theoretical distribution (solid line) and the sampled field histogram.

the commensurate magnetic fields are very similar, with some exceptions like the O−F and O−O sites between 0.1 eV< E < 0 . 2 eV. For these sites we also find that the helical distribution is consistently higher than the commensurate fields, which might provide a way of distinguishing the two possible magnetic structures in experimental data. Finally, to investigate the effect of the deviation of the helix from the XYF structure we can consider the field distribution for different values of Δk as shown in **Figure 5.14** for the O−F sites, where we see that the distribution seems to oscillate between two forms. A similar effect is observed in the distribution at the other muon site types.

5.2.4 Polycrystalline sample in magnetic field

Having calculated the dipole field at each of the muon sites we can now simulate the muon polarisation $P_z(t)$ that one would expect to measure from a muon at such a site. In the simple case of a zero field experiment this is given by

$$P_z(t) = \sum_i p_i \times \frac{1}{3} + \frac{2}{3}\cos(\gamma_\mu B_i t)\exp\left[\frac{-(\Delta_N t)^2}{2}\right], \tag{5.10}$$

where p_i is the probability of occupying a site, B_i is the field magnitude there and Δ_N is a phenomenological term which smears out the signal. The smearing can be understood as arising mainly from dipolar interactions between the muon and nuclear moments in the

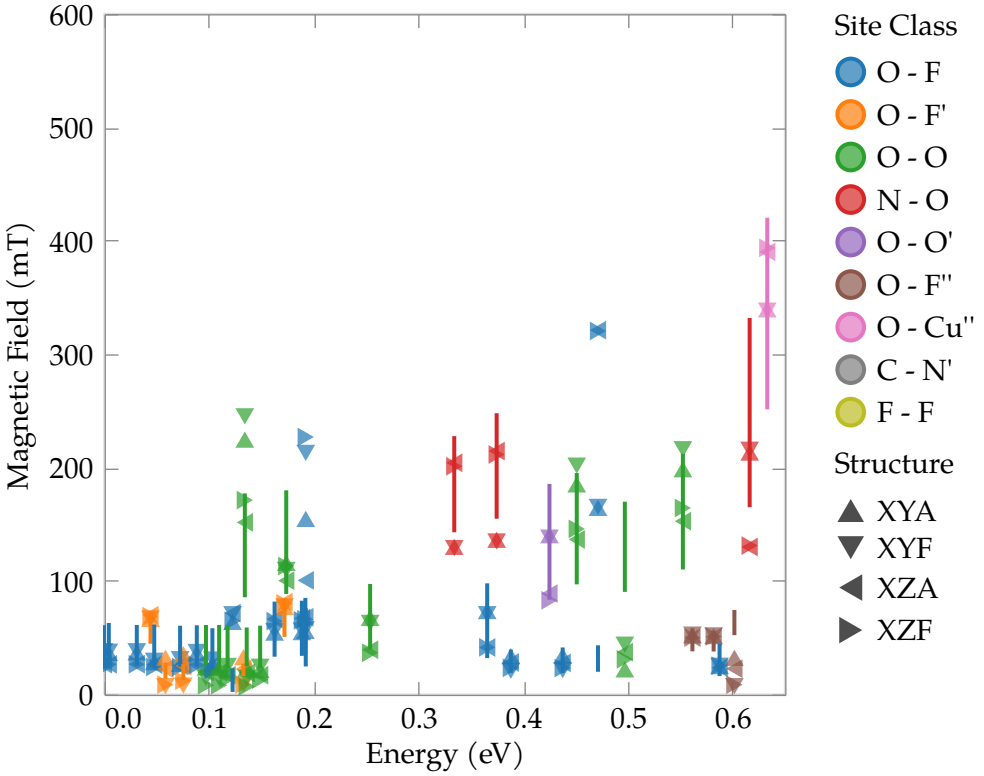

Figure 5.13 Minimal and maximal fields in the helical structure distribution (line) compared to static values for the commensurate structures (triangles) for a subset of sites with $E < 0.6\,\mathrm{eV}$.

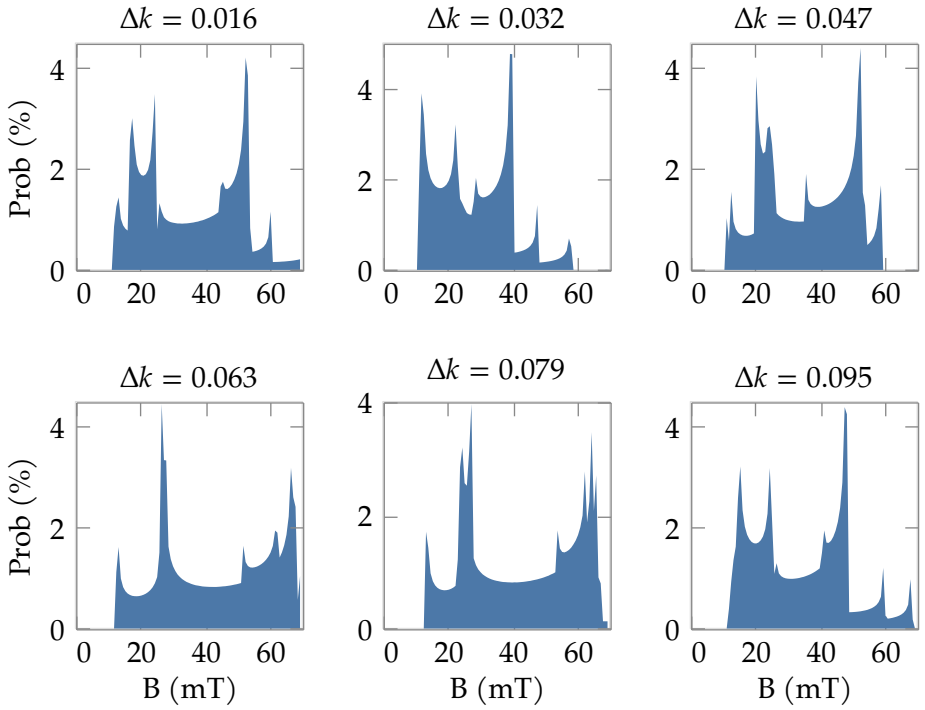

Figure 5.14 The dependence of $k = k_0 + \Delta k$ for the O−F sites with $E < 0.2\,\mathrm{eV}$.

structure and will be approximated using a Van Vleck sum [105]. To better visualise the

resulting polarisation signals we consider the field-dependent polarisation spectrum by taking the Fourier transform of $P(t)$ and using the fact that $f = \gamma_\mu B/2\pi$. Since the signal is a linear combination of all the static field polarisations in the sample, the relative amplitude of the frequency components will be approximately proportional to the magnetic field distribution over all the muon sites.

For the commensurate magnetic structure we have no information about the magnetic field at the muon sites realised experimentally unlike in the NPM compound because no phase transition to an ordered magnetic structure was observed at low temperatures in ZF μ^+SR measurements. We therefore assume an equal probability for each of the calculated sites. Since the initial positions were randomly distributed in the unit cell the calculated sites can be taken to be independent samples from the distribution of possible muon sites, with the caveat that higher energy sites are less likely to be realised - which we model by considering only sites below a certain cutoff energy E_c. This assumption is supported by the fact that low-energy sites are more common and we expect that sites in the O − F bond will dominate.

An example of the spectrum averaged over all the muon sites can be found in **Figure 5.15**. The different structures produce fairly similar results, which is to be expected as they only differ by the direction of a few spins, but the smearing parameter Δ_N has a large effect on the amount of detail visible, and so the results of any comparison with experimental data. The value used was chosen on the basis of the Van Vleck sum for the second moment of the field distribution due to dipole contributions from nuclear moments in a polycrystalline sample [12], given by

$$\Delta_N = \sqrt{\frac{4}{15}\left(\frac{\mu_0}{4\pi}\right)^2 \hbar^2 (\gamma_\mu)^2 \left[\sum_i \frac{(\gamma_i)^2 I_i(I_i+1)}{(r_i)^6}\right]} = 0.271\,\text{MHz}\,, \tag{5.11}$$

where the summation is performed over a large super-cell of the copper ($I_{Cu} = 3/2$ and $\gamma_{Cu} = 70.965{\times}10^6$ rad/T·s) and fluorine ions ($I_F = 1/2$ and $\gamma_F = 251.803{\times}10^6$ rad/T·s), each a distance r_i from the site. Since we also have a large number of possible sites with different muon positions, we average the resulting value of Δ_N over the lowest energy sites ($E < 0.05\,\text{eV}$), although the values for the different sites are very similar - dropping to 0.196 MHz when $E < 1\,\text{eV}$. We suspect that our calculation of Δ_N is overestimating

the experimental value, since the moments are not truly randomised, some degree of entanglement is expected between the nuclear moments.

A similar calculation of the averaged zero-field spectra for the helical incommensurate structure can also be performed, although we must now average over both the magnetic field values at each site (see **Figure 5.12**) and the different muon sites, which are still assumed to be equiprobable. The results are shown in **Figure 5.16**, which also contains a comparison with the XYF magnetic structure, which it resembles when $\Delta k = 0$.

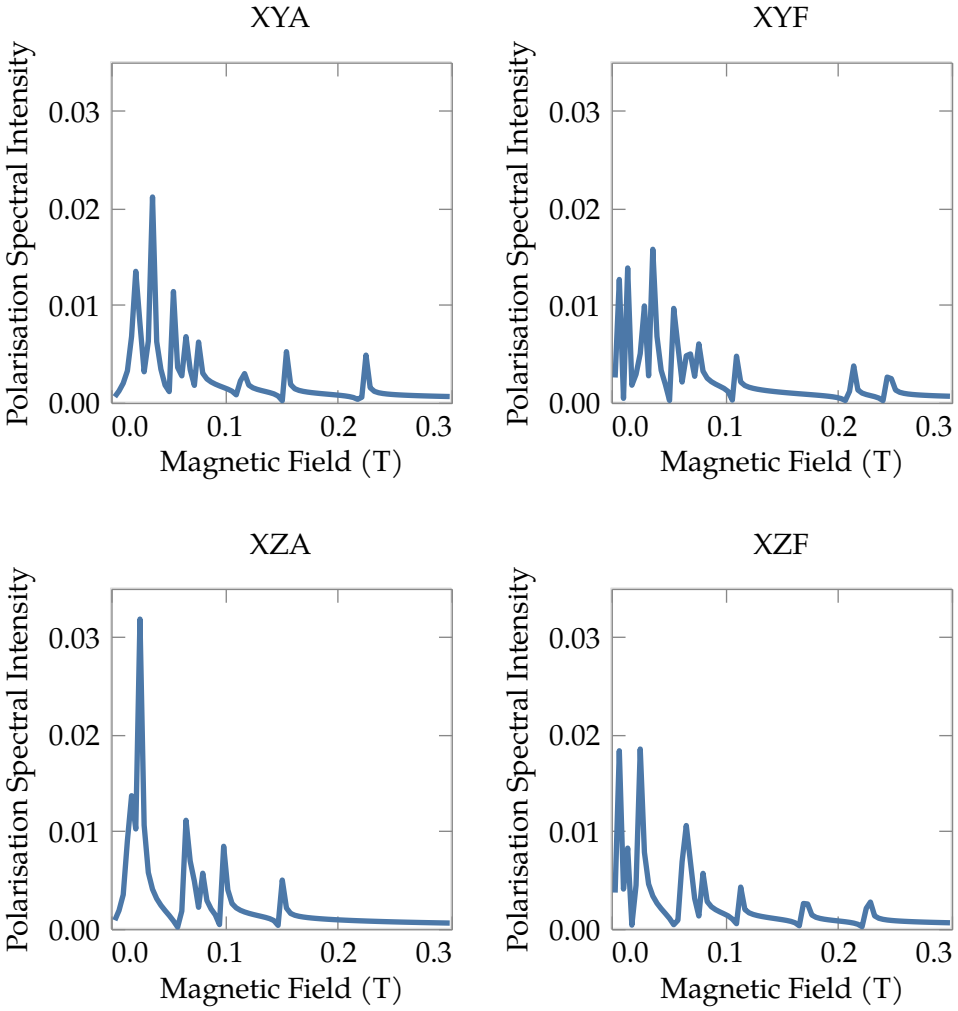

Figure 5.15 Averaged zero-field spectra for different commensurate magnetic structures with $E < 0.2\,\text{eV}$.

To simulate the TF μ^+SR experimental results we need to calculate the polarisation in the non-zero field case for a polycrystalline sample in the transverse field geometry, which we can do by evaluating an integral over the surface of a sphere. We start with

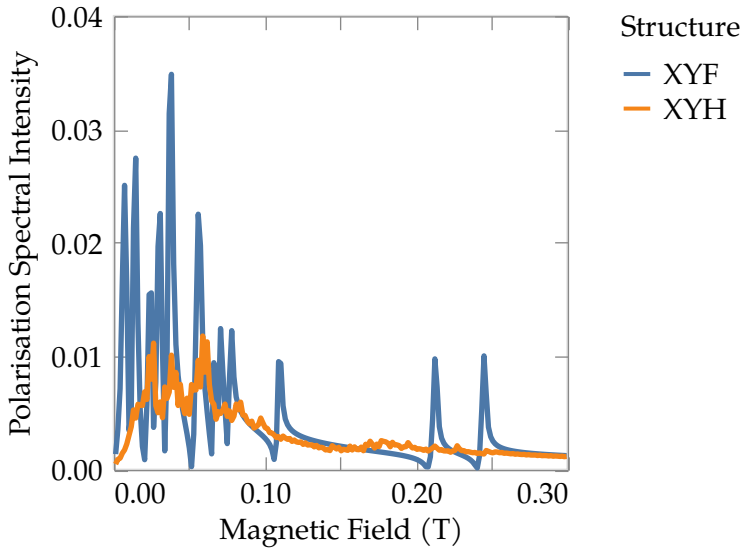

Figure 5.16 Comparison of spectra for commensurate and helical magnetic structure, averaged over all muon sites with $E < 0.2\,\mathrm{eV}$.

an expression for the time evolution of a single muon spin subject to a magnetic field $\mathbf{B}$, obtained by solving the Larmor equation [102], of the form

$$P_z^S(\mathbf{B}, t) = \left(\frac{\mathbf{B}\cdot\hat{\mathbf{z}}}{\|\mathbf{B}\|}\right)^2 + \left[1 - \left(\frac{\mathbf{B}\cdot\hat{\mathbf{z}}}{\|\mathbf{B}\|}\right)^2\right]\cos(\gamma_\mu \|\mathbf{B}\| t)\,, \tag{5.12}$$

where we apply the external field along the x-axis and measure along the z-axis. The field at each site is then given by $\mathbf{B}_i = \mathbf{B}_{\text{ext}} + \mathbf{b}_i$, where the $\{\mathbf{b}_i\}$ are internal site fields each observed with probability p_i and $1 \leq i \leq N_B$. Note that only the internal field contributes to the numerator ($\mathbf{B}_i \cdot \hat{\mathbf{z}} = \mathbf{b}_i \cdot \hat{\mathbf{z}}$). Since the sample is polycrystalline, we consider only the magnitudes of the internal fields $b_i = \|\mathbf{b}_i\|$ and must integrate over all possible orientations with respect to the measurement axis, giving

$$P_z(t) = \sum_i \left(\frac{p_i}{4\pi}\right)\left[\int_{\mathbb{S}^2} P_z^S(b_i, \hat{\mathbf{r}}, t)\, d\Omega\right], \tag{5.13}$$

where we integrate over the unit sphere to ensure that all possible directions of the internal field are considered[6], so that we have $d\Omega = \sin\theta\, d\theta\, d\phi$ in spherical coordinates. We also define the radial unit vector to each point on the surface of the sphere as $\hat{\mathbf{r}} \in \mathbb{S}^2 = \{\mathbf{x} \in \mathbb{R}^3 : \|\mathbf{x}\| = 1\}$. The integral can then be approximated using the Lebedev quadrature

[6] The denominator is explained by the fact that we have $\int d\Omega = 4\pi$.

rule [106], where we sum the values of the integral at a finite set of points $\{\hat{\mathbf{r}}_j\} \subset \mathbb{S}^2$ with weights w_j and $1 \leq j \leq N_D$. This means that our expression for the polarisation becomes

$$P_z(t) = \sum_{i=1}^{N_B} \sum_{j=1}^{N_D} \left(\frac{p_i w_j}{4\pi} \right) P_z^S(b_i, \hat{\mathbf{r}}_i, t) \, . \tag{5.14}$$

We can then substitute our expression for the single muon polarisation P_z^S and include a Gaussian envelope term to obtain our final expression

$$P_z(t) = \sum_{i=1}^{N_B} \sum_{j=1}^{N_D} \left(\frac{p_i w_j}{4\pi} \right) \left[\left(\frac{f_{ij}}{F_{ij}} \right)^2 + \left[1 - \left(\frac{f_{ij}}{F_{ij}} \right)^2 \right] \cos(\gamma_\mu F_{ij} t) \right] \exp\left[\frac{(\Delta_N)^2 t^2}{2} \right], \tag{5.15}$$

where $f_{ij} = b_i(\hat{\mathbf{r}}_j \cdot \hat{\mathbf{z}})$ and $F_{ij} = \left\| B_{\text{ext}} \hat{\mathbf{x}} + b_i \hat{\mathbf{r}}_j \right\| = \sqrt{B_{\text{ext}}^2 + b_i^2 + 2 B_{\text{ext}} b_i (\hat{\mathbf{r}} \cdot \hat{\mathbf{x}})}$. To compare more easily with the experimental measurements, we can finally take the Fourier transform of our polarisation $P_z(t)$ to obtain a field distribution using $\omega = \gamma_\mu B$, giving a spectra with a single well-defined peak as expected.

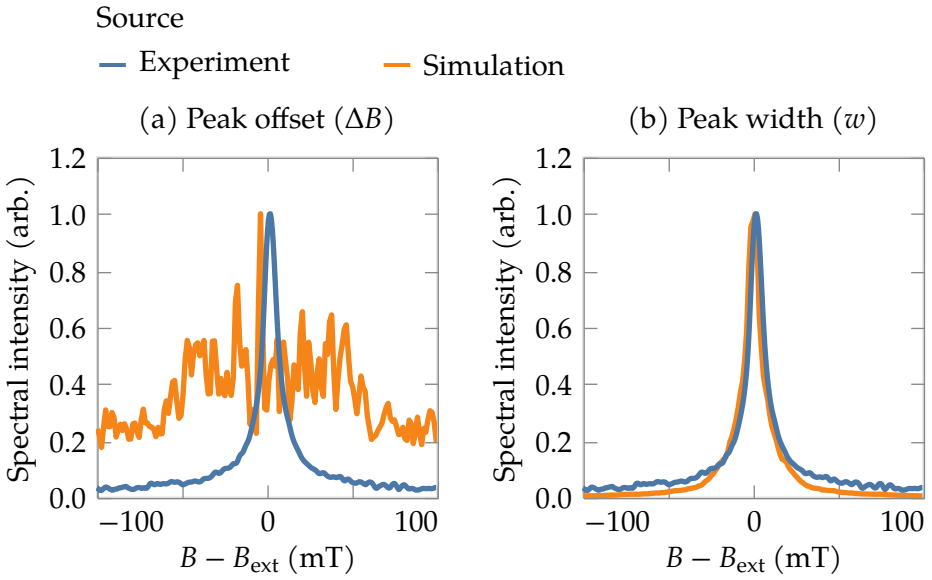

Figure 5.17 Comparison of simulated and experimental spectra at $B = 4\,\text{T}$ when fitting μ_{Cu} to match the (a) peak offset and (b) peak width.

We can then fit the simulation results to a Lorentzian function as described in **Section 5.2.1**, giving two main parameters: the width of the distribution w and its offset from the applied external field $\Delta B = B_0 - B_{\text{ext}}$. An example of a fitted simulated distribution as compared to experimental data can be found in **Figure 5.17**.

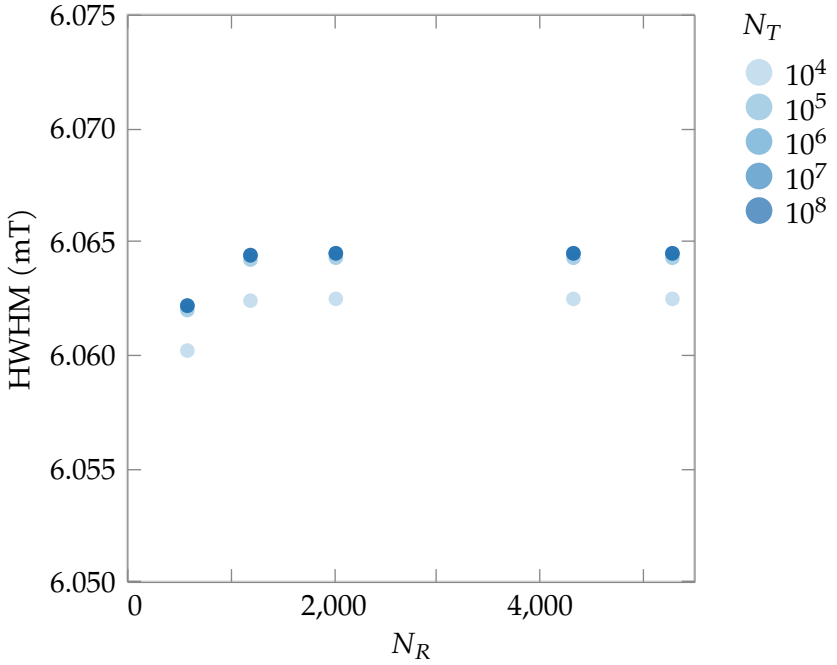

Figure 5.18 Convergence of peak width fitting against the number of timesteps (N_T) and directions considered (N_D) for $B = 4\,\mathrm{T}$.

In the simulation of the spectra we are left with a small set of parameters: the smearing parameter Δ_N which was approximated from the atomic structure by a Van Vleck sum but is expected to be lower experimentally, the cut-off energy E_c below which we consider candidate muon sites to be realised, the degree of canting Δk in the case where the system adopts an incommensurate XYH magnetic structure below the transition and most important of all the magnitude of the copper magnetic moments in the structure μ_Cu. For a bare copper atom the magnetic moment is $1.0\,\mu_\mathrm{B}$, but we expect spin chain fluctuations to reduce it greatly - which is one of the reasons why muons are well suited to investigate systems of this type.

We proceed by considering μ_Cu as dependent on the applied external field B_ext and extract its value by fitting its value to experimental data by matching the width of the Lorentzian peak w (see **Figure 5.19**). We also considered fitting to the other parameter of the Lorentzian in the form of the offset from the applied field ΔB, as shown in **Figure 5.20**, but found that this produced very unrealistic values of the width and magnetic moment. The fact that when fitting to the width the resulting values of the offset are smaller than observed experimentally suggests that this shift is caused by an effect that is not being taken into account, perhaps a macroscopic field like the Lorentz field or the

demagnetising field. The simulations also depend on some computational parameters that had to be converged, namely the number of time-steps ($N_T = 19^7$) and the number of directions to consider when simulating the polycrystalline sample ($N_D = 2030$), where the dependence can be found in **Figure 5.18**.

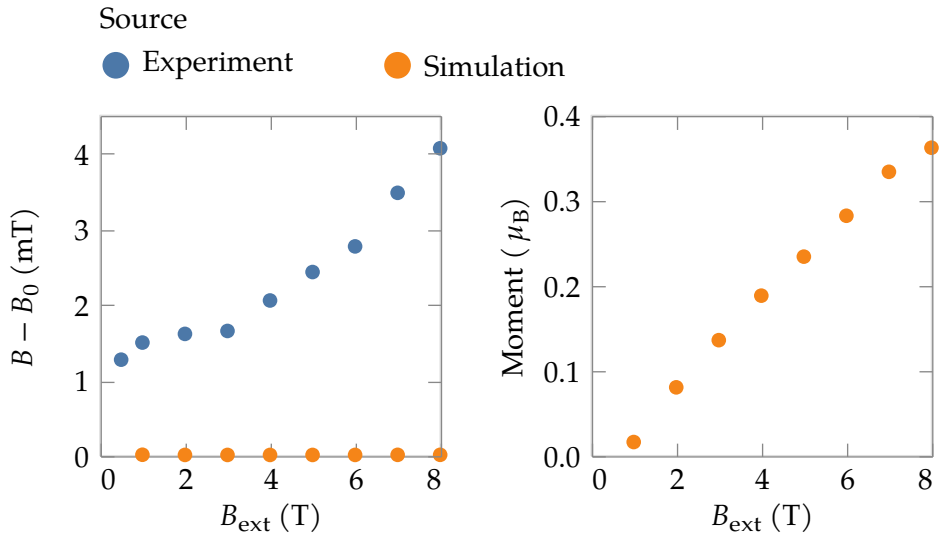

Figure 5.19 Result of fitting simulated TF μ^+SR to experimental peak widths w using $E_c = \infty$ and the XYF magnetic structure, showing a comparison of peak shift ΔB (other parameter) with experiment (left) and fitted value of the copper moment μ_{Cu} (right).

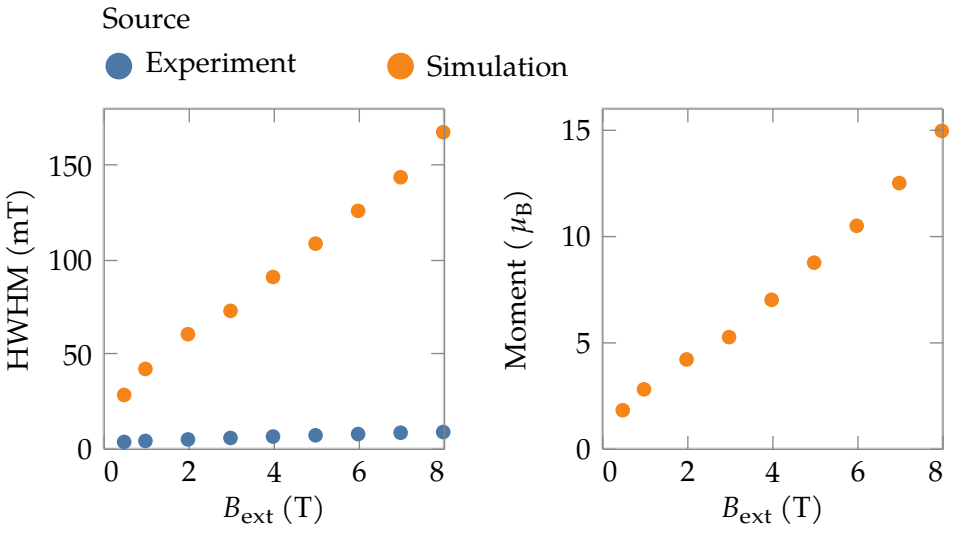

Figure 5.20 Result of unsuccessfully fitting simulated TF μ^+SR to experimental peak shift ΔB using $E_c = \infty$ and the XYF magnetic structure, showing a comparison of peak width w (other parameter) with experiment (left) and unrealistic value of the copper moment μ_{Cu} (right).

We proceed by considering the effect of different magnetic structures and values of the cut-off energy E_c, the results of which can be found in **Figure 5.21**. All the structures produce similar and reasonable values of the copper moments but we observe a difference between the ferromagnetic and antiferromagnetic structures, the latter producing lower values of μ_{Cu} for the higher cut-off energies. The results also imply that if the material adopts the XYF structure as suggested by neutron measurements even a relatively high value of $E_c = 1\,\text{eV}$ is acceptable, since the magnetic moment values increase and then decrease with the cut-off. Realistically, we expect a value of $E_c < 0.1\,\text{eV}$ to be most likely, with a small number of the O−F class of muon sites being realised. Similarly, repeating the calculation for the XYF structure but for increasing values of Δ_N, as shown in **Figure 5.22**, we find that values decrease consistently, with the third panel showing the originally calculated value of Δ_N.

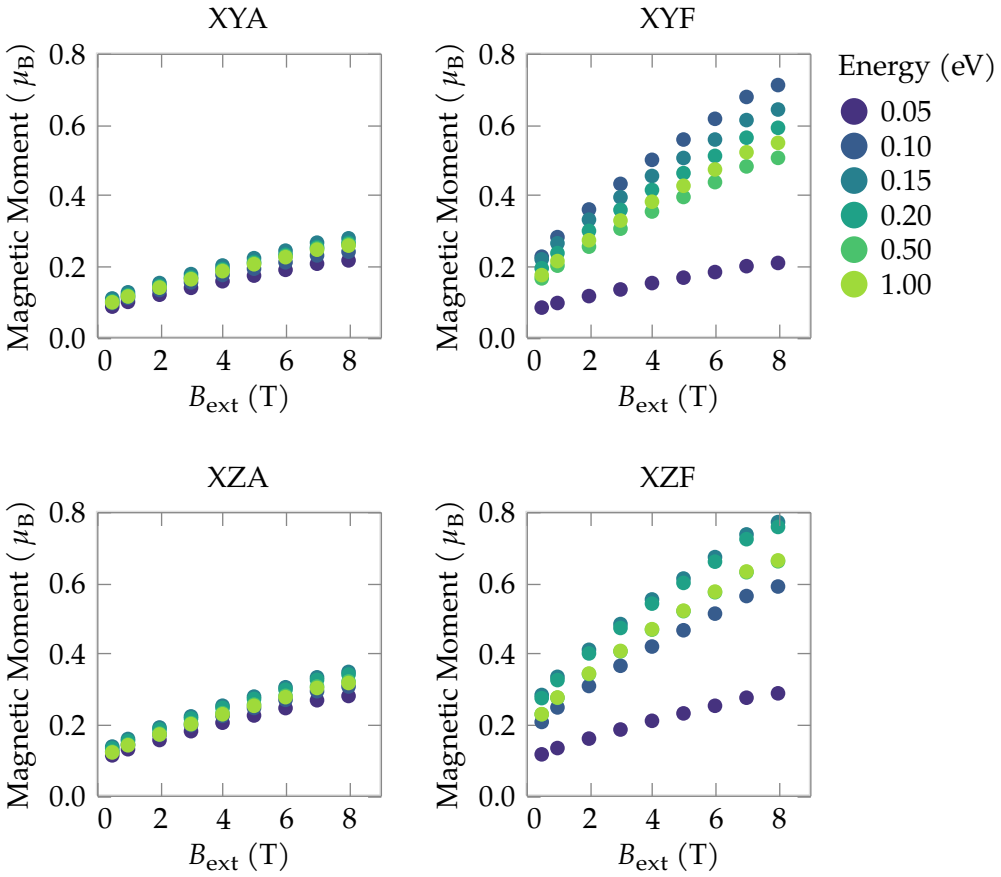

Figure 5.21 Fitted copper magnetic moment as a function of external magnetic field for possible magnetic structures and cut-off site energies E_c.

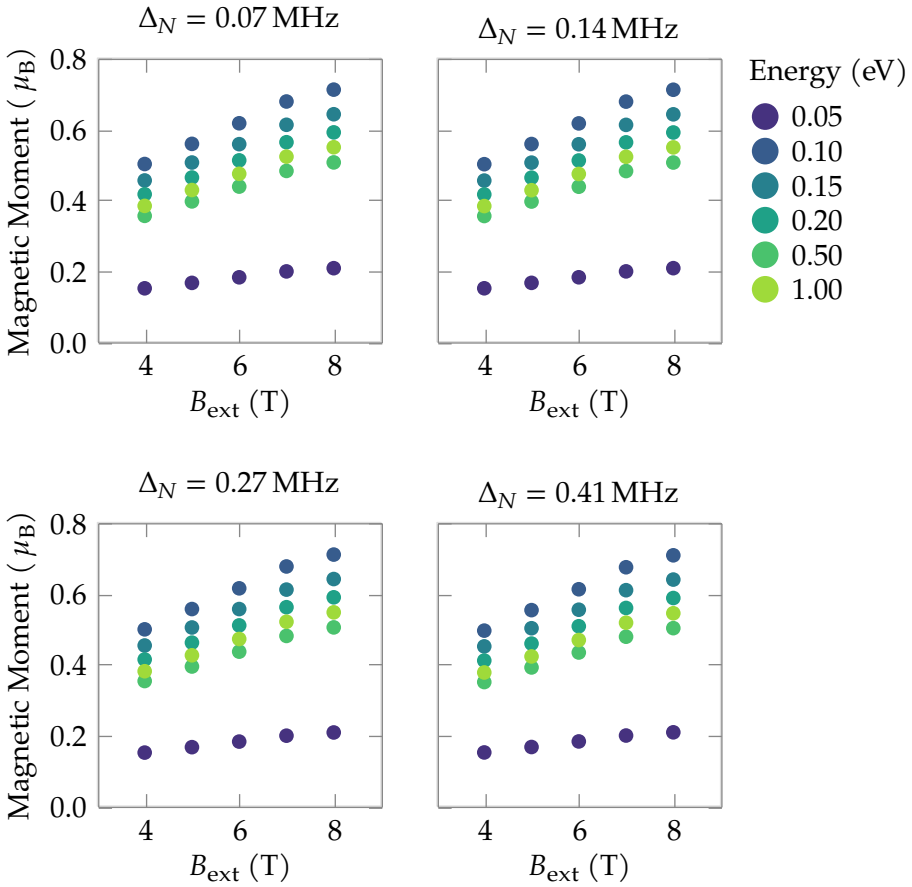

Figure 5.22 Fitted copper magnetic moment as a function of external magnetic field for different values of the nuclear smearing parameter Δ_N and the cut-off site energy E_c.

We also considered the possibility that for $B_{ext} < 3\,T$ the system adopts an incommensurate XYH helical magnetic structure, where the canting angle between spins in the helix is represented by a small change in the propagation vector $(0, 0, k_0 + \Delta k)$ and $k_0 = 4\pi$ corresponds to the XYF commensurate structure. The result of this calculation can be found in **Figure 5.23**, where each panel shows the change in the fitted moment with the propagation vector change Δk for different values of the applied external field. We find that μ_{Cu} is periodic with the helix angle and mostly independent of the energy cutoff E_c, although higher values seem to increase the value slightly.

In conclusion, we can confirm from our TF μ^+SR measurements that the CPM spin chain undergoes a transition at $B_{ext} = 3\,T$ as suspected from magnetometry measurements. To better understand our results we performed a series of DFT calculations and found that the sites most likely to be realised belong to the O−F class, positioned on the other side of the oxygen nuclei where the muon was found in the analogous NPM chain,

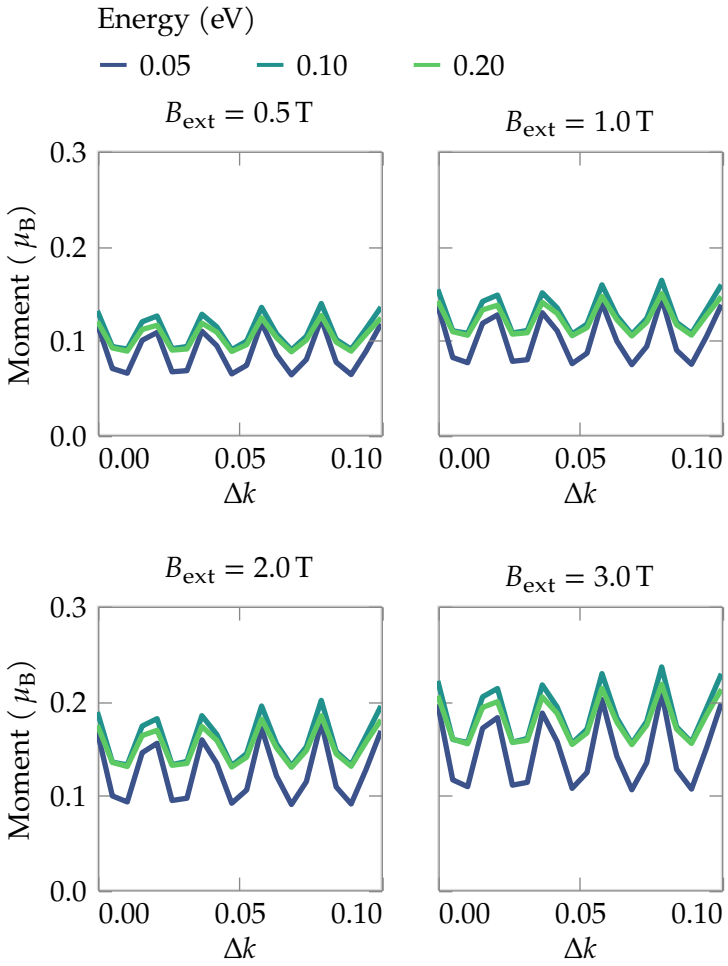

Figure 5.23 Fitted copper magnetic moment as a function of external magnetic field for possible magnetic structures and cut-off site energies E_c.

perhaps attracted by the nearby fluorine atom. We then calculated the dipole magnetic field at each site and used the results to simulate the spectra for the different magnetic structures. The results of this calculation confirm that the proposed XYF magnetic structure, considered most likely from neutron scattering measurements, is consistent with our muon measurements, although we were unable to discount any of the other proposed structures.

In our simulations we also fit the peak width from the experimental data by assuming a field dependent copper magnetic moment, giving a reasonable value ranging from 0.1 μ_B to 0.5 μ_B depending on the value of the site energy cutoff E_c, which limits the calculation to the lower energy sites. From similar materials and the results obtained for the NPM chain we expect that only the low energy O−F are experimentally realised, which requires a value of $E_c = 0.1$ eV, although increasing the value to $E_c = 1$ eV does not change

the results significantly. Although fitting of the experimental data to the XYF structure provided values for μ_{Cu} below the transition we expect that the disorder observed with ZF μ^+SR persists at least in part up to 3 T, when the system adopts the commensurate XYF magnetic structure. We also considered the possibility that an incommensurate helical magnetic structure representing a small helical perturbation from the XYF structure occurs below the transition and our simulations don't rule out this possibility, but since we observe a single transition a disordered low-field phase is more likely.

5.3 Further Work

A series of ZF and TF μ^+SR measurements were performed on the novel chiral spin chain materials NPM and CPM respectively. For the nickel chain magnetic order was observed below $T_N = 1.82 \pm 0.02$ K and the two muon site magnetic fields extracted from the ZF spectra were used to identify the most likely muon sites and confirm the canted AFM magnetic structure suggested by neutron scattering measurements, giving an estimate of the Ni moment magnitude and canting angle. Similarly, we found evidence of a phase transition under external applied field in the CPM compound at $B_{ext} = 3$ T in the TF measurements and used simulations of the results spectra to confirm that the suggested ordered magnetic structure is compatible with our results, giving a field dependent value of the copper magnetic moment. Possible avenues of further work include a more accurate calculation of the magnetic field at a given muon site for both NPM and CPM, since using only the dominant dipole field term did not reproduce the phase transition in the CPM simulations, and the development of a more efficient method of simulating the TF polarisation spectra for any polycrystalline sample as described in **Appendix B** which would make this type of analysis and fitting easier.

Chapter 6

Quantum tunnelling between muon sites in methylated benzene crystals

This chapter presents some work to simulate the behaviour of muons in crystalline benzene and its methylated analogues (which will collectively be referred to as MB crystals, even if benzene itself is not methylated), with a focus on possible quantum tunnelling between the different sites. This has long been known to be a considerable contribution to the movement of muons between sites at low temperatures in some systems [107,108] and attempts have been made to simulate the process with *ab initio* approaches [7,59,109]. These simulations can then be used to better understand the results of μ^+SR experiments and increase the amount of information that can be extracted from them.

An issue with simulating muon quantum tunnelling in benzene (C_6H_6) is that the problem is under-constrained, there are many possible sites with similar energies and so many possible transitions. We instead start by considering methylated benzene crystals, where we add methyl groups (CH_3) around the ring (see **Figure 6.1**). This change will increase the distance between the benzene rings (see **Table 6.1**)and disallow some muon sites (on the carbon atoms in the ring where the methyl group was added), and so possible transitions, simplifying the problem [110–112].

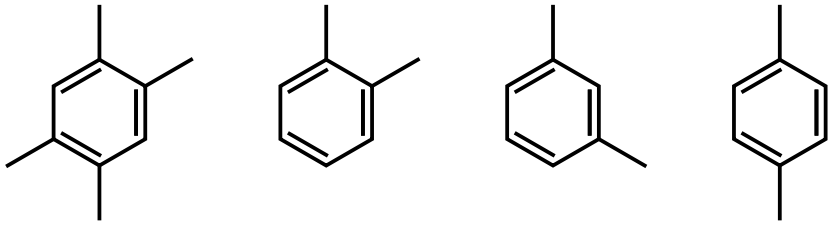

(a) durene (b) o-xylene (c) m-xylene (d) p-xylene

Figure 6.1 Diagrams showing the positioning of the CH_3 groups in the MB compounds.

Benzene crystallises into a solid below 279 K, adopting an orthorhombic configuration with space group *Pbca* known as Phase I which is known to persist down temperatures of 4 K where $a = 7.35$ Å, $b = 9.36$ Å and $c = 6.69$ Å [113]. Each unit cell contains four

benzene molecules oriented at an angle of approximately 45° to the a and c-axis. When considering tunnelling between sites, if we focus on a single ring we have groups of four parallel rings with different orientations and at increasing distances, as can be seen in **Figure 6.2**. We would expect direct transitions from the central ring to another only for $N = 1$ or 2, since the distance to further benzene molecules is too large.

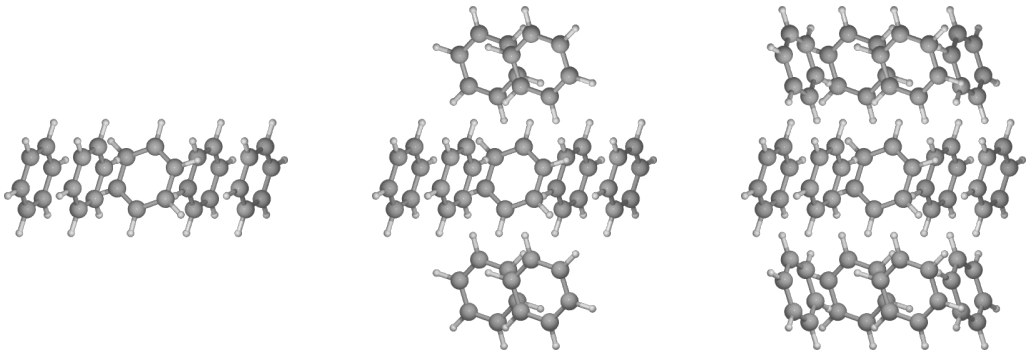

(a) $N = 1$ (b) $N = 2$ (c) $N = 3$

Figure 6.2 Diagram showing the arrangement of the benzene rings in a crystal, with an increasing number of nearest neighbours included around the central ring which is facing the observer.

Name	Group	a (Å)	b (Å)	c (Å)	β (°)	V (Å^3)	d_{min} (Å)
benzene	Pbca	7.35	9.36	6.69	90.0	460.80	1.66
durene	$P2_1/c$	11.51	5.58	6.82	112.89	403.26	2.63
m-xylene	Pbca	10.16	7.46	16.88	90.0	1279.72	1.66
o-xylene	$P2_1/a$	12.51	6.07	8.81	108.68	634.36	1.82
p-xylene	$P2_1/n$	5.73	4.95	11.14	90.0	310.52	1.60

Table 6.1 The crystal space group and unit cell parameters for the different methylated benzene compounds, as well as the minimum site distance d_{min} which greatly influences the degree of quantum tunnelling.

The work in this chapter is based on simulations performed by myself at the University of Durham. The low-temperature ALC spectra for the different MB crystals used to evaluate the accuracy of the simulations were measured and analysed by Francis Pratt and collaborators working at the ISIS Neutron and Muon Source, which is part of the Rutherford Appleton Laboratory (RAL). The initial files describing the atomic structure of the MB compounds used in the DFT simulations were provided by Leandro Liborio working at the Scientific Computing Department also associated with RAL.

6.1 Simulation of muon sites

We start by calculating the muon sites in the different crystalline benzene compounds by performing a series of geometry optimisation calculations using the CASTEP program, as described in **Section 1.3**. Instead of using random initial positions as in other chapters, the muon site candidates were generated by considering all C atoms in the structure with available covalent bonding positions (and so excluding the methyl groups). The possible muon sites were then reduced by considering the symmetries of the crystal and the muon initially positioned to share a carbon atom with a proton. The two particles were placed with an angle of 100° between them and a distance of 1 Å from the carbon atom. Additionally, we identified all other sites that a muon could tunnel to, with a distance limit of 4 Å, to be used in the quantum tunnelling calculation discussed in **Section 6.2**. A summary of the DFT parameters for the geometry optimisation calculations for the different systems can be found in **Table 6.2**. In general, we found that for all the MB crystals, the muons were already approximately positioned at the muon sites and so the structure changed very little with the geometry optimisation.

Quantity	System				
	benzene	durene	m-xylene	o-xylene	p-xylene
Number of sites	21	3	21	19	11
Energy cut-off (eV)	700.00	700.00	700.00	700.00	700.00
MP k-point grid	4 × 3 × 4	2 × 5 × 3	3 × 4 × 2	1 × 3 × 1	3 × 6 × 3
Cell volume (Å^3)	491.68	821.39	1279.71	634.36	621.05
$\|\Delta\mathbf{R}\|_{\max}$ (Å)	5.77	6.72	7.48	6.62	7.35
$\|\mathbf{F}\|_{\max}$ (Å/eV)	7.91	7.65	6.18	7.86	7.93
$\Delta E/N_{\text{ion}}$ (eV)	2.84	3.56	1.45	3.05	2.59

Table 6.2 Parameters of DFT muon site calculations for different methylated benzene crystals.

6.2 Simulation of quantum tunnelling

In theory, the method described in **Section 6.3** can be used to simulate the ALC spectra for the different methylated benzene crystals by calculating the hyperfine interaction experienced at each muon site. Each site gives a set of resonances in the polarisation as the applied field is varied, so that the different contributions can be averaged to obtain the

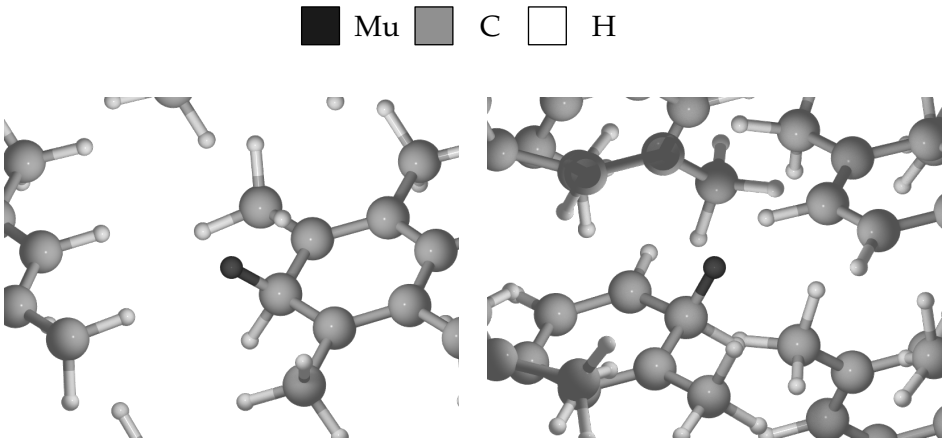

(a) durene (b) m-xylene

Figure 6.3 Examples of muon sites in methylated benzene compounds

full spectra. The main complication with this method is that the quantum nature of the muon is not taken into account. A range of different quantum effects are possible, but in this chapter we will focus on the case of quantum delocalisation between classical sites, which happens when the muon ZPE is comparable to the barrier energy between sites. The simple approach that we used to investigate this effect was to estimate the transition rate k between sites and average the hyperfine tensors at two sites when the value was greater than a cutoff k_c, under the assumption that the muon would constantly tunnel between the sites during the experimental measurement.

To estimate the transition rate between sites we make use of the Wentzel-Kramers-Brillouin (WKB) method, which gives a semi-classical approximate solution to the 1D time-independent Schrödinger equation by assuming that the wavefunction is a complex exponential with a slowly varying amplitude and phase (i.e. $\psi(x) = \exp(iS(x)/\hbar)$ where S is a complex function). This means that we need to first approximate the 1D potential barrier between the sites and the ZPE of the muon at each site, which was calculated using a phonon DFT calculation and the method described in **Section 1.3.1.1**.

6.2.1 Simulation of the energy barrier

We start by making the simplifying assumption that the transition of a muon between two sites in the crystal can be described by a 1D potential $V(x)$ parameterised by a reaction

coordinate that interpolates between the sites. In practical terms, this means that we use the transition state search (TSS) method (see **Section 1.2.5.3**) as implemented in CASTEP to calculate the energy barrier between all pairs of sites. For simplicity the linear synchronous transit (LST) method, where atom positions are linearly interpolated between the two configurations, was used. The method then performs a series of energy calculations along this path to locate the maximum barrier height and determine the general shape of the potential.

A complication that arises when performing these calculations is that the two structures being interpolated are the result of a previous geometry optimisation with subtly different atomic positions. We therefore need to match the atoms in the two unit cells whilst minimising the total pairwise distance, a task known as the linear sum assignment problem. We define a $N \times N$ cost matrix C_{ij} containing the distance between atoms i and j in the two structures whilst taking periodic boundary conditions into account. The distance between atoms of different species is infinite by definition, since they can't be assigned to each other. Our task is then to find a Boolean matrix $X_{ij} \in \{0, 1\}$ where a given entry is non-zero only when atoms i and j are assigned to each other, so that the minimal total distance is then given by

$$\min\left(\sum_i \sum_j C_{ij} X_{ij}\right). \tag{6.1}$$

An implementation of the algorithm described by Crouse [114] was used to obtain this optimal assignment and so successfully calculate the potential barriers between sites.

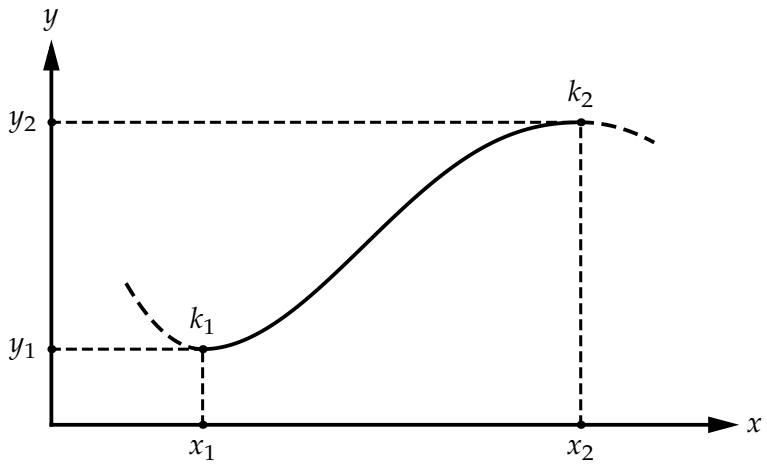

Figure 6.4 Part of piecewise potential well interpolation showing single quintic polynomial.

Since we also need to perform a phonon calculation to estimate the ZPE at each site, we can improve our estimate of the potential by using piecewise polynomial interpolation, allowing us to also account for the shape of the potential minima around the muon sites. We proceed by splitting the barrier at its extrema (minima and maxima), which in this case always gives a double well with four intervals: two quadratic sections at the endpoints representing the walls and two quintic polynomials between them and the barrier maxima. We construct the quintic intermediate sections $f(x)$ by using Hermite interpolation, which allows us to specify the value of the function and its first two derivatives at the endpoints $f(x_i) = y_i$, $f'(x_i) = 0$ and $f''(x_i) = k_i$ as shown in **Figure 6.4**.

This means that to construct our potential we need to calculate the second derivatives of the potential at the extrema. For the maximum, we can fit a quadratic function to the intermediate barrier points found during the TSS search for the barrier maximum at $x_{\max}$, limited to $|x - x_{max}| < 0.25$ to exclude points that are close to the muon sites. On the other hand, to approximate the shape of the minimum we can use the result of the phonon calculation at the Γ point, performing a series of single-point energy DFT calculations with the atoms perturbed along the three muon mode eigenvectors. This gives us an idea of the anharmonicity of each minimum and can be used to fit a 3D quadratic polynomial $E(\mathbf{r}_\mu)$ describing the energy as a function of the muon position, which can then be used to calculate the second derivative along the direction between two muon sites. A full description of the procedure used to construct the interpolated barrier can be found in **Appendix C**.

Repeating the procedure described above for all pairs of muon sites maximum distance of $d_{\text{pair}} < 4$ Å we obtain a series of barriers, as shown in **Figure 6.5**. We find a large number of possible site transitions N_{b} and a range of site distances d_{pair} but with very similar shapes. All barriers are nearly symmetric double potential wells, with the two endpoints x_i having very similar energies and a central peak at $x_{\max}$. We find that most barriers have a height $V_{\max} = V(x_{\max})$ between 2–3 eV, but identify a class with a higher $V_{\max} \sim 4$ eV which seems to correspond to the case where the muon crosses the plane of a benzene molecule between two sites.

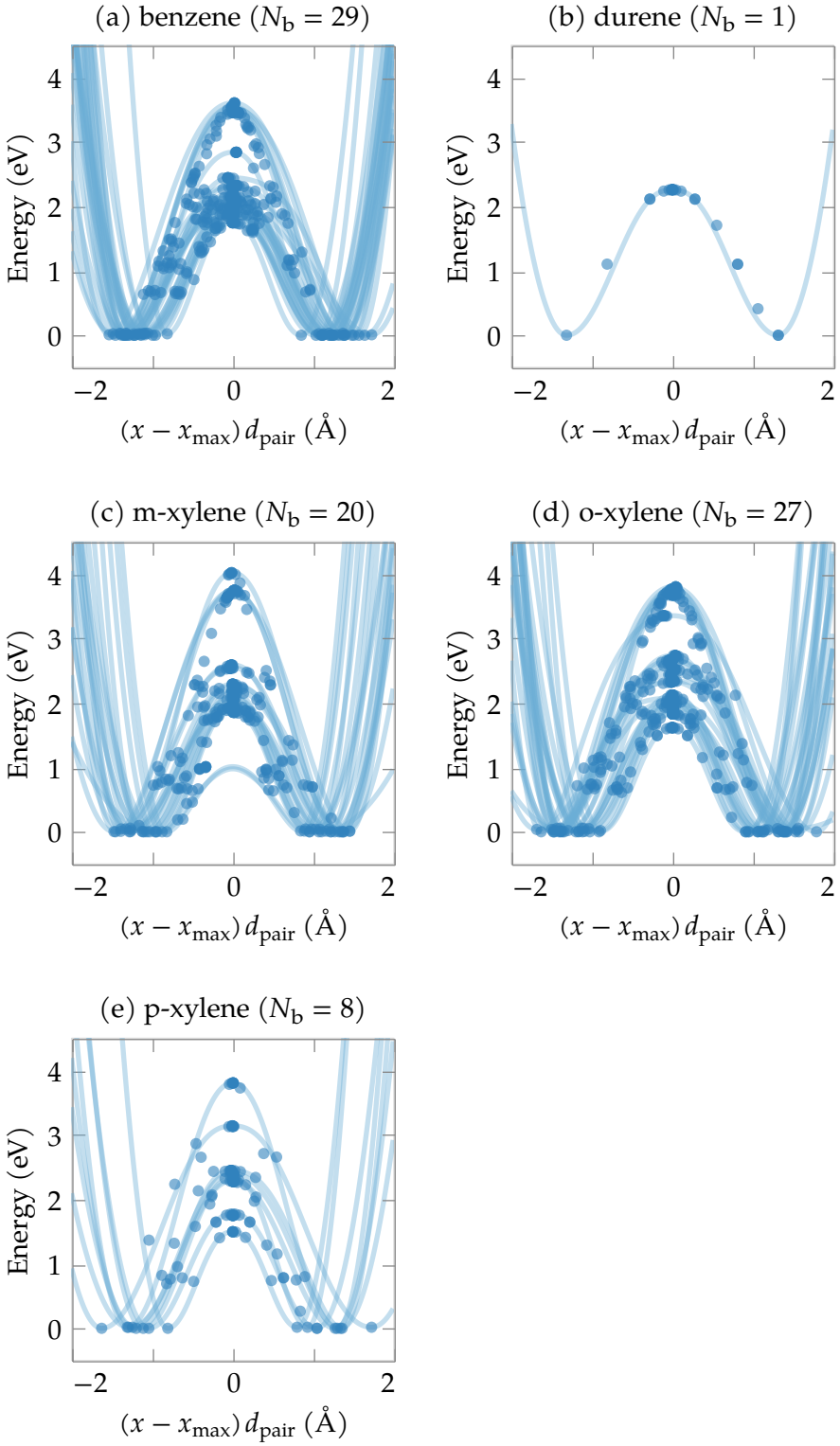

Figure 6.5 Calculated potential barriers for all transitions between muon sites in all methylated benzene crystals centred on the maximum. We indicate the number of barriers N_b calculated in each case and show both the points found during the TSS calculation and the piecewise polynomial fitted to them.

6.2.2 WKB Approximation

A derivation of the WKB approximation and its application to quantum tunnelling through a potential barrier can be found in any undergraduate quantum mechanics textbook (see for example [115]). Unfortunately, in most cases the simplifying assumption of vertical barrier walls is made, since the approximation breaks down when the barrier energy matches that of the particle $E = V$ and the wavefunction no longer varies slowly. This issue can be resolved by using *connection formulas* as explained in **Appendix D** and so the transition probability across a smooth potential barrier $V(x)$ for a particle with energy E is given by

$$T = \frac{\exp(-2\gamma)}{\left[1 - \frac{1}{4}\exp(-2\gamma)\right]^2} \quad \text{where} \quad \gamma = \sqrt{\frac{2m}{\hbar^2}} \int_{\tilde{x}_1}^{\tilde{x}_2} \sqrt{V(x) - E}\, dx\,. \tag{6.2}$$

Note that we integrate between the classical turning points $x_1 < \tilde{x}_1 < \tilde{x}_2 < x_2$ which occur when $V(\tilde{x}_i) = E$, meaning that the potential energy matches the total energy. This means that the muon transition rate between sites is approximately

$$k = \left(\frac{E}{2\pi\hbar}\right) \times T\,, \tag{6.3}$$

which can be understood as the particle attempting to tunnel with frequency $f = E/(2\pi\hbar)$ and succeeding with probability T, by analogy with Gamow's theory of alpha decay [116]. For our calculations, we assumed that the muon at each site before a transition has energy obtained using the harmonic approximation by averaging the frequencies of the three muon phonon modes as described in **Section 1.3.1.1**.

Performing this calculation for the possible site transitions from the previous section, we obtain a range of rate values, shown as a function of the barrier distance d_{pair} and height V_{max} in **Figure 6.6**. A logarithmic scale was used on the y-axis to show the expected approximately linear dependence, since $T \approx e^{-2\gamma}$ when the barrier is high and wide (i.e. $\gamma \gg 1$). The same information is also presented in a different manner in **Figure 6.7**, which shows the correlation between the barrier width and height whilst representing the transition rate using the size of the points. In this representation, we can more clearly see the transitions with high barriers $3\,\text{eV} < V_{\text{max}} < 4\,\text{eV}$ identified in the previous section

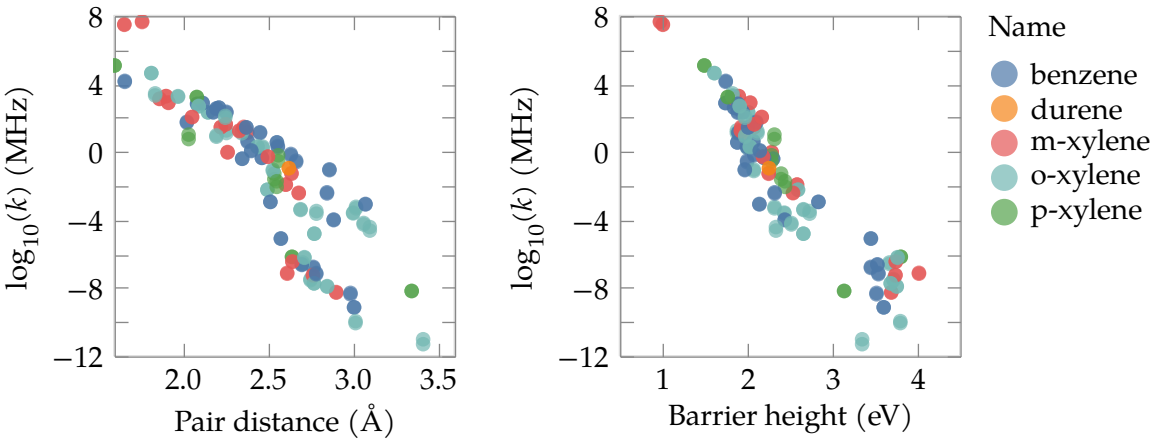

Figure 6.6 Calculated transition rate k between muon sites in different MB compounds on a logarithmic scale as a function of the two main barrier parameters, its width and height.

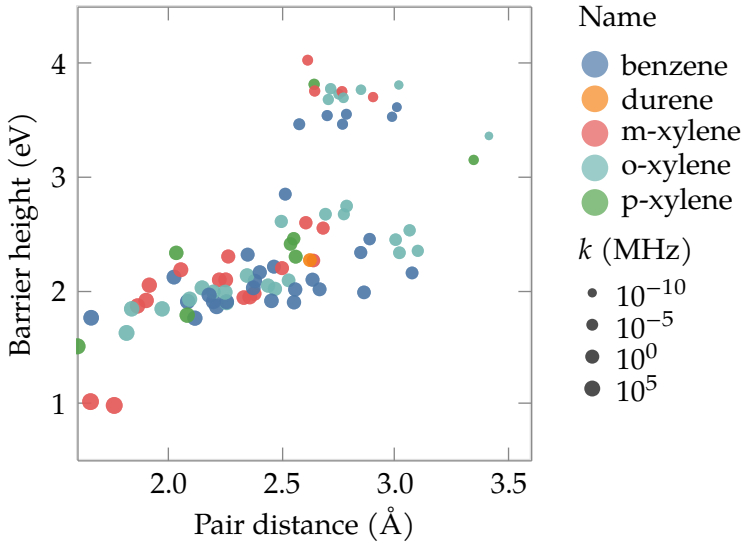

Figure 6.7 Correlation between barrier height and width for the possible muon site transition in different MB compounds, with the size of the point indicating the corresponding transition rate (on a logarithmic scale).

as involving crossing the plane of a benzene molecule which appear as smaller points in the top-right of the plot.

6.3 Simulation of ALC spectra

Given the muon sites we can simulate the ALC spectra that would be observed experimentally using the method described in **Section 1.1.5**, calculating the resonance peak for each site in the isolated system containing an electron, the muon and the hydrogen atom

sharing the carbon atom in the benzene ring with it, giving a Hamiltonian containing Hyperfine and Zeeman terms:

$$\begin{aligned}\hat{H} = & \sum_{ij} \left(A_\mu\right)_{ij} \left(\hat{S}_e\right)_i \left(\hat{S}_\mu\right)_i + \left(A_H\right)_{ij} \left(\hat{S}_e\right)_i \left(\hat{S}_H\right)_j \\ & + \sum_i \hbar \Big[\gamma_\mu \left(\hat{S}_\mu\right)_i + \gamma_e \left(\hat{S}_e\right)_i + \gamma_H \left(\hat{S}_H\right)_i \Big] B_i \,, \end{aligned} \tag{6.4}$$

where we have constructed the spin operators $\left(\hat{S}_\alpha\right)_i$ to act on the combined system by using the Kronecker product and identity matrices for each component $\alpha = \mu, e, H$ and direction $i = x, y, z$. We also have the hyperfine tensor $(A_\alpha)_{ij}$ between the electron and the other particles, the gyromagnetic ratio for each particle γ_α and the applied external magnetic field B_i.

The hyperfine tensors A_{ij} can be calculated at each classical muon site from the electronic structure as implemented in CASTEP [117], with the same DFT parameters as when calculating the site positions (see **Table 6.2**). The resulting 3×3 matrix can be described using three parameters A_{iso}, D_1 and D_2 which are related to the eigenvalues $|A_1| < |A_2| < |A_3|$ and three orthonormal eigenvectors $\mathbf{a}$, $\mathbf{b}$ and $\mathbf{c}$ by

$$A = \left(A_{\text{iso}} + D_1\right)(\mathbf{a} \otimes \mathbf{a}) + \left(A_{\text{iso}} - \frac{D_1 - D_2}{2}\right)(\mathbf{b} \otimes \mathbf{b}) + \left(A_{\text{iso}} - \frac{D_1 + D_2}{2}\right)(\mathbf{c} \otimes \mathbf{c}) \,,$$

$$\text{where} \quad \begin{cases} A_{\text{iso}} = \frac{1}{3}\left(A_1 + A_2 + A_3\right) \\ D_1 = A_3 - A_{\text{iso}} \\ D_2 = A_2 - A_1 \,. \end{cases} \tag{6.5}$$

One complication that arises in the calculation of the hyperfine tensor is that due to its low mass, the effect of the muon zero-point motion around the classical position can't in general be disregarded [118]. This problem can be mitigated by multiplying the hyperfine parameters (A_{iso}, D_1, D_2) by quantum correction factors calculated by averaging over the finite spread of the muon wavefunction. In this chapter, the factors were chosen by hand to match the experimental results ($A^{\text{F}}_{\text{iso}} = 1.15$, $D^{\text{F}}_1 = 1.1$, $D^{\text{F}}_2 = 1.0$), but values can also be calculated from first principles. One common method of doing this, first presented by Möller, Ceresoli *et al.* [119], is similar to the procedure used to evaluate the shape of the potential around the muon site minima (see **Section 6.2**). We identify the three phonon modes which correspond to the muon, which are well separated from

the rest due to the difference in mass, and then compute the hyperfine tensor with the atoms displaced along each of the vibration eigenvectors. The result is then a weighted average of the calculated tensors using the muon wavefunction, which we get by either using the harmonic approximation, giving the ground state of a Harmonic oscillator with the phonon frequency, or solving the Schrödinger equation directly for greater accuracy, especially when the muon site is anharmonic.

The ALC spectra can then be simulated for the different MB compounds using the `quantumtools` [120] library, which computes the average polarisation for different applied magnetic fields by direct diagonalisation of the Hamiltonian in **Equation 6.4**. To account for the effect of quantum tunnelling we introduce a cutoff transition rate k_c above which two sites are considered to be connected and then use the rate calculated in **Section 6.2** to construct a graph with sites as nodes and edges between pairs that have a transition rate over this threshold. We can then obtain the connected components of the graph using a simple algorithm [56] as groups of sites whose hyperfine tensors we average and treat as a single site. This means that a value of $k_c = 0$ will average all sites that could be connected into a single one whilst a value of $k_c = \infty$ will treat each site individually without any tunnelling. In general, we find that a lower value of k_c, and so a greater degree of tunnelling, decreases the number of distinct resonances in the spectra and narrows the remaining ones.

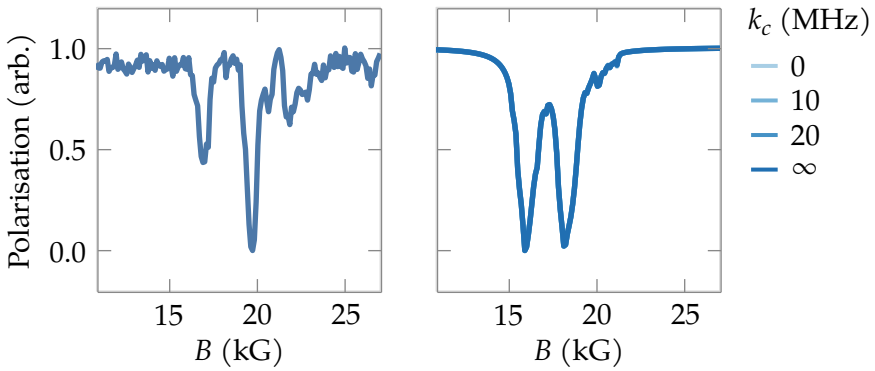

Figure 6.8 Normalised ALC spectra for durene (left) measured experimentally at 4 K and (right) simulated with quantum tunnelling for different values of the rate cutoff k_c, which in this case all give the same values.

We find that the simplest spectra are those of durene (see **Figure 6.8**), where there is clear agreement with experiment with two strong resonances. Since we have only two sym-

metry inequivalent sites, we can explain why the relative amplitudes of the resonances don't match the experimental measurement by concluding that the sites are not occupied with equal probability but with a ratio of approximately 2 : 1. We also find that in this case the different values of k_c produce the same spectra (which are superimposed) and we find no evidence of quantum tunnelling. This is not unexpected since durene is the crystal with the lowest number of sites and greatest minimum distance between them due to the 4 methyl groups around the benzene rings (see **Figure 6.1a**). A combination of these factors means that there is only a single pair where a transition can happen (see **Figure 6.5b**) but the sites have similar hyperfine tensors due to being related by a crystal symmetry, so that even $k_c = 0$ leaves the spectra unchanged.

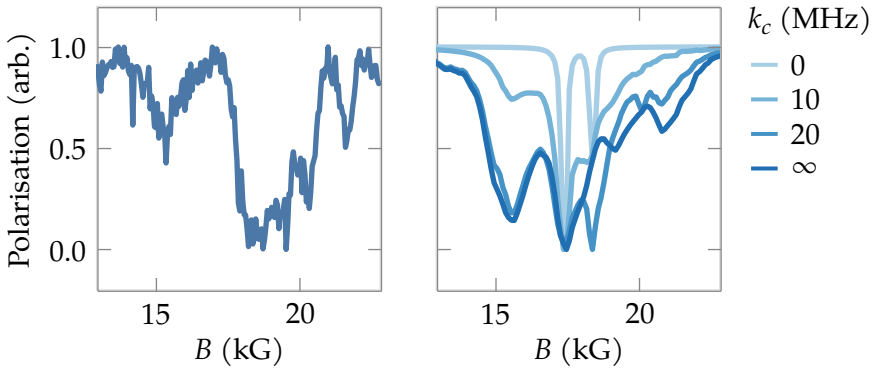

Figure 6.9 Normalised ALC spectra for o-xylene (left) measured experimentally at 10 K and (right) simulated with quantum tunnelling for different values of the rate cutoff k_c.

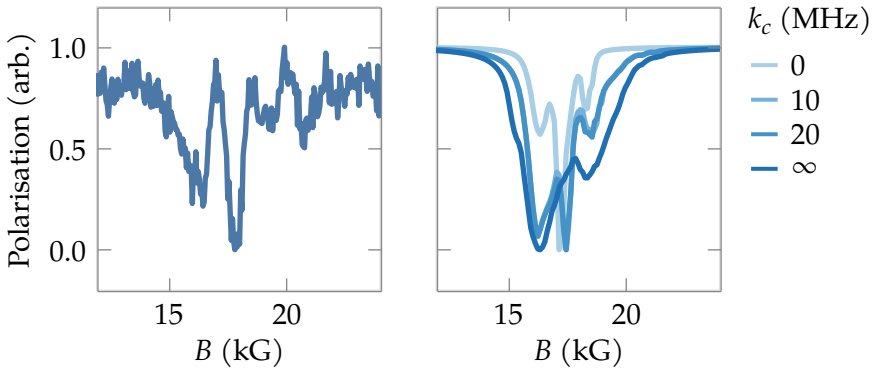

Figure 6.10 Normalised ALC spectra for m-xylene (left) measured experimentally at 10 K and (right) simulated with quantum tunnelling for different values of the rate cutoff k_c.

Similarly, for the cases of o-xylene (see **Figure 6.9**) and m-xylene (see **Figure 6.10**) we obtain some agreement between experiment and simulation, whilst also showing the effect of quantum tunnelling on the spectra. In both cases we find that increasing the value of

k_c broadens the resonances, which is to be expected since the spectra are then caused by a larger number of independent sites instead of a smaller number of tunnelling sites with averaged hyperfine tensors. By comparing with the experimental measurements, we can clearly see that not all possible transitions are happening ($k_c \neq 0$) but find evidence that our calculations improve the accuracy of the simulated spectra over the case without tunnelling, since some peaks are missing from that spectra ($k_c = \infty$). In the case of o-xylene a slightly smaller experimental resonance at $B = 20\,\text{kG}$ to the right of the main one disappears and in m-xylene the two main resonances between 15 kG and 20 kG are averaged into a single one for $k_c > 20\,\text{MHz}$.

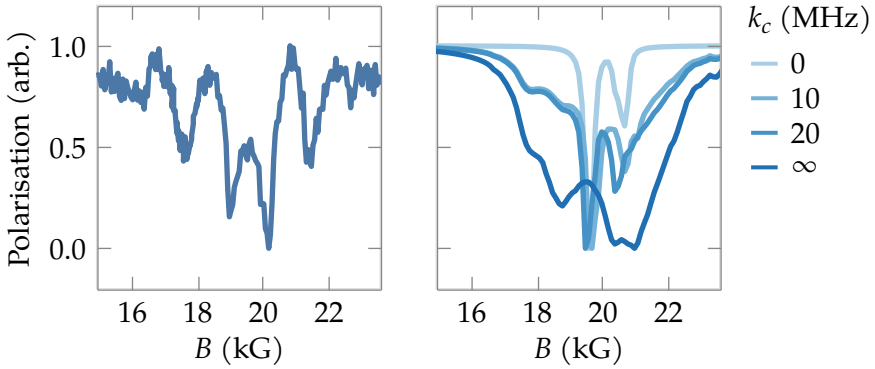

Figure 6.11 Normalised ALC spectra for benzene (left) measured experimentally at 5 K and (right) simulated with quantum tunnelling for different values of the rate cutoff k_c.

Finally, the most complicated spectra to simulate is that of benzene, which can be found in **Figure 6.11**, where the lack of methyl groups around the benzene rings means that a large number of muon sites are available and that the distance between the rings is smaller. We therefore expect quantum effects to be more noticeable in this case, with a greater number of tunnelling transitions possible between sites and a more pronounced quantum correction. From the four large resonances found in the experimental spectra, our simulation seems to reproduce the two central ones in the range 18–20 kG as seen more clearly with $k_c = 20\,\text{MHz}$. The fact that their relative amplitude is reversed also indicates that our assumption that all muon sites are occupied equally doesn't hold in this case as well. We don't see the two smaller resonances that appear experimentally at 17 kG and 21 kG except for slight features in the simulated spectra. We suspect that a more accurate calculation of the quantum correction factors to the hyperfine tensors used would improve the agreement with experiment and plan to do so in the future.

In conclusion, by comparing with experimental results we have shown that accounting for quantum tunnelling between muon sites increases the accuracy of the simulation of the avoided-level crossing spectra for different methylated benzene crystals, better matching the resonance widths and preserving some peaks that disappear when no tunnelling is considered. The simulation was performed by using a combination of different first-principles DFT calculations to approximate the potential barrier between pairs of sites and then estimating the transition rate using a semi-classical expression derived by the WKB method. Those rates were then used to simulate the ALC spectra for the different compounds with various degrees of quantum tunnelling. We found that considering transitions with a rate greater than $k_c = 10$–$20\,\mathrm{MHz}$ provided greater agreement than both the case without tunnelling ($k_c = \infty$) and where all possible transitions below a certain site distance happen ($k_c = 0$).

Some areas of further work include a more accurate calculation of the potential barrier (using a more sophisticated TSS method than LST, with some alternatives discussed in **Section 1.2.5.3**) and the transition rate, perhaps using a density matrix approach [121] or adopting the techniques used to simulate proton tunnelling [122]. The accuracy of the simulated ALC spectra results could be improved by a calculation of the hyperfine quantum correction factors from DFT [119] and the relative occupancies of the muon sites estimated by fitting to experimental data. Related to this last possibility and applicable to other systems, combining this type of simulation with fitting to experimental results will probably require faster simulations of ALC spectra, which proved a bottleneck in our calculations, either by optimising existing routines or by a more efficient numerical algorithm which takes advantage of the structure of the Hamiltonian to be solved.

Chapter 7

Conclusions and further work

This thesis aims to demonstrate the importance of knowing the location of the muon sites and their environment when analysing the results of a μ^+SR experiment, enhancing our understanding of the materials under investigation and their interaction with the muon.

In **Chapter 2** we consider the molecular honeycomb lattice $Cu(pym)_{1.5}(H_2O)(BF_4)_2$ where the use of DFT calculations places the most likely low-energy sites close to oxygen and fluorine atoms surrounding the complex structure. This will prove to be a common feature of more than one molecular system containing O and F considered in this thesis. The muons were also able to detect an incommensurate magnetic ground state below the phase transition, despite the small magnetic moments present in the material.

We also find that DFT calculations suggest that the position of the muon sites realised experimentally might change when a material undergoes a structural transition. This happens both with the hysteretic molecular magnet 4-(2-benzimidazolyl)-1,2,3,5-dithiadiazolyl (HbimDTDA) in **Chapter 3**, which displays magnetic switching behaviour when the structure changes with temperature, and in the Mott insulator Sr_2IrO_4 (SIO) described in **Chapter 4**, where the structure can be altered considerably with the application on an external electrical current. In the first case we have a large number of possible sites with similar energies in the structure, a common feature in molecular systems, and find that two new sites become available in the high-temperature phase, most likely due to the changes in the structure and bonding between molecules in the material. In the case of the SIO material, we find that the application of an external electric current, which alters both the structure and magnetism of the material, leads to a change in the relative energies of the two classes of sites identified. In the ZF μ^+SR measurements with the applied current we also saw a splitting in the muon site fields, which we explained using a calculation of the dipole magnetic field at each site as caused by an additional FM *c*-axis component in the magnetic structure.

We used a combination of μ^+SR measurements and DFT calculations to investigate a pair of analogous spin chains $[Ni(pym)(H_2O)_4]SO_4$ and $[Cu(pym)(H_2O)_4]SiF_6 \cdot H_2O$

(pym = pyrimidine) with $S = 1$ and $S = 1/2$ respectively in **Chapter 5**. In the first case, a magnetic ordering transition was observed at low temperature and zero-field with evidence of two muon site frequencies in the measurements. By combining this information with the calculated sites and simulations of the magnetic field at each one from the different possible magnetic structures we confirmed that the canted AFM arrangement suggested by neutron scattering measurements was consistent with our results and obtained a value for the nickel magnetic moment. Similarly, for the copper chain which remains disordered at the lowest temperatures, we found evidence of phase transition with applied field using TF μ^+SR measurements and confirmed that our results are consistent with an ordered magnetic structure above the transition. The most likely muon sites realised were determined for each case based on the DFT energy of each site and comparison with experimental data, giving similar results as expected from analogous structures and proving essential in the simulation of the magnetic field and polarisation spectra which followed.

Finally, in **Chapter 6** we considered the case of quantum tunnelling between sites in a series of methylated benzene structures. A new method was developed using DFT calculations and the WKB approximation to estimate the transition rate between muon sites in the material and the results used to simulate the ALC spectra expected from the materials, showing that a greater degree of tunnelling decreased the number of resonances and made the remaining ones narrower. The results were then compared with experimental measurements, confirming that the addition of quantum tunnelling improves the accuracy of our simulated spectra when compared to the case where all sites remain independent, with a better agreement in peak width and the appearance of some resonances which were not visible without tunnelling.

A common theme in this thesis has been to combine knowledge of the muon sites with other simulations to allow for direct comparison with μ^+SR experimental results. In some systems dipole magnetic fields were calculated at the muon sites to distinguish between different candidate magnetic structures but another useful technique, especially in the last two chapters, has been the direct calculations of muon polarisation spectra, reproducing the results of both TF and ALC μ^+SR measurements. A fundamental part of these simulations was an efficient method of simulating the polarisation, which also

opened up the possibility of fitting against experimental data to calculate properties like the magnetic moment as demonstrated in **Chapter 5**. In this first case, a more performant method was proposed and partially implemented as discussed in **Appendix B**. Similarly, the simulation of ALC muon spectra could be optimised in the future since the current method relies on solving directly diagonalising the Hamiltonian for each value of the applied magnetic field. Each of these matrices is related by a linearly-varying Zeeman term (i.e. $\hat{H}(B) = \hat{H}_0 + B\Delta\hat{H}$) meaning that a more efficient method taking advantage of this structure might exist.

In some systems we also observed an important shortcoming of the DFT+μ method: although the energy of the geometry-optimised structure is usually a good indicator of which muon sites are most likely to be realised we find that experimental results indicate that this is not always the case. We sometimes find that non-minimal energy sites are occupied instead or that multiple sites are realised with different probabilities[7]. A solution to this problem is not clear, but it might be possible to combine ion implantation calculations [124] to classically approximate the thermalisation of the high-energy implanted muon with more accurate molecular dynamics calculations [125] to simulate the stopping process and so estimate the stopping cross-section for each muon site, giving more accurate results.

As part of the work on improving calculations on the quantum behaviour of muons in crystalline systems[8], we also performed some computational experiments to extend the CASTEP DFT code employed throughout this thesis by treating the muon as a quantum object on the same level as the electrons. This required a series of modifications to the internals of the `FORTRAN` program so that it would solve a pair of Schrödinger equations describing the coupled electron and muon system

$$\left[-\frac{\nabla^2}{2} - \sum_n \frac{Z_n}{(\mathbf{r}-\mathbf{R}_n)} + \int \frac{\rho_\mathrm{e}(\mathbf{r}')}{(\mathbf{r}-\mathbf{r}')} d\mathbf{r}' - \int \frac{\rho_\mu(\mathbf{r}')}{(\mathbf{r}-\mathbf{r}')} d\mathbf{r}' - V_\mathrm{xc}\left[\rho_e, \rho_\mu\right](\mathbf{r})\right] \psi_i(\mathbf{r}) = \epsilon_i \psi_i(\mathbf{r}) \tag{7.1}$$

[7] A famous example of this is in semiconductors like silicon, where the metastable states with energy higher than the ground state are realised [12,123].

[8] DFT calculations with a quantum muon are usually performed using the expensive path-integral molecular dynamics (PIMD) method [59] or Nuclear-Electronic orbitals method [126] which is more useful in non-crystalline molecular systems that don't use plane wave basis sets.

$$\left[-\frac{\nabla^2}{2m_\mu}+\sum_n \frac{Z_n}{(\mathbf{r}-\mathbf{R}_n)}-\int \frac{\rho_e(\mathbf{r}')}{(\mathbf{r}-\mathbf{r}')}d\mathbf{r}'+V_{xc}[\rho_e,\rho_\mu](\mathbf{r})\right]\chi(\mathbf{r})=\lambda\chi(\mathbf{r}), \qquad (7.2)$$

where we add the second to last term in **Equation 7.1** to represent the potential from the muon charge density and change our exchange-correlation functional to account for the new quantum particle in the system. In the muon part of the equations, we must account for its different mass $m_\mu = 206m_e$ but don't need a Hartree term for the electrostatic repulsion between muons because there is only a single one in the system. This is the same reason why as a first approximation we can use the same XC functional as in normal DFT calculations, since there is no exchange between muons and the correlation is expected to be small. A possible method of correcting the error in this approximation might be to use a reduced muon mass to tune the quantum behaviour of the muon.

The changes made to CASTEP for this extension can be divided into two parts: an option was added to the function calculating the kinetic energy to adjust the particle mass being used (which simply scales the term) and modifications were made to the function calculating the local potential acting on the particles so that the new terms were included. For simplicity, in our initial implementation, another option was added to distinguish between the electronic and muon calculations and the common terms transferred the two by writing and reading from a pair of files. To solve the ground state of the combined system, an external script was used to perform a small number of SCF iterations on each part and the two calculations restarted with updated potentials from the new charge densities until the results were consistent. Although the implementation is still incomplete, we managed to obtain some initial results with a Si_8 unit cell, as seen in **Figure 7.1**, where we see that the muon charge density is mostly localised at the centre of the unit cell and the iso-surfaces are approximately spherical.

In conclusion, DFT+μ can be an important part of analysing muon experiments some issues persist. Determining the degree to which the muon behaves like a quantum particle in a particular system is sometimes essential and an area of open research. As part of the work for this thesis, the MuFinder program designed to simplify the running of muon site calculations was extended to calculate a series of metrics which make use of DFT phonon calculations to estimate how prevalent muon quantum effects are expected to be in a given system, as discussed in **Section 1.3.1**. Similarly, the extension to DFT to

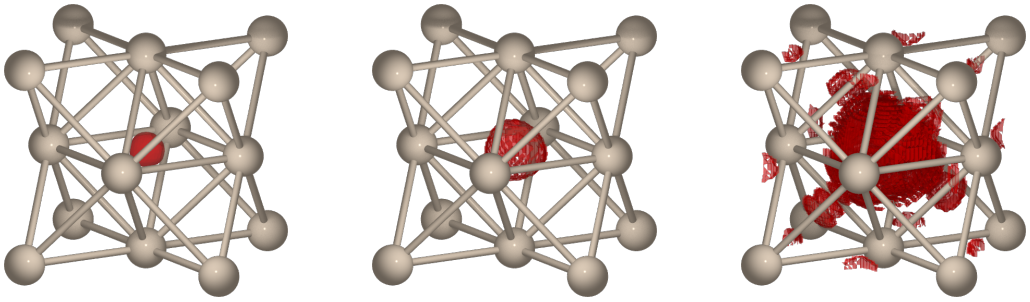

(a) $f = 1 - 10^{-1}$ (b) $f = 1 - 10^{-3}$ (c) $f = 1 - 10^{-5}$

Figure 7.1 Example quantum muon calculation in Si crystal, showing volume containing different fractions f of the total muon charge density.

account for a muon wavefunction discussed in the previous section is still in its infancy but might provide a fruitful avenue of research, providing a method of estimating the quantum behaviour of the muon which balances accuracy and performance.

Appendix A
Bloch's theorem

Following the derivation in Ashcroft and Mermin [127], we start with the fact that the system is periodic by any real space lattice vector $\mathbf{R} = n_i \mathbf{a}_i$, where $\mathbf{a}_i$ are the lattice vectors which define the parallelepiped of the unit cell. This means that we can define a translation operator $\hat{T}_{\mathbf{R}} f(\mathbf{r}) = f(\mathbf{r} + \mathbf{R})$ which will always commute both all other translations ($\hat{T}_{\mathbf{R}} \hat{T}_{\mathbf{R}'} \psi(\mathbf{r}) = \hat{T}_{\mathbf{R}'} \hat{T}_{\mathbf{R}} \psi(\mathbf{r}) = \psi(\mathbf{r} + \mathbf{R} + \mathbf{R}')$) and with the Hamiltonian ($\hat{T}_{\mathbf{R}} \hat{H} \psi = H(\mathbf{r} + \mathbf{R})\, \psi(\mathbf{r} + \mathbf{R}) = H(\mathbf{r})\, \psi(\mathbf{r} + \mathbf{R}) = \hat{H} \hat{T}_{\mathbf{R}} \psi$ since $H(\mathbf{r} + \mathbf{R}) = H(\mathbf{r})$). This means that the eigenstates of the Hamiltonian can be chosen to be simultaneous eigenstates of all the translation operators ($\hat{H}\psi = \epsilon\psi$ and $\hat{T}_{\mathbf{R}} \psi = c(\mathbf{R})\, \psi$). We can then use the fact that $c(\mathbf{R} + \mathbf{R}') = c(\mathbf{R})\, c(\mathbf{R}')$ and that we can always write $c(\mathbf{a}_i) = \exp(2\pi i x_i)$ to define

$$c(\mathbf{R}) = \exp[i(\mathbf{k} \cdot \mathbf{R})] = \prod_i c(\mathbf{a}_i)^{n_i}, \tag{A.1}$$

where $\mathbf{k} = \sum_i x_i \mathbf{b}_i$ and the $\mathbf{b}_i$ are the reciprocal lattice vectors defined by $\mathbf{a}_i \cdot \mathbf{b}_j = 2\pi\delta_{ij}$. So that we finally have

$$\hat{T}_{\mathbf{R}} \psi = \psi(\mathbf{r} + \mathbf{R}) = c(\mathbf{R})\, \psi(\mathbf{r}) = \exp[i(\mathbf{k} \cdot \mathbf{R})]\, \psi(\mathbf{r})\ . \tag{A.2}$$

This means that by separating the wavefunction into $\psi(\mathbf{r}) = e^{i\mathbf{k}\cdot\mathbf{r}} u(\mathbf{r})$ we find that $u(\mathbf{r})$ also had the periodicity of the lattice

$$\begin{aligned} u(\mathbf{r} + \mathbf{R}) &= \exp(-i[\mathbf{k} \cdot (\mathbf{r} + \mathbf{R})])\, \psi(\mathbf{r} + \mathbf{R}) \\ &= \exp(-i[\mathbf{k} \cdot (\mathbf{r} + \mathbf{R})]) \exp[i(\mathbf{k} \cdot \mathbf{R})]\, \psi(\mathbf{r}) \\ &\quad u(\mathbf{r})\ . \end{aligned} \tag{A.3}$$

Under the assumption that the specific boundary conditions that we impose will not affect the physical properties, we assume Born-Von Karman boundary conditions where the crystal is finite with N_i primitive cells along $\mathbf{a}_i$ and the wavefunction is also periodic beyond this supercell. We can then obtain a condition on the values of x_i

$$\begin{aligned} \psi(\mathbf{r} + N_i\mathbf{a}_i) = \psi(\mathbf{r}) \rightarrow \exp[iN_i(\mathbf{k}\cdot\mathbf{a}_i)] = 1 \rightarrow \exp(2\pi i N_i x_i) = 1 \\ \rightarrow x_i = \left(\frac{m_i}{N_i}\right) \quad \text{where} \quad m_i \in \mathbb{Z}\,, \end{aligned} \tag{A.4}$$

which in the limit of an infinite crystal $N_i \rightarrow \infty$, becomes $x_i \in [0,1] \subset \mathbb{Q}$.

Appendix B

Polarisation calculation in Fourier space

Although the procedure described in **Section 5.2.4** to simulate the Fourier transform of the polarisation function $P_z(t)$ works as expected, the calculation is computationally expensive, especially since the simulation is then used to fit the magnitude of the magnetic moment. The reason for this is then when evaluating **Equation 5.15** a very high time resolution is required, since this determines the resolution in magnetic field after taking the Fourier transform. A small time step will give us a wide range of values in B-space but most of them will be discarded, since we are only interested in the field values around the applied external field B_{ext} where we observe the peak.

A possible solution to this issue is that instead of evaluating $P_z(t)$ and then computing the Fourier transform $\hat{P}_z(B)$ numerically using the FFT algorithm, we can compute the Fourier transform of the expression analytically and then evaluate only over the desired range in B-space. Taking advantage of the fact that the Fourier transform is linear in its argument[9] we can consider only a single term in the sum, which has the general form

$$G(t) = \cos(at)\exp\left(-bt^2\right)\theta(t),$$

where we have substituted $a = \gamma_\mu F_{ij}$ and $b = \Delta_{\text{N}}^2/2$. We also need to multiply by the Heaviside step function $\theta(t)$ to account for the fact that we only consider $t > 0$ and will be able to set $a = 0$ for terms that don't contain a factor of $\cos(t)$.

The Fourier transform for this function can be evaluated analytically by using the convolution theorem[10] to give

$$\hat{G}(\omega) = \frac{1}{\sqrt{8\pi b}}\left[\sqrt{\pi}\exp\left(\frac{-\omega^2}{4b}\right) + 2iF\left(\frac{\omega}{2\sqrt{b}}\right)\right] * \left[\frac{\delta(\omega - a) + \delta(\omega + a)}{2}\right],$$

where we use $f * g$ to denote the convolution of two functions

[9] That is to say that for $h(x) = af(x) + bg(x)$ we have $\hat{h}(\omega) = a\hat{f}(\omega) + b\hat{g}(\omega)$.

[10] Which states that the Fourier transform of a convolution is a product and vice-versa ($h(x) = f(x)\,g(x) \iff \hat{h}(\omega) = \hat{f}(\omega) * \hat{g}(x)$).

$$(f * g)(t) = \int_{-\infty}^{\infty} f(\tau)\, g(t-\tau)\, d\tau$$

and $F(x)$ is the Dawson integral, which is defined as

$$F(x) = \frac{1}{2}\int_0^{\infty} e^{-t^2/4} \sin(xt)\, dt.$$

So that we can now express $\hat{P}_z(B)$ as a sum of simpler terms

$$\hat{P}_z(B) = \sum_{i=1}^{N_B}\sum_{j=1}^{N_D} \frac{p_i w_j}{4\pi} \times \left\{ \left(\frac{f_{ij}}{F_{ih}}\right)^2 \times 2K(B) + \left[1 - \left(\frac{f_{ij}}{F_{ih}}\right)^2\right] \times \left[K\big(B - F_{ij}\big) + K\big(B + F_{ij}\big)\right] \right\},$$

where we have defined the kernel function $K(x)$ as

$$K(B) = \frac{1}{4\sqrt{\pi}\Delta_{\mathrm{N}}}\left[\sqrt{\pi}\exp\left(\frac{-\gamma_\mu^2 B^2}{2\Delta_{\mathrm{N}}^2}\right) + 2iF\left(\frac{\gamma_\mu B}{2\sqrt{2}\Delta_{\mathrm{N}}}\right)\right].$$

Our algorithm therefore reduces to evaluating the sum u_i of a set of $K(B)$ functions centred at some points y_i at another set of points x_i, which can be expressed as

$$u_i = \sum_{j=1}^{N} K(x_i - y_j) \cdot q_j. \quad i = 1, \ldots, M$$

This is a well-known problem and can be efficiently solved by extending an implementation [128] of the fast Gauss transform (FGT) based on approximating the kernel as a sums-of-exponentials (SOE)

$$K(x) \approx S(x) = \sum_{k=1}^{N_K} w_k e^{-t_k x},$$

where $w_k, t_k \in \mathbb{C}$. The Gaussian part of our kernel is simple to approximate and very efficient expansions exist (see [128]) but the imaginary part containing $F(x)$ is more complicated. The solution that we finally arrived at is to employ the algorithm described in [129] to construct a SOE approximation for a general kernel, which requires a greater number of exponential terms than the Gaussian contributions but gives good results when applied to the Dawson function.

Appendix C

Polynomial interpolation of potential barrier

We want to construct a quintic polynomial $P(x)$ that satisfies a series of conditions, starting with the fact that it has two extrema at points x_1 and x_2, so that we define

$$P'(x) = (x - x_1)\,(x - x_2)\left(ax^2 + bx + c\right) \tag{C.1}$$

which we can then integrate to obtain an expression for $P(x)$, adding a last unknown d for the constant of integration:

$$\begin{aligned} P(x) = \quad & \frac{1}{5}ax^5 + \frac{1}{4}\left[b - a(x_1 + x_2)\right]x^4 + \frac{1}{3}\left[ax_1x^2 - b(x_1 + x_2) + c\right]x^3 \\ & + \frac{1}{2}\left[bx_1x^2 - c(x_1 + x_2)\right]x^2 + cx_1x_2x + d \end{aligned} \tag{C.2}$$

We then impose the condition that the endpoints x_1 and x_2 also have certain values $P(x_i) = y_i$ and second derivatives $P''(x_i) = k_i$, giving a system of linear equations

$$\begin{bmatrix} x_1^3 - x_1^2x_2 & x_1^2 - x_1x_2 & x_1 - x_2 & 0 \\ -x_2^2x_1 + x_2^3 & -x_1x_2 + x_2^2 & -x_1 + x_2 & 0 \\ -\frac{1}{20}x_1^5 + \frac{1}{12}x_1^4x_2 & -\frac{1}{12}x_1^4 + \frac{1}{6}x_1^3x_2 & -\frac{1}{6}x_1^3 + \frac{1}{2}x_1^2x_2 & 1 \\ \frac{1}{12}x_2^4x_1 - \frac{1}{20}x_2^5 & \frac{1}{6}x_2^3x_1 - \frac{1}{12}x_2^4 & \frac{1}{2}x_2^2x_1 - \frac{1}{6}x_2^3 & 1 \end{bmatrix} \begin{bmatrix} a \\ b \\ c \\ d \end{bmatrix} = \begin{bmatrix} k_1 \\ k_2 \\ y_1 \\ y_2 \end{bmatrix}$$

which can be solved symbolically using Cramer's rule to give values for a, b, c and d.

Similarly, to obtain information about the shape of the potential close to the sites, in the form of second derivative values k_i we use the Γ-point phonon calculations performed for each site (whilst taking advantage of the crystal symmetries), which were also used to estimate the muon zero-point energy. Since the muon is much lighter than the other atom in the unit cell, we always find three high-frequency modes (one for each spatial dimension) with very high values for the muon component in their eigenvectors $\mathbf{v}_j$. We can then investigate the anharmonicity of the site minima by performing a series of single-point DFT energy calculations with the atom positions $\mathbf{R}_0$ displaced along the axis defined by the phonon eigenvectors

$$\mathbf{R}_0 + \sum_i q_i \mathbf{v}_i \,, \tag{C.3}$$

where $\mathbf{q} \in Q = \left\{\lambda(i/N)\,\hat{\mathbf{e}}_j \in \mathbb{R}^3 : -N \leq i \leq N \text{ and } 1 \leq j \leq 3\right\}$ and $(\hat{\mathbf{e}}_j)_i = \delta_{ij}$ is the standard basis in $\mathbb{R}^3$. We therefore perform $2N$ calculations over each axis with the scaling parameter λ limiting the maximal displacement of any atom, since the $\mathbf{v}_i$ are normalised.

We can then use the result of these calculations to both confirm the assumption of a harmonic well and to compute the second derivative of the potential in the direction of the muon transfer. We start by performing a multivariate quadratic regression over the calculated energies in terms of the displacements by solving a linear system of equations:

$$E_i = \sum_{|\alpha|<2} c_\alpha (q_i)^\alpha \,, \tag{C.4}$$

giving a linear system of equations of the form

$$\mathbf{E} = X\mathbf{c} + \boldsymbol{\epsilon}$$

$$\begin{bmatrix} E_1 \\ E_2 \\ \vdots \\ E_M \end{bmatrix} = \begin{bmatrix} 1 & Q_{11} & \cdots & Q_{13} & Q_{11}Q_{12} & \cdots & Q_{12}Q_{13} & Q_{11}^2 & \cdots & Q_{13}^2 \\ 1 & Q_{21} & \cdots & Q_{23} & Q_{21}Q_{22} & \cdots & Q_{22}Q_{23} & Q_{21}^2 & \cdots & Q_{23}^2 \\ \vdots & \vdots & \vdots & \vdots & \vdots & \vdots & \vdots & \vdots & \vdots & \vdots \\ 1 & Q_{M1} & \cdots & Q_{M3} & Q_{M1}Q_{M2} & \cdots & Q_{M2}Q_{M3} & Q_{M1}^2 & \cdots & Q_{M3}^2 \end{bmatrix} \begin{bmatrix} c_1 \\ c_2 \\ \vdots \\ c_M \end{bmatrix} + \boldsymbol{\epsilon} \,, \tag{C.5}$$

where we have defined the matrix Q_{ij} by joining the vectors in the set Q as rows and also have an additional vector $\boldsymbol{\epsilon}$ representing the random error. The ordinary least squares estimation of the coefficients $\mathbf{c}$ then is

$$\mathbf{c} = X^\mathsf{T} X^{-1} X^\mathsf{T} \mathbf{E} \,. \tag{C.6}$$

The resulting polynomial $E(\mathbf{q})$ is then adjusted by a coordinate transform $\mathbf{q} = M\mathbf{x} + \mathbf{c}$ so that the result is expressed in terms of the position of the muon in the unit cell $\mathbf{x}$. We can then calculate the shape of the potential in the direction of the transfer by substituting $\mathbf{x} = \hat{\mathbf{v}}t + \mathbf{x}_0$, where $\hat{\mathbf{v}}$ is the unit vector of the displacement between the muon sites. We can then finally differentiate this 1D quadratic function $P(t)$ twice to obtain a value of $k_i = V''(x_i)$ at the muon sites.

Appendix D

Derivation of WKB transition rate formula

We start by expressing the wavefunction as $\psi(x) = \exp(if(x)/\hbar)$ where $f(x)$ is a complex function, so that the Schrödinger equation is:

$$\begin{gathered}\frac{d\psi}{dx^2} = -\frac{p^2}{\hbar^2}\psi \quad \text{where} \quad p = \sqrt{2m[E - V(x)]} \\ \left[\frac{i}{\hbar}f'' - \left(\frac{1}{\hbar^2}\right)f^{2\prime}\right]\exp\left(\frac{if}{\hbar}\right) = -\frac{p^2}{\hbar^2}\exp\left(\frac{if}{\hbar}\right) \\ i\hbar f'' - f^{2\prime} + p^2 = 0\,,\end{gathered} \tag{D.1}$$

so that expanding $f(x)$ as a power series $f = f_0 + \hbar f_1 + \hbar^2 f_2 + \ldots$ in $\hbar$ we have:

$$\begin{aligned}(f_0)^{2\prime} &= p^2 \\ i(f_0)'' &= 2(f_0)'(f_1)' \\ i(f_1)'' &= 2(f_0)'(f_2)' + (f_1')^2\,.\end{aligned} \tag{D.2}$$

This means that to first order in $\hbar$ we have:

$$\begin{aligned}(f_0)' = \pm p \rightarrow f_0 &= \pm\int p(x)\,dx + C_0 \\ (f_1)' = \frac{i}{2}\left[\frac{(f_0)''}{(f_0)'}\right] \rightarrow f_1 &= \frac{i}{2}\ln(p) + C_1 \\ \psi &= \frac{C}{\sqrt{p}}\exp\left[\left(\pm\frac{i}{\hbar}\right)\left(\int p\,dx\right)\right].\end{aligned} \tag{D.3}$$

Additionally, in the tunnelling case where we have $E < V(x)$, the WKB approximation can be written as:

$$\psi = \frac{C}{\sqrt{|p|}}\exp\left[\frac{1}{\hbar}\left(\int |p|\,dx\right)\right]. \tag{D.4}$$

In the usual derivation of the quantum tunnelling probability, the simplifying assumption that the walls of the potential barrier are vertical is made. To obtain a more accurate expression for the tunnelling rate by having smooth walls we must look at the behaviour of the WKB approximation close to a classical turning point $V = E$, where we have a

transition between a classical and non-classical region [115]. For a barrier with a single maximum, we have two turning points, labelled $\tilde{x}_1$ and $\tilde{x}_2$. We start considering the upward-sloping point $\tilde{x}_1$, which we can shift to $x = 0$ without loss of generality to give an approximate wavefunction

$$\psi(x) \approx \begin{cases} \frac{1}{\sqrt{p(x)}}\left[A\exp\left(\frac{i}{\hbar}\left[\int_x^0 p(x')\,dx'\right]\right) + B\exp\left(\frac{-i}{\hbar}\left[\int_x^0 p(x')\,dx'\right]\right)\right] \text{ if } x < 0 \\ \frac{1}{\sqrt{p(x)}}\left[C\exp\left(\frac{i}{\hbar}\left[\int_0^x |p(x')|\,dx'\right]\right) + D\exp\left(\frac{-i}{\hbar}\left[\int_0^x |p(x')|\,dx'\right]\right)\right] \text{ if } x > 0 \end{cases} \tag{D.5}$$

Notice that at the turning point $p(x) \to 0$ and so our approximation for ψ goes to infinity as the WKB method fails, since the wavefunction is no longer varying slowly in space. To resolve this issue we patch the two regions by approximating the potential near the turning point by a Taylor expansion to first order

$$V(x) \approx E + V'(0)\,x\,, \tag{D.6}$$

so that the Schrödinger equation becomes

$$\frac{d\psi_p}{dx} = \alpha^3 x \psi_p \quad \text{where} \quad \alpha = \left[\left(\frac{2m}{\hbar^2}\right)V'(0)\right]^{1/3}, \tag{D.7}$$

which is Airy's equation with solutions given by a linear combination of the Airy functions $\psi_p = a\mathrm{Ai}(\alpha x) + b\mathrm{Bi}(\alpha x)$. Over the patching region we have $p(x) \approx \hbar\alpha^{3/2}\sqrt{-x}$, whose integral matches the asymptotic behaviour of the Airy function for $\alpha x \gg 0$, so that we obtain

$$a = 2D\sqrt{\frac{\pi}{\alpha\hbar}} \quad \text{and} \quad b = C\sqrt{\frac{\pi}{\alpha\hbar}}\,. \tag{D.8}$$

Similarly for the other part of the wavefunction, where $\alpha x \ll 0$ we have

$$A = \sqrt{\frac{\pi}{\alpha\hbar}}\left(\frac{-ia+b}{2}\right)\exp\left(\frac{i\pi}{4}\right) \quad \text{and} \quad B = \sqrt{\frac{\pi}{\alpha\hbar}}\left(\frac{ia+b}{2}\right)\exp\left(\frac{-i\pi}{4}\right), \tag{D.9}$$

giving the so-called *connection formulas* for $\tilde{x}_1$

$$A = \left(\frac{C}{2} - iD\right)\exp\left(\frac{i\pi}{4}\right) \quad \text{and} \quad B = \left(\frac{C}{2} + iD\right)\exp\left(\frac{-i\pi}{4}\right). \tag{D.10}$$

An analogous calculation can be performed for the downward-sloping turning point at $\tilde{x}_2$, with the wavefunction now being

$$\psi(x) \approx \begin{cases} \frac{1}{\sqrt{p(x)}}\left[C' \exp\left(\frac{i}{\hbar}\left[\int_x^0 |p(x')|\,dx'\right]\right) + D' \exp\left(\frac{-i}{\hbar}\left[\int_x^0 |p(x')|\,dx'\right]\right)\right] \text{ if } x < 0 \\ \frac{1}{\sqrt{p(x)}} F \exp\left(\frac{i}{\hbar}\left[\int_0^x p(x')\,dx'\right]\right) \text{ if } x > 0 \end{cases} \tag{D.11}$$

where we define $C' = De^{-\gamma}$ and $D' = Ce^{-\gamma}$ with $\gamma = \int_{\tilde{x}_1}^{\tilde{x}_2} |p(x)|\,dx$. The connecting formulas for $\tilde{x}_2$ then are

$$C' = \exp\left(\frac{-i\pi}{4}\right) F \quad \text{and} \quad D' = \frac{i}{2} \exp\left(\frac{-i\pi}{4}\right) F\,, \tag{D.12}$$

meaning that the transition rate is given by

$$T = \left|\frac{F}{A}\right|^2 = \frac{\exp(-2\gamma)}{\left[1 - \frac{1}{4}\exp(-2\gamma)\right]^2}\,, \tag{D.13}$$

which when $\gamma \gg 1$ tends towards the more typical expression $T = e^{-2\gamma}$.

Bibliography

[1] A.J. Steele, T. Lancaster, S.J. Blundell, P.J. Baker, F.L. Pratt, C. Baines, M.M. Conner, H.I. Southerland, J.L. Manson, and J.A. Schlueter, Magnetic Order in Quasi-Two-Dimensional Molecular Magnets Investigated With Muon-Spin Relaxation, *Physical Review B* **84**(6), 064412 (2011).

[2] D. Opherden, N. Nizar, K. Richardson, J.C. Monroe, M.M. Turnbull, M. Polson, S. Vela, W.J.A. Blackmore, P.A. Goddard, J. Singleton *et al.*, Extremely Well Isolated Two-Dimensional Spin- 12 Antiferromagnetic Heisenberg Layers With a Small Exchange Coupling in the Molecular-Based Magnet Cupof, *Physical Review B* **102**(6), 064431 (2020).

[3] B.M. Huddart, M.T. Birch, F.L. Pratt, S.J. Blundell, D.G. Porter, S.J. Clark, W. Wu, S.R. Julian, P.D. Hatton, and T. Lancaster, Local Magnetism, Magnetic Order and Spin Freezing in the 'nonmetallic Metal' Fecras, *Journal of Physics: Condensed Matter* **31**(28), 285803 (2019).

[4] K.J.A. Franke, B.M. Huddart, T.J. Hicken, F. Xiao, S.J. Blundell, F.L. Pratt, M. Crisanti, J.A.T. Barker, S.J. Clark, A. Štefančič *et al.*, Magnetic Phases of Skyrmion-Hosting GaV4S8-ySey(y=0,2,4,8) Probed With Muon Spectroscopy, *Physical Review B* **98**(5), 054428 (2018).

[5] F.K.K. Kirschner, N.E. Sluchanko, V.B. Filipov, F.L. Pratt, C. Baines, N.Yu. Shitsevalova, and S.J. Blundell, Observation of a Crossover From Nodal To Gapped Superconductivity in Luxzr1-xb12, *Physical Review B* **98**(9), 094505 (2018).

[6] S.J. Blundell and T. Lancaster, DFT+μ: Density functional theory for muon site determination, *Applied Physics Reviews* **10**(2), (2023).

[7] P. Bonfà and R. De Renzi, Toward the Computational Prediction of Muon Sites and Interaction Parameters, *Journal of the Physical Society of Japan* **85**(9), 091014 (2016).

[8] S.J. Clark, M.D. Segall, C.J. Pickard, P.J. Hasnip, M.I.J. Probert, K. Refson, and M.C. Payne, First principles methods using CASTEP, *Zeitschrift für Kristallographie - Crystalline Materials* **220**(5–6), 567–570 (2005).

[9] X.Z. Li, M.I.J. Probert, A. Alavi, and A. Michaelides, Quantum Nature of the Proton in Water-Hydroxyl Overlayers on Metal Surfaces, *Physical Review Letters* **104**(6), 066102 (2010).

[10] D. Marx and M. Parrinello, Ab Initio Path-Integral Molecular Dynamics, *Zeitschrift fr Physik B Condensed Matter* **95**(2), 143-144 (1994).

[11] S.F.J. Cox, Implanted Muon Studies in Condensed Matter Science, *Journal of Physics C: Solid State Physics* **20**(22), 3187-3319 (1987).

[12] S.J. Blundell, R. De Renzi, T. Lancaster, and F.L. Pratt, *Muon Spectroscopy: An Introduction*, p.. 432 (Oxford University Press, 2022).

[13] F. Scheck, Muon physics, *Physics Reports* **44**(4), 187–248 (1978).

[14] S.J. Blundell, Spin-polarized muons in condensed matter physics, *Contemporary Physics* **40**(3), 175–192 (1999).

[15] P.D. de Réotier and A. Yaouanc, Muon spin rotation and relaxation in magnetic materials, *Journal of Physics: Condensed Matter* **9**(43), 9113–9166 (1997).

[16] C.E. Soliverez, The Contact Hyperfine Interaction: an Ill-Defined Problem, *Journal of Physics C: Solid State Physics* **13**(34), L1017-L1019 (1980).

[17] A. Schenck, D. Andreica, F.N. Gygax, and H.R. Ott, Extreme Quantum Behavior of Positive Muons Inceal2below 1 K, *Physical Review B* **65**(2), 024444 (2001).

[18] C. Kittel, *Introduction to solid state physics* (Wiley, Hoboken, NJ, 2018).

[19] S. Sturniolo, L. Liborio, E. Chadwick, J. Thomas, and A. Mudaraddi, MuSpinSim: spin dynamics calculations for muon science, *Journal of Physics: Conference Series* **2462**(1), 012017 (2023).

[20] B.M. Huddart, *Muon stopping sites in magnetic systems from density functional theory*, (PhD thesis) (2020).

[21] R. Kubo and T. Toyabe, *Magnetic resonance and relaxation* (North-Holland, Amsterdam, 1967).

[22] J. Sugiyama, Y. Ikedo, K. Mukai, J.H. Brewer, E.J. Ansaldo, G.D. Morris, K.H. Chow, H. Yoshida, and Z. Hiroi, Incommensurate magnetic order in Ag_2NiO_2 studied with muon-spin-rotation and relaxation spectroscopy, *Physical Review B* **73**(22), (2006).

[23] A.T. Savici, Y. Fudamoto, I.M. Gat, T. Ito, M.I. Larkin, Y.J. Uemura, G.M. Luke, K.M. Kojima, Y.S. Lee, M.A. Kastner *et al.*, Muon spin relaxation studies of incommensurate magnetism and superconductivity in stage-4 $La_2CuO_{4.11}$ and $La_{1.88}Sr_{0.12}CuO_4$, *Physical Review B* **66**(1), (2002).

[24] R.S. Hayano, Y.J. Uemura, J. Imazato, N. Nishida, T. Yamazaki, and R. Kubo, Zero-And Low-Field Spin Relaxation Studied By Positive Muons, *Physical Review B* **20**(3), 850-859 (1979).

[25] J.H. Brewer, S.R. Kreitzman, D.R. Noakes, E.J. Ansaldo, D.R. Harshman, and R. Keitel, Observation of muon-fluorine "hydrogen bonding" in ionic crystals, *Physical Review B* **33**(11), 7813–7816 (1986).

[26] J. Wilkinson, *Muon sites and muon states in model fluorides and magnets*, (PhD thesis) (2022).

[27] D.R. Noakes, E.J. Ansaldo, S.R. Kreitzman, and G.M. Luke, The $(F\mu F)-$ ion in solid fluorides, *Journal of Physics and Chemistry of Solids* **54**(7), 785–792 (1993).

[28] K. Nishiyama, S.W. Nishiyama, and W. Higemoto, Asymmetric F–μ–F interaction of the muon in polyfluorocarbons, *Physica B: Condensed Matter* **326**(1–4), 41–45 (2003).

[29] T. Lancaster, S.J. Blundell, P.J. Baker, M.L. Brooks, W. Hayes, F.L. Pratt, J.L. Manson, M.M. Conner, and J.A. Schlueter, Muon-Fluorine Entangled States in Molecular Magnets, *Physical Review Letters* **99**(26), (2007).

[30] I. McKenzie, *Investigations of the Structure and Dynamics of Novel Muoniated Radicals*, (PhD thesis) (2014).

[31] N.P. Bentley and S.J. Blundell, The interaction between a positive muon and multiple quadrupolar nuclei, *Journal of Physics: Conference Series* **2462**(1), 012043 (2023).

[32] S. Sturniolo and L. Liborio, Computational Prediction of Muon Stopping Sites: a Novel Take on the Unperturbed Electrostatic Potential Method, *The Journal of Chemical Physics* **153**(4), 044111 (2020).

[33] M. Born and R. Oppenheimer, Zur Quantentheorie Der Molekeln, *Annalen der Physik* **389**(20), 457-484 (1927).

[34] P. Hohenberg and W. Kohn, Inhomogeneous Electron Gas, *Physical Review* **136**(3B), B864-B871 (1964).

[35] W. Kohn and L.J. Sham, Self-Consistent Equations Including Exchange and Correlation Effects, *Physical Review* **140**(4A), A1133-A1138 (1965).

[36] Á. Morales-García, R. Valero, and F. Illas, An Empirical, yet Practical Way To Predict the Band Gap in Solids by Using Density Functional Band Structure Calculations, *The Journal of Physical Chemistry C* **121**(34), 18862–18866 (2017).

[37] S.F. Sousa, P.A. Fernandes, and M.J. Ramos, General Performance of Density Functionals, *The Journal of Physical Chemistry A* **111**(42), 10439-10452 (2007).

[38] J.P. Perdew and A. Zunger, Self-interaction correction to density-functional approximations for many-electron systems, *Physical Review B* **23**(10), 5048–5079 (1981).

[39] A.D. Becke, Density-functional thermochemistry. I. The effect of the exchange-only gradient correction, *The Journal of Chemical Physics* **96**(3), 2155–2160 (1992).

[40] J.P. Perdew, K. Burke, and M. Ernzerhof, Generalized Gradient Approximation Made Simple, *Physical Review Letters* **77**(18), 3865–3868 (1996).

[41] J. Toulouse, *Review of Approximations for the Exchange-Correlation Energy in Density-Functional Theory*, In *Density Functional Theory*, pp.. 1–90 (Springer International Publishing, 2022).

[42] I. Štich, R. Car, M. Parrinello, and S. Baroni, Conjugate Gradient Minimization of the Energy Functional: a New Method for Electronic Structure Calculation, *Physical Review B* **39**(8), 4997-5004 (1989).

[43] H.J. Monkhorst and J.D. Pack, Special points for Brillouin-zone integrations, *Physical Review B* **13**(12), 5188–5192 (1976).

[44] N.D. Woods, M.C. Payne, and P.J. Hasnip, Computing the self-consistent field in Kohn–Sham density functional theory, *Journal of Physics: Condensed Matter* **31**(45), 453001 (2019).

[45] J.M. Millam and G.E. Scuseria, Linear scaling conjugate gradient density matrix search as an alternative to diagonalization for first principles electronic structure calculations, *The Journal of Chemical Physics* **106**(13), 5569–5577 (1997).

[46] N. Marzari, D. Vanderbilt, and M.C. Payne, Ensemble Density-Functional Theory Forab Initiomolecular Dynamics of Metals and Finite-Temperature Insulators, *Physical Review Letters* **79**(7), 1337-1340 (1997).

[47] D. Vanderbilt, Soft self-consistent pseudopotentials in a generalized eigenvalue formalism, *Physical Review B* **41**(11), 7892–7895 (1990).

[48] R.P. Feynman, Forces in Molecules, *Physical Review* **56**(4), 340–343 (1939).

[49] S. Baroni, S. de Gironcoli, A. Dal Corso, and P. Giannozzi, Phonons and related crystal properties from density-functional perturbation theory, *Reviews of Modern Physics* **73**(2), 515–562 (2001).

[50] M. Born and K. Huang, *Dynamical Theory Of Crystal Lattices* (Oxford University PressNew York, NY, 1996).

[51] K. Refson, P.R. Tulip, and S.J. Clark, Variational density-functional perturbation theory for dielectrics and lattice dynamics, *Physical Review B* **73**(15), (2006).

[52] N. Govind, M. Petersen, G. Fitzgerald, D. King-Smith, and J. Andzelm, A generalized synchronous transit method for transition state location, *Computational Materials Science* **28**(2), 250–258 (2003).

[53] G. Henkelman, B.P. Uberuaga, and H. Jónsson, A climbing image nudged elastic band method for finding saddle points and minimum energy paths, *The Journal of Chemical Physics* **113**(22), 9901–9904 (2000).

[54] B.M. Huddart, A. Hernández-Melián, T.J. Hicken, M. Gomilšek, Z. Hawkhead, S.J. Clark, F.L. Pratt, and T. Lancaster, MuFinder: A program to determine and analyse muon stopping sites, *Computer Physics Communications* **280** 108488 (2022).

[55] L. Liborio, S. Sturniolo, and D. Jochym, Computational prediction of muon stopping sites using ab initio random structure searching (AIRSS), *The Journal of Chemical Physics* **148**(13), (2018).

[56] D.J. Pearce, An Improved Algorithm for Finding the Strongly Connected Components of a Directed Graph (2005).

[57] P. Bonfà, I.J. Onuorah, A. Lim, and R. De Renzi, *MuESR: Version 0.1.2*, https://github.com/bonfus/muesr (unpublished).

[58] I.J. Onuorah, P. Bonfà, R. De Renzi, L. Monacelli, F. Mauri, M. Calandra, and I. Errea, Quantum effects in muon spin spectroscopy within the stochastic self-consistent harmonic approximation, *Physical Review Materials* **3**(7), (2019).

[59] M. Gomilšek, F.L. Pratt, S.P. Cottrell, S.J. Clark, and T. Lancaster, Many-body quantum muon effects and quadrupolar coupling in solids, *Communications Physics* **6**(1), (2023).

[60] L. Kantorovich, *Quantum Theory of the Solid State: An Introduction* (Springer Netherlands, 2004).

[61] Z.Y. Meng, T.C. Lang, S. Wessel, F.F. Assaad, and A. Muramatsu, Quantum spin liquid emerging in two-dimensional correlated Dirac fermions, *Nature* **464**(7290), 847–851 (2010).

[62] A.F. Albuquerque, D. Schwandt, B. Hetényi, S. Capponi, M. Mambrini, and A.M. Läuchli, Phase diagram of a frustrated quantum antiferromagnet on the honeycomb lattice: Magnetic order versus valence-bond crystal formation, *Physical Review B* **84**(2), (2011).

[63] H. Yamaguchi, M. Okada, Y. Kono, S. Kittaka, T. Sakakibara, T. Okabe, Y. Iwasaki, and Y. Hosokoshi, Randomness-induced quantum spin liquid on honeycomb lattice, *Scientific Reports* **7**(1), (2017).

[64] O.O. Kryvchikov and D.V. Laptiev, The exotic ground state of the decorated honeycomb lattice, *Low Temperature Physics* **49**(12), 1439–1443 (2023).

[65] A. Kitaev, Anyons in an exactly solved model and beyond, *Annals of Physics* **321**(1), 2–111 (2006).

[66] H. Takagi, T. Takayama, G. Jackeli, G. Khaliullin, and S.E. Nagler, Concept and realization of Kitaev quantum spin liquids, *Nature Reviews Physics* **1**(4), 264–280 (2019).

[67] S.A. Antonenko and A.I. Sokolov, Critical Exponents for a Three-Dimensional O(n)-symmetric Model Withn>3, *Physical Review E* **51**(3), 1894-1898 (1995).

[68] L. Anghinolfi, H. Luetkens, J. Perron, M.G. Flokstra, O. Sendetskyi, A. Suter, T. Prokscha, P.M. Derlet, S.L. Lee, and L.J. Heyderman, Thermodynamic phase transitions in a frustrated magnetic metamaterial, *Nature Communications* **6**(1), (2015).

[69] S.K. Choi, R. Coldea, A.N. Kolmogorov, T. Lancaster, I.I. Mazin, S.J. Blundell, P.G. Radaelli, Y. Singh, P. Gegenwart, K.R. Choi *et al.*, Spin Waves and Revised Crystal Structure of Honeycomb Iridate Na_2IrO_3, *Physical Review Letters* **108**(12), (2012).

[70] S. Haddad, S. Charfi-Kaddour, and J.P. Pouget, Inhomogeneous superconductivity in organic conductors: the role of disorder and magnetic field, *Journal of Physics: Condensed Matter* **23**(46), 464205 (2011).

[71] H. Alloul, J. Bobroff, M. Gabay, and P.J. Hirschfeld, Defects in correlated metals and superconductors, *Reviews of Modern Physics* **81**(1), 45–108 (2009).

[72] O. Sato, Dynamic molecular crystals with switchable physical properties, *Nature Chemistry* **8**(7), 644–656 (2016).

[73] M.B. Mills, T. Wohlhauser, B. Stein, W.R. Verduyn, E. Song, P. Dechambenoit, M. Rouzières, R. Clérac, and K.E. Preuss, Magnetic Bistability in Crystalline Organic Radicals: The Interplay of H-bonding, Pancake Bonding, and Electrostatics in 4-(2′-Benzimidazolyl)-1,2,3,5-dithiadiazolyl, *Journal of the American Chemical Society* **140**(49), 16904–16908 (2018).

[74] S.J. Blundell, F.L. Pratt, I.M. Marshall, C.A. Steer, W. Hayes, J.F. Létard, S.L. Heath, A. Caneschi, and D. Gatteschi, Muon study of molecular magnets, spin crossover and magnetic nanodiscs, *Synthetic Metals* **133–134** 531–533 (2003).

[75] T. Lancaster, S.J. Blundell, F.L. Pratt, M.L. Brooks, J.L. Manson, E.K. Brechin, C. Cadiou, D. Low, E.J.L. McInnes, and R.E.P. Winpenny, Muons as a probe of magnetism in molecule-based low dimensional magnets, *Journal of Physics: Condensed Matter* **16**(40), S4563–S4582 (2004).

[76] A.W. Cordes, R.C. Haddon, R.T. Oakley, L.F. Schneemeyer, J.V. Waszczak, K.M. Young, and N.M. Zimmerman, Molecular semiconductors from bifunctional dithia- and diselenadiazolyl radicals. Preparation and solid-state structural and electronic properties of 1,4-[(E2N2C)C6H4(CN2E2)] (E = sulfur, selenium), *Journal of the American Chemical Society* **113**(2), 582–588 (1991).

[77] Y.J. Uemura, T. Yamazaki, D.R. Harshman, M. Senba, and E.J. Ansaldo, Muon-spin relaxation in AuFe and CuMn spin glasses, *Phys. Rev. B* **31** 546–563 (1985).

[78] S.J. Blundell, F.L. Pratt, C.A. Steer, I.M. Marshall, and J.F. Létard, A μSR study of the spin-crossover, *J. Phys. Chem. Sol.* **65**(1), 25-28 (2004).

[79] T. Lancaster, F. Xiao, B.M. Huddart, R.C. Williams, F.L. Pratt, S.J. Blundell, S.J. Clark, R. Scheuermann, T. Goko, S. Ward *et al.*, Quantum magnetism in molecular spin ladders probed with muon-spin spectroscopy, *New Journal of Physics* **20**(10), 103002 (2018).

[80] E. Trzop, D. Zhang, L. Piñeiro-Lopez, F.J. Valverde-Muñoz, M. Carmen Muñoz, L. Palatinus, L. Guerin, H. Cailleau, J.A. Real, and E. Collet, First Step Towards a Devil's Staircase in Spin-Crossover Materials, *Angewandte Chemie International Edition* **55**(30), 8675–8679 (2016).

[81] B.J. Kim, H. Jin, S.J. Moon, J.Y. Kim, B.G. Park, C.S. Leem, J. Yu, T.W. Noh, C. Kim, S.J. Oh *et al.*, Novel $J_{\rm eff} = 1/2$ Mott State Induced by Relativistic Spin-Orbit Coupling in Sr_2IrO_4, *Physical Review Letters* **101**(7), (2008).

[82] S.B. Roy, *Mott Insulators: Physics and applications* (IOP Publishing, 2019).

[83] J.G. Rau, E.K.H. Lee, and H.Y. Kee, Spin-Orbit Physics Giving Rise to Novel Phases in Correlated Systems: Iridates and Related Materials, *Annual Review of Condensed Matter Physics* **7**(1), 195–221 (2016).

[84] F. Ye, C. Hoffmann, W. Tian, H. Zhao, and G. Cao, Pseudospin-lattice coupling and electric control of the square-lattice iridate $SrIr_2O_4$, *Physical Review B* **102**(11), (2020).

[85] Q. Huang, J.L. Soubeyroux, O. Chmaissem, I.N. Sora, A. Santoro, R.J. Cava, J.J. Krajewski, and W.F. Peck, Neutron Powder Diffraction Study of the Crystal Structures of Sr_2RuO_4 and Sr_2IrO_4 at Room Temperature and at 10 K, *Journal of Solid State Chemistry* **112**(2), 355–361 (1994).

[86] F. Ye, S. Chi, B.C. Chakoumakos, J.A. Fernandez-Baca, T. Qi, and G. Cao, Magnetic and crystal structures of Sr_2IrO_4: A neutron diffraction study, *Physical Review B* **87**(14), (2013).

[87] M. Ge, T.F. Qi, O.B. Korneta, D.E. De Long, P. Schlottmann, W.P. Crummett, and G. Cao, Lattice-driven magnetoresistivity and metal-insulator transition in single-layered iridates, *Physical Review B* **84**(10), (2011).

[88] I. Franke, P.J. Baker, S.J. Blundell, T. Lancaster, W. Hayes, F.L. Pratt, and G. Cao, Measurement of the internal magnetic field in the correlated iridates Ca_4IrO_6, $Ca_5Ir_3O_{12}$, $Sr_3Ir_2O_7$, and Sr_2IrO_4, *Physical Review B* **83**(9), (2011).

[89] M. Miyazaki, R. Kadono, M. Hiraishi, A. Koda, K.M. Kojima, K. Ohashi, T. Takayama, and H. Takagi, Evidence for Ordered Magnetic Moments At Oxygen Sites in Antiferromagnetic Sr_2IrO_4 and $Sr_3Ir_2O_7$, *Physical Review B* **91**(15), 155113 (2015).

[90] G. Wolberg, Cubic Spline Interpolation: A Review, (1988).

[91] H. Bethe, Zur Theorie Der Metalle, *Zeitschrift fur Physik* **71**(3-4), 205-226 (1931).

[92] T. Giamarchi, Spin 1/2 chains, In Quantum Physics in One Dimension (Oxford University Press, 2003).

[93] J.C. Bonner, H.W.J. Blöte, H. Beck, and G. Müller, *Quantum Spin Chains*, In *Physics in One Dimension*, pp.. 115–128 (Springer Berlin Heidelberg, 1981).

[94] P.R. Hammar, M.B. Stone, D.H. Reich, C. Broholm, P.J. Gibson, M.M. Turnbull, C.P. Landee, and M. Oshikawa, Characterization of a quasi-one-dimensional spin-1/2 magnet which is gapless and paramagnetic for $g\mu_B H \lesssim J$ and $k_B T \ll J$, *Physical Review B* **59**(2), 1008–1015 (1999).

[95] R. Feyerherm, S. Abens, D. Günther, T. Ishida, M. Meißner, M. Meschke, T. Nogami, and M. Steiner, Magnetic-field induced gap and staggered susceptibility in theS= 1/2 chain [PM·Cu(NO3)2·(H2O)2]n(PM = pyrimidine), *Journal of Physics: Condensed Matter* **12**(39), 8495–8509 (2000).

[96] S.A. Zvyagin, A.K. Kolezhuk, J. Krzystek, and R. Feyerherm, Excitation Hierarchy of the Quantum Sine-Gordon Spin Chain in a Strong Magnetic Field, *Physical Review Letters* **93**(2), 027201 (2004).

[97] J. Liu, S. Kittaka, R. D. Johnson, T. Lancaster, J. Singleton, T. Sakakibara, Y. Kohama, J. van Tol, A. Ardavan, B. H. Williams *et al.*, Unconventional Field-Induced Spin Gap in an S=1/2 Chiral Staggered Chain, *Physical Review Letters* **122**(5), (2019).

[98] J. Singleton, Personal communication (unpublished).

[99] R. Scatena, Personal communication (2020).

[100] P. Goddard, Personal communication (unpublished).

[101] E. Ressouche, Reminder: Magnetic Structures Description and Determination By Neutron Diffraction, *École thématique de la Société Française de la Neutronique* **13**(nil), 02001 (2014).

[102] P.D. de Réotier, A. Maisuradze, A. Yaouanc, B. Roessli, A. Amato, D. Andreica, and G. Lapertot, Determination of the Zero-Field Magnetic Structure of the Helimagnet MnSi At Low Temperature, *Physical Review B* **93**(14), 144419 (2016).

[103] N. Martin, M. Deutsch, F. Bert, D. Andreica, A. Amato, P. Bonfà, R.D. Renzi, U.K. Rößler, P. Bonville, L.N. Fomicheva *et al.*, Magnetic Ground State and Spin Fluctuations in Mnge Chiral Magnet As Studied By Muon Spin Rotation, *Physical Review B* **93**(17), 174405 (2016).

[104] D.A. Andreica, *Magnetic phase diagram in some Kondo-lattice compounds. microscopic and macroscopic studies*, (PhD thesis). ETH Zurich, Zürich (2001). (Diss., Naturwissenschaften ETH Zürich, Nr. 14170, 2001.)

[105] J.H. Van Vleck, The Dipolar Broadening of Magnetic Resonance Lines in Crystals, *Physical Review* **74**(9), 1168–1183 (1948).

[106] V.I. Lebedev and D.N. Laikov, A quadrature formula for the sphere of the 131st algebraic order of accuracy, *Doklady Mathematics* **59**(3), 477 – 481 (1999).

[107] R. Kadono, J. Imazato, T. Matsuzaki, K. Nishiyama, K. Nagamine, T. Yamazaki, D. Richter, and J.M. Welter, Quantum diffusion of positive muons in copper, *Physical Review B* **39**(1), 23–41 (1989).

[108] V.G. Storchak and N.V. Prokof'ev, Quantum diffusion of muons and muonium atoms in solids, *Reviews of Modern Physics* **70**(3), 929–978 (1998).

[109] A.D. Pant, E. Torikai, H. Nakanishi, and H. Kasai, First Principles Study of Positive Muon and Hydrogen Nucleus (H+, D+) on Graphene, In Proceedings of the International Symposium on Science Explored by Ultra Slow Muon (USM2013) (Journal of the Physical Society of Japan, 2014).

[110] M. Plazanet, M.R. Johnson, J.D. Gale, T. Yildirim, G.J. Kearley, M.T. Fernández-Díaz, D. Sánchez-Portal, E. Artacho, J.M. Soler, P. Ordejón *et al.*, The structure and dynamics of crystalline durene by neutron scattering and numerical modelling using density functional methods, *Chemical Physics* **261**(1–2), 189–203 (2000).

[111] R.M. Ibberson, W.I.F. David, S. Parsons, M. Prager, and K. Shankland, The crystal structures of m-xylene and p-xylene, C_8D_{10}, at 4.5 K, *Journal of Molecular Structure* **524**(1–3), 121–128 (2000).

[112] R.M. Ibberson, C. Morrison, and M. Prager, Neutron powder and ab initio structure of ortho-xylene: the influence of crystal packing on phenyl ring geometry at 2 K, *Chemical Communications* 7, 539–540 (2000).

[113] C.J. Craven, P.D. Hatton, C.J. Howard, and G.S. Pawley, The structure and dynamics of solid benzene. A neutron powder diffraction study of deuterated benzene from 4 K to the melting point, *The Journal of Chemical Physics* **98**(10), 8236–8243 (1993).

[114] D.F. Crouse, On implementing 2D rectangular assignment algorithms, *IEEE Transactions on Aerospace and Electronic Systems* **52**(4), 1679–1696 (2016).

[115] D.J. Griffiths and D.F. Schroeter, *Introduction to Quantum Mechanics* (Cambridge University Press, 2018).

[116] A. Beiser, *Concepts of Modern Physics* (McGraw-Hill, 2003).

[117] C.G. Van de Walle and P.E. Blöchl, First-principles calculations of hyperfine parameters, *Physical Review B* **47**(8), 4244–4255 (1993).

[118] S. Sturniolo, L. Liborio, F.L. Pratt, S.P. Cottrell, D.B. Jochym, and B. Montanari, Exploring the Temperature Dependent Solid-State ALC Spectrum of the C6H6Mu•Radical with Ab-Initio Simulation Techniques, In Proceedings of the 14th International Conference on Muon Spin Rotation, Relaxation and Resonance (μSR2017) (Journal of the Physical Society of Japan, 2018).

[119] J.S. Möller, D. Ceresoli, T. Lancaster, N. Marzari, and S.J. Blundell, Quantum states of muons in fluorides, *Physical Review B* **87**(12), (2013).

[120] J. Lord, *Quantumtools: Version 1.04*, https://github.com/mantidproject/scriptrepository (unpublished).

[121] P.H. Cribb, S. Nordholm, and N.S. Hush, A density matrix approach to double well transfer: effects of asymmetry on the tunneling rate, *Chemical Physics* **44**(3), 315–335 (1979).

[122] A.D. Godbeer, J.S. Al-Khalili, and P.D. Stevenson, Modelling proton tunnelling in the adenine–thymine base pair, *Physical Chemistry Chemical Physics* **17**(19), 13034–13044 (2015).

[123] R.F. Kiefl, M. Celio, T.L. Estle, S.R. Kreitzman, G.M. Luke, T.M. Riseman, and E.J. Ansaldo, ^{29}Si Hyperfine Structure of Anomalous Muonium in Silicon: Proof of the Bond-Centered Model, *Physical Review Letters* **60**(3), 224–226 (1988).

[124] Jon. Drobny and D. Curreli, RustBCA: A High-Performance Binary-Collision-Approximation Code for Ion-Material Interactions, *Journal of Open Source Software* **6**(64), 3298 (2021).

[125] T.K. Stenczel, Z. El-Machachi, G. Liepuoniute, J.D. Morrow, A.P. Bartók, M.I.J. Probert, G. Csányi, and V.L. Deringer, Machine-learned acceleration for molecular dynamics in CASTEP, *The Journal of Chemical Physics* **159**(4), (2023).

[126] J.A. Dickinson, Q. Yu, and S. Hammes-Schiffer, Generalized Nuclear-Electronic Orbital Multistate Density Functional Theory for Multiple Proton Transfer Processes, *The Journal of Physical Chemistry Letters* **14**(26), 6170–6178 (2023).

[127] N.W. Ashcroft and N.D. Mermin, *Solid State Physics* (Holt, Rinehart and Winston, 1976).

[128] S. Jiang and L. Greengard, Approximating the Gaussian As a Sum of Exponentials and Its Applications To the Fast Gauss Transform, *Communications in Computational Physics* **31**(1), 1-26 (2022).

[129] Z. Gao, J. Liang, and Z. Xu, A Kernel-Independent Sum-of-Exponentials Method, *Journal of Scientific Computing* **93**(2), (2022).